

Submillimeter and Mid-Infrared Variability of Young Stellar Objects in the M17 SWex Intermediate-Mass Star-Forming Region

GEUMSOOK PARK,^{1, 2, 3} DOUG JOHNSTONE,^{4, 5} CARLOS CONTRERAS PEÑA,^{6, 7} JEONG-EUN LEE,^{6, 8} SHENG-YUAN LIU,⁹ GREGORY HERCZEG,^{10, 11} STEVE MAIRS,^{4, 12} ZHIWEI CHEN,¹³ JENNIFER HATCHELL,¹⁴ KEE-TAE KIM,^{3, 15} MI-RYANG KIM,⁶ KEPING QIU,¹⁶ YAO-TE WANG,^{9, 17} XU ZHANG,¹⁶ AND THE JCMT TRANSIENT TEAM

¹ Telepix Co., Ltd., 17, Techno 4-ro, Yuseong-gu, Daejeon 34013, Republic of Korea

² Research Institute of Natural Sciences, Chungnam National University, 99 Daehak-ro, Yuseong-gu, Daejeon 34134, Republic of Korea

³ Korea Astronomy and Space Science Institute, 776 Daedeokdae-ro, Yuseong-gu, Daejeon 34055, Republic of Korea

⁴ NRC Herzberg Astronomy and Astrophysics, 5071 West Saanich Rd, Victoria, BC, V9E 2E7, Canada

⁵ Department of Physics and Astronomy, University of Victoria, Victoria, BC, V8P 5C2, Canada

⁶ Department of Physics and Astronomy, Seoul National University, 1 Gwanak-ro, Gwanak-gu, Seoul 08826, Korea

⁷ Research Institute of Basic Sciences, Seoul National University, Seoul 08826, Republic of Korea

⁸ SNU Astronomy Research Center, Seoul National University, 1 Gwanak-ro, Gwanak-gu, Seoul 08826, Korea

⁹ Academia Sinica Institute of Astronomy and Astrophysics, 11F of AS/NTU Astronomy-Mathematics Building, No.1, Sec. 4, Roosevelt Rd, Taipei 10617, Taiwan, R.O.C.

¹⁰ Kavli Institute for Astronomy and Astrophysics, Peking University, Yiheyuan Lu 5, Haidian Qu, 100871 Beijing, Peoples Republic of China

¹¹ Department of Astronomy, Peking University, Yiheyuan 5, Haidian Qu, 100871 Beijing, China

¹² East Asian Observatory, 660 N. A‘ohōkū Place, Hilo, Hawai‘i, 96720, USA

¹³ Purple Mountain Observatory, Chinese Academy of Sciences, 10 Yuanhua, 210023 Nanjing, China

¹⁴ Physics and Astronomy, University of Exeter, Stocker Road, Exeter EX4 4QL, UK

¹⁵ University of Science and Technology, Korea (UST), 217 Gajeong-ro, Yuseong-gu, Daejeon 34113, Republic of Korea

¹⁶ School of Astronomy and Space Science, Nanjing University Xianlin Campus, 163 Xianlin Avenue, Qixia District, Nanjing, Jiangsu, China, 210023

¹⁷ Graduate Institute of Astrophysics, National Taiwan University, No. 1, Sec. 4, Roosevelt Rd., Taipei 10617, Taiwan, R.O.C.

ABSTRACT

We present a comprehensive analysis of young stellar object (YSO) variability within the M17 Southwest Extension (M17 SWex), using 3.5 years of monitoring data from the JCMT Transient Survey at sub-millimeter (sub-mm) and 9 years from the NEOWISE mission at mid-infrared (mid-IR). Our study encompasses observations of 147 bright sub-mm peaks identified within our deep JCMT co-added map as well as 156 YSOs in NEOWISE W1 and 179 in W2 that were previously identified in Spitzer surveys. We find three robust sub-mm variables: two are candidate YSOs and one is a likely extragalactic source. At mid-IR wavelengths, our analysis reveals secular and stochastic variability in 47 YSOs, with the highest fraction of secular variability occurring at the earliest evolutionary stage. This is similar to what has previously been observed for low-mass YSO variability within the Gould Belt. However, we observe less overall variability in M17 SWex at both the sub-mm and mid-IR. We suspect that this lower fraction is due to the greater distance to M17 SWex. Our findings showcase the utility of multi-wavelength observations to better capture the complex variability phenomena inherent to star formation processes and demonstrate the importance of years-long monitoring of a diverse selection of star-forming environments.

1. INTRODUCTION

Variability in young stellar objects (YSOs) provides a powerful tool for understanding the physical processes that occur during star formation and the history of mass assembly onto the forming star (see review by Fischer et al. 2023 and studies by, e.g., Carpenter et al. 2001; Caramazza et al. 2007; Billot et al. 2012; Cody et al. 2014; Guarcello et al. 2017). While optical and near-

infrared (near-IR) surveys have revealed the complex variability of the less obscured disk-hosting and diskless YSOs, those protostars that are deeply embedded within their nascent envelopes are much more challenging to monitor. The optical depth and geometric complexities, such as the envelope structures and outflow cavities, significantly impact observed fluxes, including at mid-infrared (mid-IR) wavelengths (e.g. Whitney et al.

2003). These complications have a significant influence on our interpretation of mid-IR outbursts from YSOs, potentially making our understanding of their early evolution stages more uncertain (e.g., Fischer et al. 2019; MacFarlane et al. 2019a,b; Baek et al. 2020; Fischer et al. 2024). This complexity is significantly reduced by far-infrared (far-IR) through submillimeter (sub-mm) observations. Because these wavelengths respond to the reprocessing of the protostellar luminosity by the enshrouding envelope, they are mostly robust to geometrical uncertainties and help to clarify the underlying nature of the variability and the mechanisms behind it (Johnstone et al. 2013; Fischer et al. 2024).

Variability in the accretion rate of mass onto stars manifests as a change in the protostellar luminosity as released gravitational energy heats the infalling matter. Thus a history of the mass assembly of stars is directly observable through variations in the protostellar brightness. Accretion variability, especially that associated with intense bursts, may play an important role in the mass assembly of the protostar (Scholz et al. 2013; Fischer et al. 2019; Park et al. 2021), impact the chemical evolution of both the envelope and the disk surrounding the YSO (e.g. Lee 2007; Jørgensen et al. 2015; Molyarova et al. 2018; Hsieh et al. 2019) and potentially affect the contraction of the forming star (e.g. Baraffe & Chabrier 2010; Hosokawa et al. 2011; Kunitomo et al. 2017). As mentioned, optically thick YSO envelopes obscure this variability at optical through near-IR wavelengths during the early stages of stellar evolution. These are, however, the phases where stars acquire most of their mass, emphasizing the importance of quantifying the role of variability during this epoch.

The best wavelength range to monitor accretion variability from deeply embedded protostars is the far-IR. Unfortunately this is not possible from the ground. Sub-mm monitoring of nearby low-mass star-forming regions by the JCMT Transient Survey (Herczeg et al. 2017) since December 2015 has allowed an exploration of accretion variability properties for a modest ensemble of deeply embedded protostars during their primary growth spurts (Lee et al. 2021b; Mairs et al. 2024). Several sources with intriguing sub-mm light curves have been further analyzed using multi-wavelength data sets and sub-mm interferometry, including EC53 in Serpens Main (also known as V371 Ser, Lee et al. 2020; Baek et al. 2020; Francis et al. 2022) and HOPS 373 in Orion (Yoon et al. 2022; Lee et al. 2023, 2024).

Furthermore, despite the known uncertainties in connecting mid-IR variability directly to accretion variations, the JCMT Transient team has found excellent agreement between the long-term sub-mm and mid-IR

variability for specific sub-mm sources (Contreras Peña et al. 2020). Statistical analyses of mid-IR variability also indicate similar fractions as in the sub-mm of long-term variability, likely due to accretion (Park et al. 2021, see also analysis by Zakri et al. 2022). Thus, while for any individual YSO one must use caution when interpreting the mid-IR lightcurve, for long-term monitoring over years, we find that sources showing years-long sub-mm variations also have similar mid-IR variability on similar timescales. Still, while there is evidence for a rough calibration between the amplitude of mid-IR variations and the underlying protostellar luminosity change (see for example, Contreras Peña et al. 2020), for individual sources this can be strongly affected by the presence of mid-IR emission lines from unrelated shocks, as seen in W2 for HOPS 373 by Yoon et al. (2022). These findings have crucial implications for theories of star formation, particularly regarding the mechanisms through which stars accumulate their mass during the earliest phases of development (see review by Fischer et al. 2023).

The question remains, however, whether similar accretion-driven luminosity bursts occur in more active star-forming regions, such as those capable of forming more massive stars, and how these processes might differ in frequency, amplitude, and duration as a function of environment. In this context, the M17 Southwest Extension (M17 SWex) offers a powerful laboratory for studying star formation processes due to its proximity to the vibrant H II region M17, its status as one of the Galaxy's most prominent infrared dark cloud complexes, and its rich population of YSOs. Situated at a distance of ~ 1.8 kpc (Wu et al. 2014), M17 SWex harbors a diverse assembly of star-forming potential, including 94 Class0/I objects, 179 Class II objects, and 48 objects with ambiguous classification based on the Spitzer GLIMPSE and MIPSGL survey (Povich & Whitney 2010). This large population of YSOs across a wide-range of evolutionary stages underscores the region's dynamic environment, appropriate for investigating the early stages of stellar development. Notably, while M17 SWex's proto-OB association currently lacks very massive stars ($> 20M_{\odot}$), it contains massive cores that are likely to form O stars in the future (Povich & Whitney 2010; Povich et al. 2016), indicating ongoing massive star formation. M17 SWex exhibits dense filamentary structures and is affected by well-aligned magnetic fields perpendicular to these filaments (Sugitani et al. 2019). Furthermore, recent studies of the molecular gas content confirm the spatial and kinematic physical connection between M17 and M17 SWex (Shimoikura et al. 2019; Nguyen-Luong et al. 2020).

Our multi-epoch sub-mm monitoring is part of the extended JCMT Transient Survey (Herczeg et al. 2017; Mairs et al. 2024). Combined with mid-IR data acquired during the NEOWISE mission, we are able to infer and analyze a broad range of variable YSO candidates (e.g. Park et al. 2021). Here our primary objective is to examine the nature of YSO variability across sub-mm and mid-IR wavelengths in the dynamic setting of the massive star-forming region M17SWex.

This paper comprehensively analyzes YSO variability across M17SWex, focusing on observations made at sub-mm and mid-IR wavelengths. Section 2 outlines the observational data employed in this study, including the JCMT Transient Survey and the NEOWISE datasets. In Section 3, we describe the analytical methods used to identify variable sources. Section 4 discusses our findings on the characteristics of variability observed in sub-mm and mid-IR wavelengths within M17SWex, including a brief comparative analysis of these results against the variability observed in low-mass star-forming regions. Finally, Section 5 summarizes our main findings and conclusions.

2. OBSERVATIONAL DATA

2.1. JCMT Transient Survey

The primary aim of the JCMT Transient Survey is to measure sub-mm variability of protostars (Herczeg et al. 2017; Mairs et al. 2024) using the Submillimetre Common User Bolometer Array 2 (SCUBA-2) instrument (Holland et al. 2013) on the James Clerk Maxwell Telescope (JCMT) in Hawaii. The survey initially monitored sub-mm continuum emission in eight star-forming regions, all located in the Gould Belt and within 500 pc of the Sun. In 2020, the program expanded to also include monitoring of fields within four massive star-forming regions (DR21, M17, M17SWex, and S255). These new targets were chosen to include regions with the potential to form a large number of stars, including some very massive stars, while still being relatively nearby, located at distances of $\lesssim 2$ kpc.

Observations are conducted simultaneously at 450 and 850 μm with effective beam sizes of 9''.8 and 14''.6, respectively (Dempsey et al. 2013). For the JCMT Transient Survey, each star-forming region is observed using the PONG1800 mode (Kackley et al. 2010). This mode scans a circular field with a diameter of 30 arcmin, providing uniform background noise across the mapped area. In practice, a somewhat larger 40 arcmin diameter field has sufficient noise uniformity for our analysis. The monitoring cadence for each region is monthly, as long as the region is observable by SCUBA2. The observing time is set by the weather conditions at the

telescope in order to maintain a uniform measurement uncertainty ~ 10 mJy beam $^{-1}$ at 850 μm across epochs. Thus, the 450 μm observations are only occasionally of high enough quality for measurements.

After data acquisition and running of the default JCMT data reduction pipeline, the JCMT Transient Survey utilizes custom image alignment and relative calibration techniques to ensure reliable light curves. Details of the observing methods and reduction techniques can be found in papers by Mairs et al. (2017, 2024), where it is shown that relative calibration between epochs at 850 μm is now close to 1% for Gould Belt regions with roughly 50 measured epochs.

This study focuses on the newly added 850 μm monitoring data set of star-forming region M17SWex, calibrated using the updated Mairs et al. (2024) procedures. The central position of the observed area for M17SWex is located at (R.A., Dec.) = (18^h18^m30^s, -16^d51^m24^s). This region's individual epoch observation dates, weather conditions, quality of each map, and the calibration requirement are provided in Table 1. During our analysis, we discovered that one epoch, taken on 2022-06-28 with a relatively high noise level, was impacted by artifacts such as echoes in the image. The cause of these issues remains uncertain and may have been due to either observational problems or issues at the telescope on that night. To ensure the validity and accuracy of our results, we exclude this epoch from our analysis. The final dataset for this paper consists of 23 epochs of SCUBA-2 850 μm imaging of M17SWex from February 2020 until August 2023.

2.2. WISE/NEOWISE

From January through September 2010, the Wide-field Infrared Survey Explorer (WISE, Wright et al. 2010) surveyed the entire sky using four mid-infrared (mid-IR) bands at 3.4 μm (W1), 4.6 μm (W2), 12 μm (W3), and 22 μm (W4) with angular resolutions of 6''.1, 6''.4, 6''.5, and 12'', respectively. An additional four months of operation followed, utilizing only the short wavelength bands of W1 and W2 during the post-cryogenic mission of the Near-Earth Object WISE (NEOWISE) program (Mainzer et al. 2011). The WISE spacecraft was placed in hibernation in February 2011 and was restarted for the NEOWISE Reactivation mission in September 2013 to survey the entire sky for near-Earth objects (NEOs), including comets and asteroids, using only the W1 and W2 bands (Mainzer et al. 2014). NEOWISE continues to operate, with twice yearly all-sky observations. The data release used here contains

Table 1. JCMT 850 μm Observational Data Summary

Epoch	Date	MJD ^a	Scan	τ_{225} ^b	Noise	FCF ^c
(yyyy-mm-dd)				(mJy beam $^{-1}$)		
1	2020-02-22	58901.73	74	0.036	8.2	1.179
2	2020-05-21	58990.48	35	0.116	11.9	0.984
3	2020-06-23	59023.46	34	0.1	11.6	0.939
4	2020-07-30	59060.35	29	0.055	9.4	1.015
5	2020-09-02	59094.17	16	0.048	7.6	1.0
6	2020-10-10	59132.21	15	0.099	13.9	0.845
7	2021-03-03	59276.75	84	0.041	9.3	1.037
8	2021-04-06	59310.55	46	0.05	8.8	1.038
9	2021-05-17	59351.56	75	0.048	12.6	0.998
10	2021-06-14	59379.39	30	0.056	7.8	1.053
11	2021-08-04	59430.21	15	0.114	16.2	0.893
12	2021-09-08	59465.28	24	0.106	13.6	0.963
13	2021-10-08	59495.18	21	0.062	11.9	0.948
14	2022-03-03	59641.67	53	0.071	9.1	1.102
15	2022-05-23	59722.55	37	0.049	7.1	1.047
16	2022-06-28 ^d	59758.36	48	0.055	18.5	0.752
17	2022-07-29	59789.24	11	0.076	10.4	1.019
18	2022-08-27	59818.27	30	0.054	9.2	1.006
19	2022-10-01	59853.23	16	0.062	10.3	0.964
20	2023-03-28	60031.60	15	0.099	11.0	1.040
21	2023-05-01	60065.54	34	0.106	10.7	1.078
22	2023-06-06	60101.54	54	0.079	11.7	0.964
23	2023-07-15	60140.30	21	0.058	11.6	1.029
24	2023-08-14	60170.30	12	0.062	8.8	0.951

^a Modified Julian Day (MJD) is converted from Julian Day by subtracting 2,400,000.5 from the JD value.

^b The average 225 GHz zenith opacity measured during observations.

^c The Flux Calibration Factor (FCF) represents the factor derived during the relative calibration step and applied to the observatory-defined default calibration factor (Mairs et al. 2024).

^d This epoch is not used in our analysis due to poor image quality.

observations through December 2022¹. For each area of the sky, *WISE* takes 10-20 exposures across a few days, with epochs separated by half a year.

3. ANALYSIS

3.1. A sub-mm source catalog

We employed the FellWalker algorithm (Berry 2015) to identify localized sub-mm sources in the co-added image at 850 μm , generated from the observations of M17 SWEx during the first ~ 1.5 years. Sources are only included in our catalog if they were located within a 20' radius of the map center, thereby excluding the noisy map edges. The mean peak flux of each source was then

¹ https://wise2.ipac.caltech.edu/docs/release/neowise/neowise_2023_release_intro.html

derived from the full co-addeed image (Figure 1), which combined data from all 23 epochs.

We identify 663 sub-mm sources that have an average peak brightness greater than 13 mJy beam $^{-1}$ (see Appendix Table A1). Of these sources, 150 have a mean peak flux above 100 mJy beam $^{-1}$, which is about ten times the mean epoch root-mean-square (RMS) noise (~ 11 mJy beam $^{-1}$; see Table 1), sufficient for secular variability analysis. Three of these bright sources are excluded because they are located near the 20' radius edge and extend beyond it, introducing increased uncertainty in the peak position and brightness.

Our final catalog for in-depth variability analysis consists of 147 targets brighter than 100 mJy beam $^{-1}$. The original list of almost 700 identified sub-mm sources is also investigated through a statistical analysis of the flux variability, as devised by Johnstone et al. (2018). For these fainter sources, however, only large variable brightness events are robustly observable.

3.2. Searching for sub-mm Variables

We evaluate variability of each source by adopting the fiducial standard deviation (SD_{fid}), as implemented by Johnstone et al. (2018). The SD_{fid} for a given source i , with mean peak flux f_m , is computed as

$$\text{SD}_{\text{fid}}(i) = \sqrt{(n_{\text{RMS}})^2 + (\text{RFCF}_{\text{unc}} \times f_m(i))^2}, \quad (1)$$

where n_{RMS} represents the typical RMS noise measured across all epochs, primarily affecting faint sources. We determined n_{RMS} to be 14 mJy beam $^{-1}$ for our target region.² The term RFCF_{unc} denotes the expected relative flux calibration uncertainty between epochs (for more details see Johnstone et al. 2018; Mairs et al. 2024). This term predominately impacts bright sources, and we adopt $\text{RFCF}_{\text{unc}} = 0.015$, corresponding to a 1.5% flux calibration uncertainty. Using the current calibration pipeline, Mairs et al. (2024) find an uncertainty of only 1% for Gould Belt regions. Our use of 1.5% incorporates the additional uncertainty related to the smaller number of observations undertaken to date for M17 SWEx as well as the large scale complexity of the sub-mm emission within the region. Lastly, f_m signifies the mean peak flux of source i .

² We estimate the typical RMS noise (n_{RMS}) associated with source peak flux measurements by requiring the typical calculated standard deviation for faint sources, those with peak flux < 100 mJy beam $^{-1}$, to be similar to SD_{fid} . This noise level is somewhat larger than the typical mean RMS map noise found for each epoch because source measurements are affected by additional factors, such as data reduction processing and recovery within local extended emission.

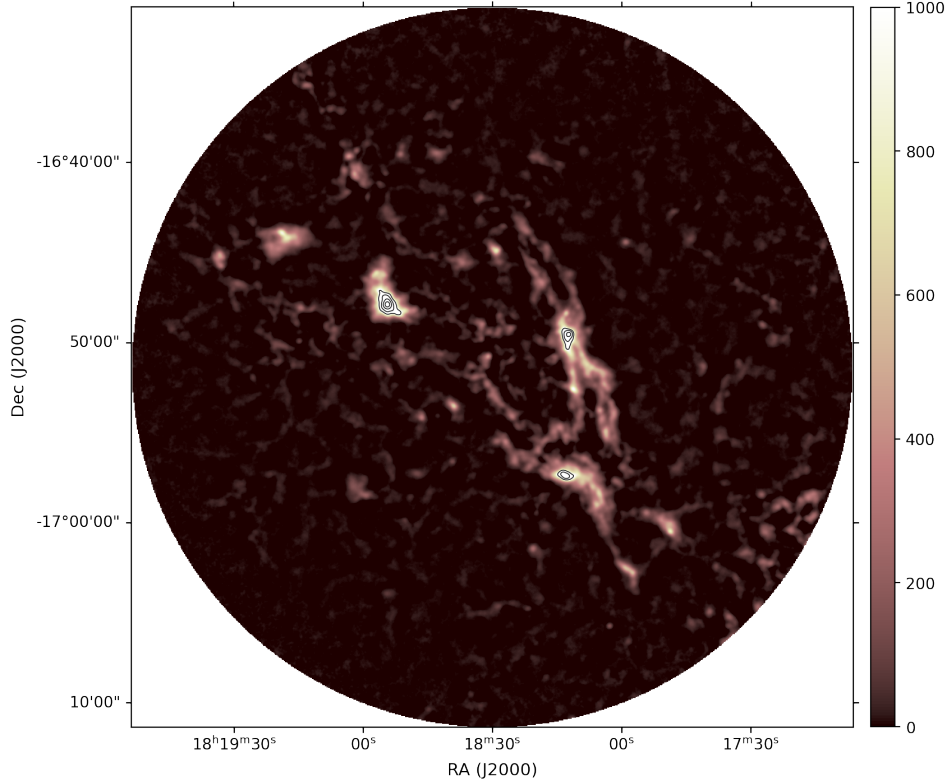


Figure 1. Co-added 850 μm image of M17 SWex using 23 epochs and with contours overlaid at (1100, 2000, 4000, 9000) mJy beam^{-1} .

Using the fiducial standard deviation model, we identify outlier sub-mm sources, as shown in Figure 2a. This figure plots the measured standard deviation of the source peak flux divided by the fiducial model against the mean peak flux for each sub-mm source. The upper right quadrant bounded by the two dashed lines of Figure 2a selects sources that are both bright ($> 100 \text{ mJy beam}^{-1}$) and with significant variability ($\text{SD}/\text{SD}_{\text{fid}} > 2.5$). Only one source lies well within the region and is robustly detected as a variable (see Table 2). We further note that there are no obvious strong outliers among the many fainter sources (upper left quadrant).

Following the method described by Johnstone et al. (2018), we also searched for sub-mm sources varying in brightness linearly with time, secular variables. We used the least-squares linear fit method, implemented in the function ‘scipy.optimize.curve_fit()’, to derive a linear model fit $f_l(i, t)$ for each source i as a function of time t , measured from the first epoch t_0 . The slope $S(i)$, representing the fractional flux change per year, was obtained by using the following equation:

$$f_l(i, t) = f_0(i)(1 + S(i) \times (t - t_0)), \quad (2)$$

where $f_0(i)$ is the initial flux value of the source, and t_0 is the time of the first epoch. We also calculated

the uncertainty in the slope $S(i)$ using the ‘curve_fit’ function, with the expectation that sources with small fractional slope uncertainties indicate robust secular variables. In Figure 2b, we find two bright sources ($> 100 \text{ mJy beam}^{-1}$) with $|S/\Delta S| \geq 3$, where ΔS is the uncertainty in the slope. Neither of these secular sources show significantly enhanced standard deviations (i.e. they do not lie in the upper right quadrant in Figure 2a). Similarly, the variable found to have a significantly enhanced standard deviation in Figure 2a does not have a clear secular variation suggesting that it’s a more stochastic sub-mm source.

Figure 3 shows the light curves of the three identified robust variables. We present the sky locations, potential known matches, and the statistical analysis results for the three sub-mm outliers in Table 2 and further examine them in Section 4.2.

3.3. Searching for Mid-IR Variables

Our investigation into mid-IR flux variability of known YSOs in M17 SWex draws upon the comprehensive catalogs by Povich & Whitney (2010) and Kuhn et al. (2021). Povich & Whitney (2010) conducted a thorough analysis of archival Spitzer GLIMPSE and MIPS-

Table 2. Statistics of Potential Variable Submillimeter Sources

ID	f_m	SD	SD/SD _{fid}	$S/\Delta S$	Type		Nearby Known Source ^a
					Source	Variable	
(1)	(2)	(3)	(4)	(5)	(6)	(7)	(8)
JCMTPP_J181812.2-164933	5409.12	125.06	1.52	5.92	Star-forming	Secular	SPICY 80147, PW2010_293 (4.9'') ^b
JCMTPP_J181803.7-165500	590.95	22.43	1.35	4.39	Star-forming	Secular	AGAL014.131-00.522_S (2.0'') ^c
JCMTPP_J181802.8-170545	153.59	58.34	4.11	1.40	Quasar	Stochastic	NVSS J181802-170542 (3.4''), IVS B1851-171, LQAC_274-017_001 (4.2'') ^d

NOTE— (1) Source ID. JCMTPP stands for JCMT Peak Position, followed by Right Ascension and Declination in h:m:s and d:m:s, respectively.; (2) Mean peak flux in mJy beam⁻¹; (3) Standard deviation in mJy beam⁻¹; (4) The ratio of the standard deviation to the fiducial standard deviation for each source; (5) The absolute value of the slope to its uncertainty ratio; (6) Type of source from literature; (7) Type of variable identified by this work; (8) Known sources that are likely to be associated with the given submm source.

^a Known sources located within a distance of 6''. The values in parentheses are the distance between the submm peak position and each source.

^b YSO cataloged by [Povich & Whitney \(2010\)](#), PW2010 and [Kuhn et al. \(2021\)](#), SPICY.

^c Protostellar clump cataloged by ATLASGAL ([Schuller et al. 2009](#); [Contreras et al. 2013](#); [Urquhart et al. 2014](#)).

^d Extragalactic source. Nearby known sources are listed in order as they appear in the text: [Condon et al. \(1998\)](#), [Petrov et al. \(2011\)](#), and [Petrov et al. \(2011\)](#).

GAL surveys, combined with Two Micron All Sky Survey (2MASS) and Midcourse Space Experiment (MSX) data, to identify 488 candidate YSOs within M17 SWex. This catalog provides a detailed baseline for understanding the initial mass function and the evolutionary stages of YSOs within the cloud complex. [Kuhn et al. \(2021\)](#) expanded on this work by presenting a list of $\sim 120,000$ Spitzer/IRAC candidate YSOs across the Galactic mid-plane, which included the M17 SWex region. Their classification scheme benefited from statistical learning methods tailored to Spitzer's mid-IR capabilities, offering a refined analysis of each objects' nature and the ensemble spatial distribution. Both catalogs employ a classification scheme that identifies YSOs based on their infrared excess, indicative of circumstellar disks or envelopes, which are key markers of early stellar evolution. These works provide a critical framework for our study, offering a catalog of YSOs whose variability we aim to explore in the mid-IR. By using these detailed classifications, we can better understand the mid-IR flux variability in relation to the evolutionary stages of YSOs, from deeply embedded Class 0/I objects to more evolved Class II disks and then Class III sources, within the dynamic environment of M17 SWex. Figure 4 presents a summary flow chart illustrating the mid-IR sample selection process and variability type classification described below.

To allow for direct comparison with the sub-mm observations, we limited the sample of YSOs to those within the boundary of the 40' diameter JCMT field as described in Section 3.1. Within this area, we identify 583 YSOs from the catalogues. These YSOs are predomin-

nantly at an early evolutionary stage, with 34.1% Class 0/I and 50.5% Class II, suggesting that the observed M17 SWex is still at an early stage of star formation. The sample contains only a minor proportion of Class III sources (2.7%), though this is likely due to the complexity of identifying them in distant, dust-obscured, regions. For completeness, ambiguous sources, which cannot be assigned robustly to individual evolutionary classes, make up 12.7% of the 583 YSOs.

To perform our search for mid-IR counterparts, for each source, we first queried the WISE and NEOWISE single exposure catalogues from the NASA/IPAC Infrared Science Archive (IRSA), using a 3'' radius. Then, from all the detections, we determined the average values for the right ascension and declination, and selected single exposures that were located within $2*sd_d$ from the mean location (where sd_d is the standard deviation of the distance from the mean location). The next step was to group all of the exposures that were carried out within a few days of each other, as these represent a specific epoch. From these groups, we discarded the brightest and faintest 15% of the data. Using the remaining 70% of the data we estimate the mean MJD, mean magnitude, mean error, and the standard deviation (in magnitudes) of the exposures for the YSO in the epoch. The measurement error was then calculated by adding, in quadrature, the mean error and the standard deviation within each epoch. This method then provides one epoch of observations every ~ 6 months.

To analyse variability in the sample and ensure high-quality data, we selected sources with a minimum of 12 epochs for which there are mid-IR measurements

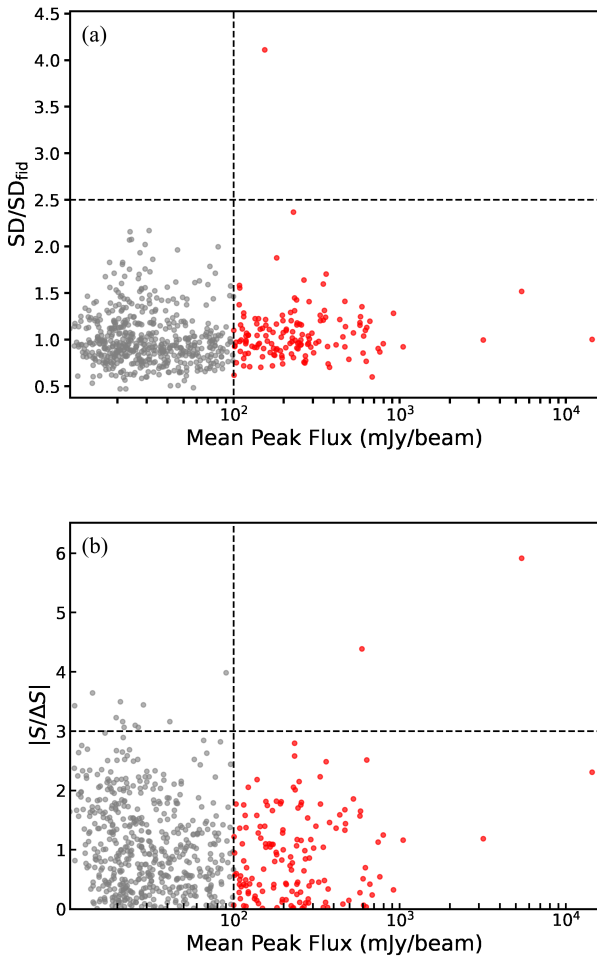


Figure 2. Scatter plots of mean peak flux at 850 μm against (a) the standard deviation of the peak flux normalized by the fiducial model and (b) the absolute value of slope S ratioed to its uncertainty ΔS for sub-mm sources identified in M17SWex. Sources with a mean peak flux greater than $100 \text{ mJy beam}^{-1}$ are shown in red, while all others are in grey. The dashed lines in each panel indicate thresholds used to identify variable candidates. The dashed vertical line indicates a mean peak flux of $100 \text{ mJy beam}^{-1}$, the threshold for sources bright enough for statistical significance. The dashed horizontal line in Panel (a) indicates 2.5 times the fiducial expectation, a threshold for reliability for stochastic variability. The dashed horizontal line in Panel (b) indicates where $|S/\Delta S| = 3$, which is the threshold for reliability for linear variability as defined by Johnstone et al. (2018). The sources that are marked in red in the upper right corners are considered to be robust variables. There is one robust stochastic variable in (a) and there are two robust linear secular variables in (b).

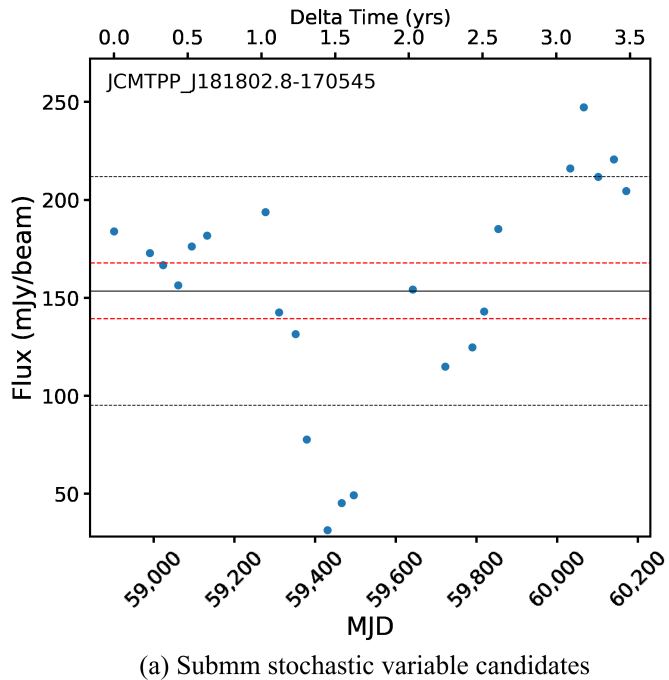
at both W1 and W2, and with a mean uncertainty $\sigma(\text{mag}) < 0.2 \text{ mag}$. Among the 583 known YSOs in M17SWex, 185 met the observation threshold with at least 12 epochs. Applying as well the measurement uncertainty requirements, we identified 156 YSOs at W1 and 179 at W2. Figure 4 records the numbers of sources recovered throughout the sample selection and variability classification process. This mid-IR-detected sample is dominated by Class 0/I and Class II sources, which together make up 95% of the ensemble, a slightly larger fraction of early stage sources than in the original sample of 583. Figure 5a displays the distribution of the known YSO classes and the mean W1 and W2 magnitudes of the final sample objects selected for light curve analysis.

In accordance with the YSO class nomenclature outlined by Park et al. (2021), we classify 156 objects in W1 and 179 objects in W2 into four categories: Class 0/I³; (33.8% in W1 and 34.4% in W2), Class II (60.5% in W1 and 60.6% in W2), Class III (3.2% in W1 and 2.8% in W2), and ambiguous (2.5% in W1 and 2.2% in W2). This information, and comparison against the full YSO sample for M17SWex, is shown graphically in Figure 5b.

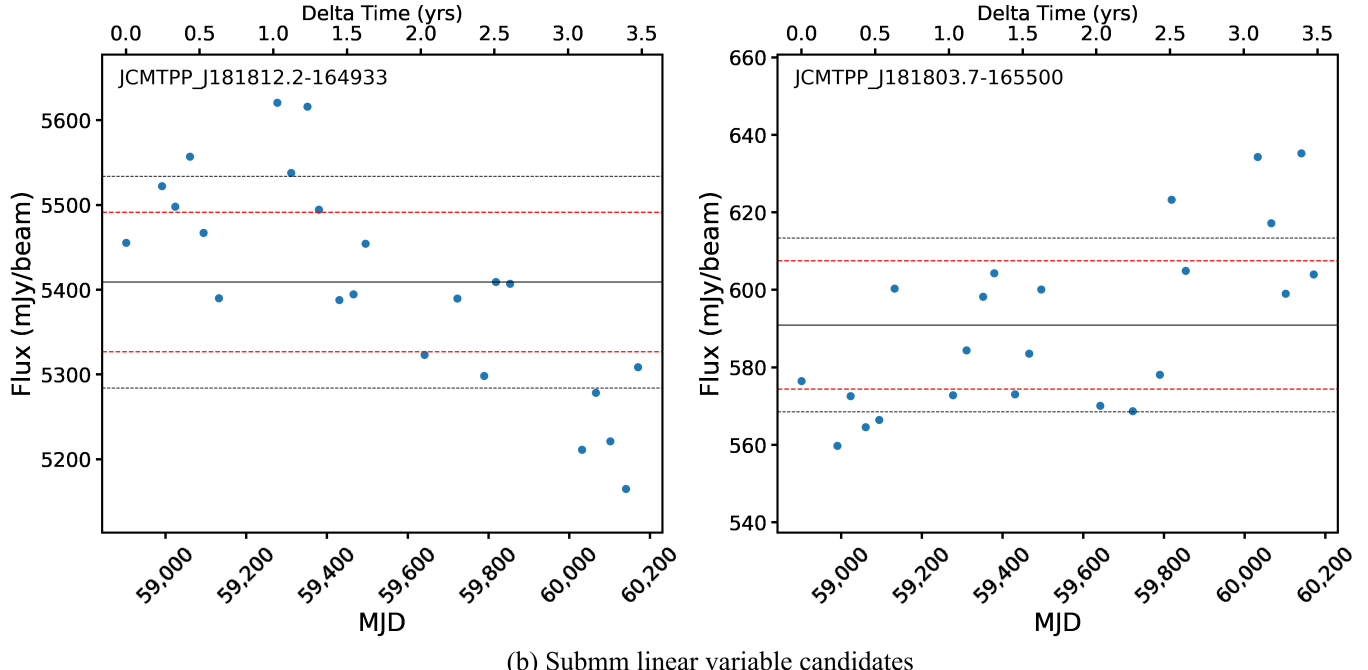
The mid-IR light curve analysis for low-mass protostars performed by Park et al. (2021) focused on the WISE W2 band, and identified variable sources exhibiting various types of behavior. In this study we slightly modify this technique to fit the M17SWex sample, and apply the analysis to both W1 and W2 data sets. In the first step to analyse variability, we convert W1 and W2 magnitudes to fluxes. From these, we estimate a standard deviation (SD) and a mean flux uncertainty (σ or SD_{fid} , see Contreras Peña et al. 2020; Park et al. 2021). The value of SD/SD_{fid} serves as a normalized measure of variability, accounting for the expected fluctuations in the data. Previous works have used this parameter and found that selecting sources with $SD/SD_{fid} > 3$, provides a reliable list of candidate variable YSOs (Contreras Peña et al. 2020).

Figure 6 shows the amplitude of variability $\Delta(\text{max-min})$, the difference between the maximum and minimum magnitudes, versus SD/SD_{fid} for both W1 and W2. Similar to the conclusions by Park et al. (2021), the figure shows that numerous sources exhibit strong brightness variations even when their SD/SD_{fid} values fall below 3. This highlights the importance of thoroughly analyzing all sources, even those with lower SD/SD_{fid} values, to understand their variability behavior fully.

³ For this classification also includes flat SED YSOs.



(a) Submm stochastic variable candidates



(b) Submm linear variable candidates

Figure 3. The light curve of potential stochastic (a) or linear (b) variable sub-mm candidates based on the 23 epochs of JCMT observations. The black solid and dotted lines represent the mean and $\pm 1\sigma$ standard deviations, while the red dotted lines show the expected fiducial standard deviations. The upper x-axis indicates the time relative to the first epoch.

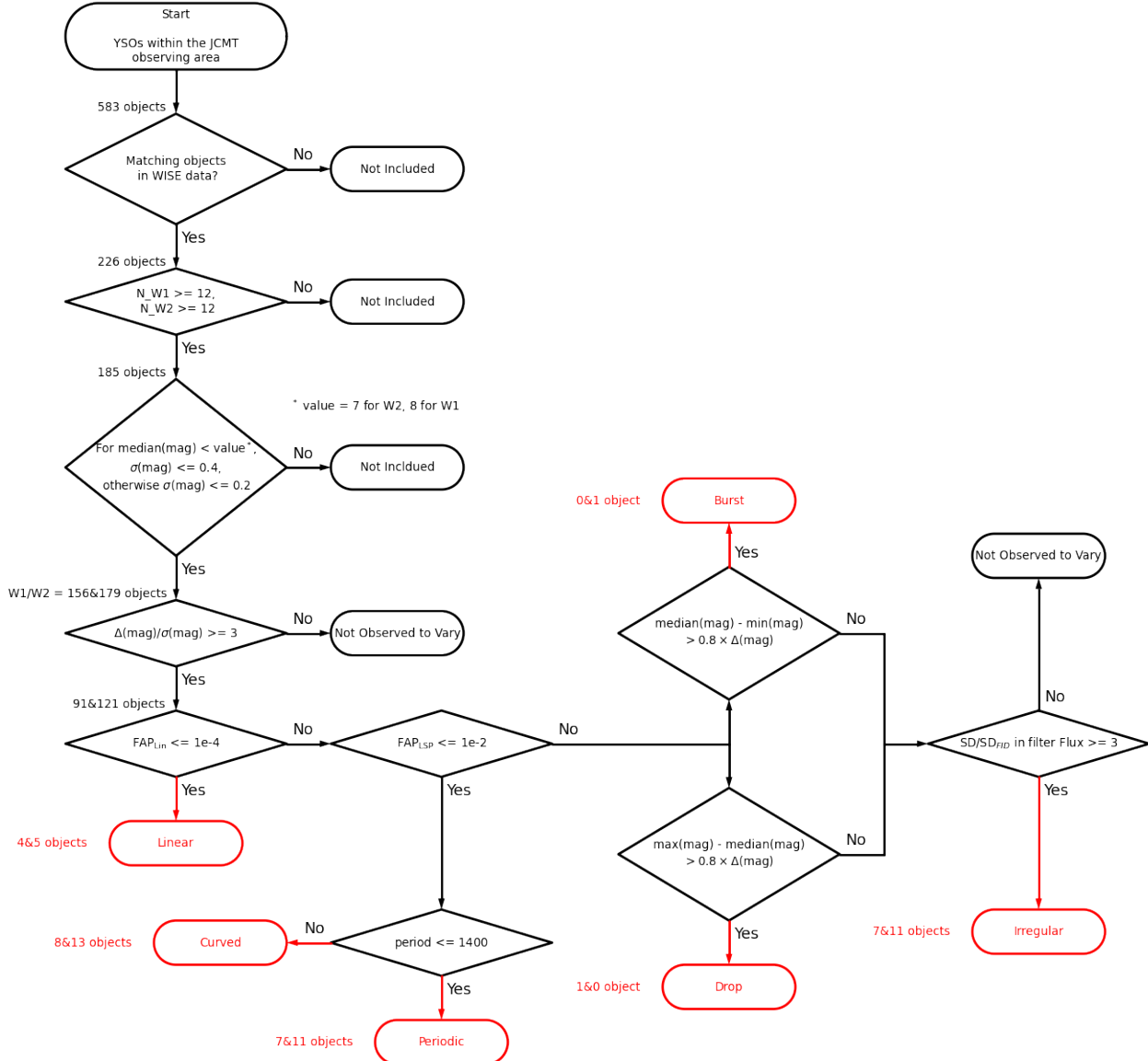
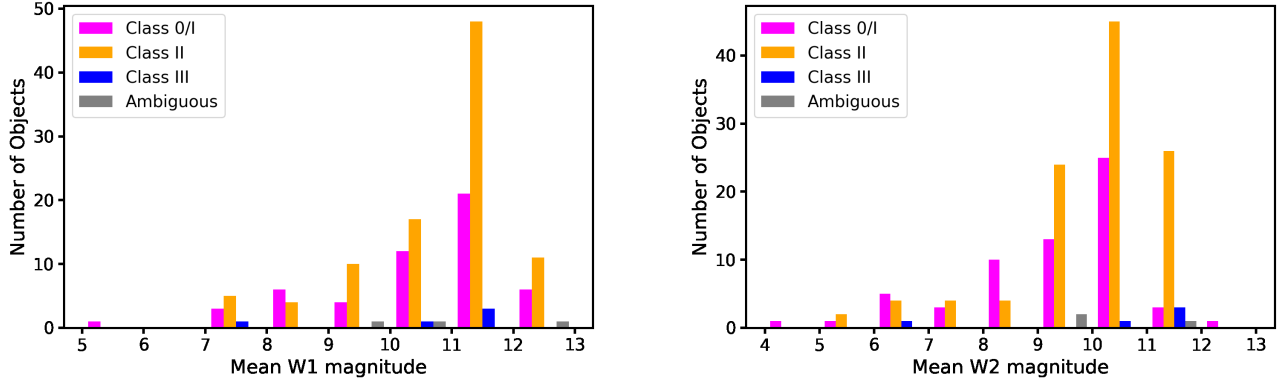
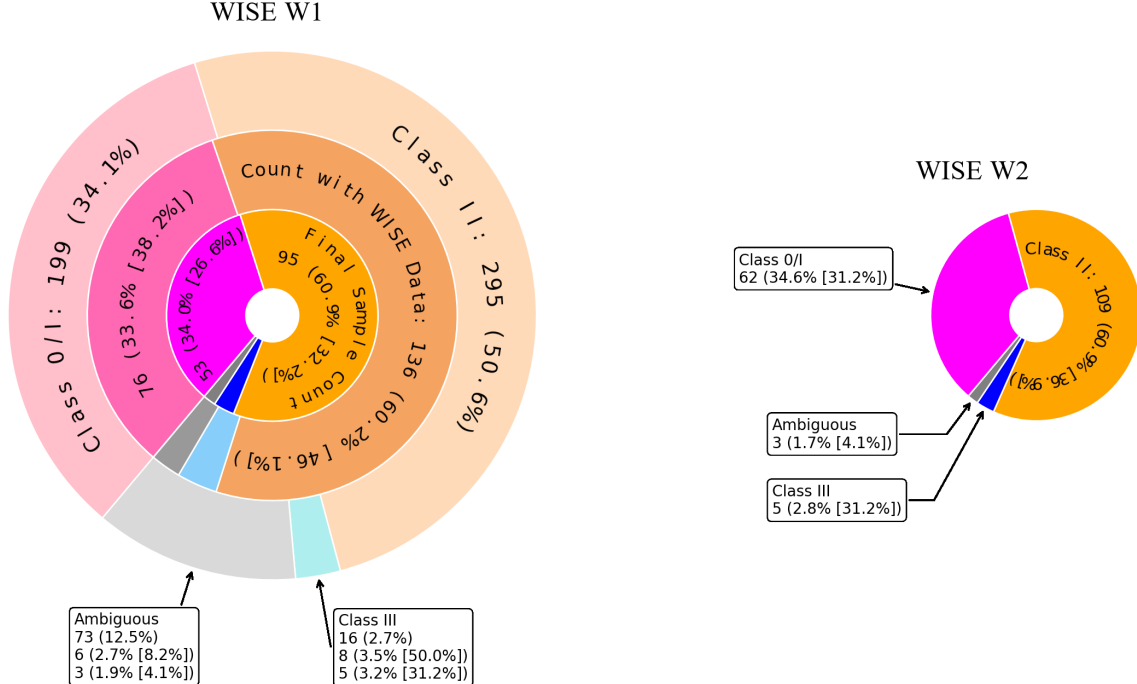


Figure 4. Summary flow chart outlining the mid-IR sample selection and light curve variability classification process. Our methodology, based on the approach used by Park et al. (2021), identifies six types of variables, secular (linear, periodic, curved) and stochastic (burst, drop, irregular), among known YSO candidates in the WISE W1 and W2 bands (refer to Section 3.3 for additional details). The quantity $\Delta(\text{mag})$ represents the difference between the maximum and minimum values of the magnitude, while SD and $\sigma(\text{mag})$ (or simply σ) denote the standard deviation and mean uncertainty of magnitudes across all epochs for a given source. This methodology was applied to each band separately. The number of objects that satisfy each flow chart criteria are indicated in the figure. Where two numbers are provided, the first is for W1 and the second for W2.



(a) YSO classes and mean magnitudes for the final WISE sample



(b) YSOs classes and selection of final WISE sample

Figure 5. Overview of YSO classification and data selection: (a) Distribution of mean magnitudes for the final sample of YSOs across different evolutionary stages: Class 0/I, Class II, Class III, and ambiguous classifications, shown in magenta, orange, blue, and gray, respectively. (b) Nested pie charts representing population statistics for YSOs at various stages of data collection and analysis for both WISE W1 and W2 bands. Each segment within the charts corresponds to a distinct YSO type, with the outer ring representing the total count of that type, the middle ring showing those with WISE data, and the innermost ring indicating the count in the final sample. The percentages on the pie charts reflect the proportion of each YSO type within the respective layer and the percentage of the total count for each YSO type.

Park et al. (2021) classified variable behavior into six distinct categories, which can be grouped into three secular and three stochastic variability categories.

Secular variability includes the following behaviors:

- Linear: These sources display straight-line changes in brightness over time, either increasing or decreasing steadily;
- Periodic: These sources exhibit regular, repeating brightness variations over time. Such periodicity can arise from a variety of astrophysical phenomena, including cycles of long-duration obscuration, binary interactions, or repetitive bursts. These mechanisms often involve interactions within the star-disk system or between binary components, leading to observable periodic changes in the systems' overall brightness (e.g., Bouvier et al. 2013; Grankin et al. 2008; Herbst et al. 2010; Cody et al. 2014; Hodapp et al. 2012; Yoo et al. 2017);
- Curved: These sources show continuous, non-linear brightness changes that do not repeat over our time baseline. This variability may arise from evolving circumstellar material, disk instabilities, or inner disk height changes. Some curved objects might later be reclassified as periodic with longer observations.

Stochastic variability includes:

- Burst: These sources exhibit sudden, short-lived increases in brightness, potentially resulting from episodic accretion events or flaring activity;
- Drop: These sources display abrupt, transient decreases in brightness that may be attributed to brief extinction events, possibly arising from the geometric properties of disks;
- Irregular: These sources show unpredictable, erratic variations in brightness without any discernible pattern, possibly due to a combination of several underlying mechanisms or chaotic processes. A sparse sampling of light curves may cause some YSOs with periodic variability to be misclassified as irregular (Lee et al. 2020).

Following the schematic flowchart in Figure 4, we first examined sources with $\Delta(\max - \min)/\sigma(\text{mag}) \geq 3$ to investigate the presence and type of variability. Here, $\Delta(\max - \min)$ represents the difference between the maximum and minimum values of the W1 or W2 magnitude, and $\sigma(\text{mag})$ denotes the mean uncertainty of the W1 or W2 bands across all epochs for a given source.

The criterion of $\text{SD}/\text{SD}_{\text{fid}} > 3$ is commonly used to identify variable sources. However, this threshold may not be effective in detecting all types of variability. For instance, secular variables may have low standard deviation due to an underlying regular pattern and weak slope, while stochastic variability may occur at only one epoch, leading to a low standard deviation over the entire light curve. To address these issues, Park et al. (2021) set an alternative criterion of $\Delta\text{mag}/\sigma(\text{mag}) \geq 3$ in the magnitude domain to search for variability. Out of 156 sources at W1, we find 91 or 58% that should be further checked for variability. At W2, 121 of 179 (68%) are potential variables.

The Lomb-Scargle periodogram (LSP; Lomb 1976; Scargle 1989) and a linear fitting are the secular models used in our analysis. The robustness of the secular variability is evaluated from the false alarm probability (FAP). The LSP FAP quantifies the likelihood of identifying a spurious signal in an LSP, whereas the linear FAP estimates the probability of falsely detecting a linear trend. However, the traditional LSP FAP can provide a systematic overestimate of the false alarm probability for long periods (Park et al. 2021; Lee et al. 2021b). Therefore for the LSP fit we used a modified version, which though labelled FAP_{LSP} takes that same form as the FAP_{mod} introduced by Lee et al. (2021b).

In Figure 7, we compare the FAP for linear and periodic fits for our M17 SWex samples at W1 and W2. Sources with $\text{FAP}_{\text{Lin}} \leq 10^{-4}$ are classified as exhibiting linear variability. Among the remaining sources, those with $\text{FAP}_{\text{LSP}} \leq 10^{-2}$ and a period of 1400 days or shorter, which corresponds to about half of the eight years covered by the WISE data used in our analysis, are identified as displaying periodic variability. Conversely, sources with $\text{FAP}_{\text{LSP}} \leq 10^{-2}$ and a period longer than 1400 days are classified as exhibiting curved variability. From the W1 sample, we identify four linear, nine curved, and seven robust periodic variables. The W2 sample yields five linear, thirteen curved, and eleven periodic variables.

We apply an additional constraint to identify sources that exhibit either bursts or drops in brightness while maintaining stable fluxes over the remaining epochs. Specifically, we require either $\text{median}(\text{mag}) - \text{min}(\text{mag}) > 0.8 \times \Delta(\text{mag})$ for burst sources or $\text{max}(\text{mag}) - \text{median}(\text{mag}) > 0.8 \times \Delta(\text{mag})$ for drop sources. After excluding all previously identified sources, those with $\text{SD}/\text{SD}_{\text{fid}} \geq 3$ are classified as showing irregular variability.

For the W1 sample, we identified one drop and seven irregular variables but no burst variable. The W2 sample, on the other hand, yielded one burst and eleven

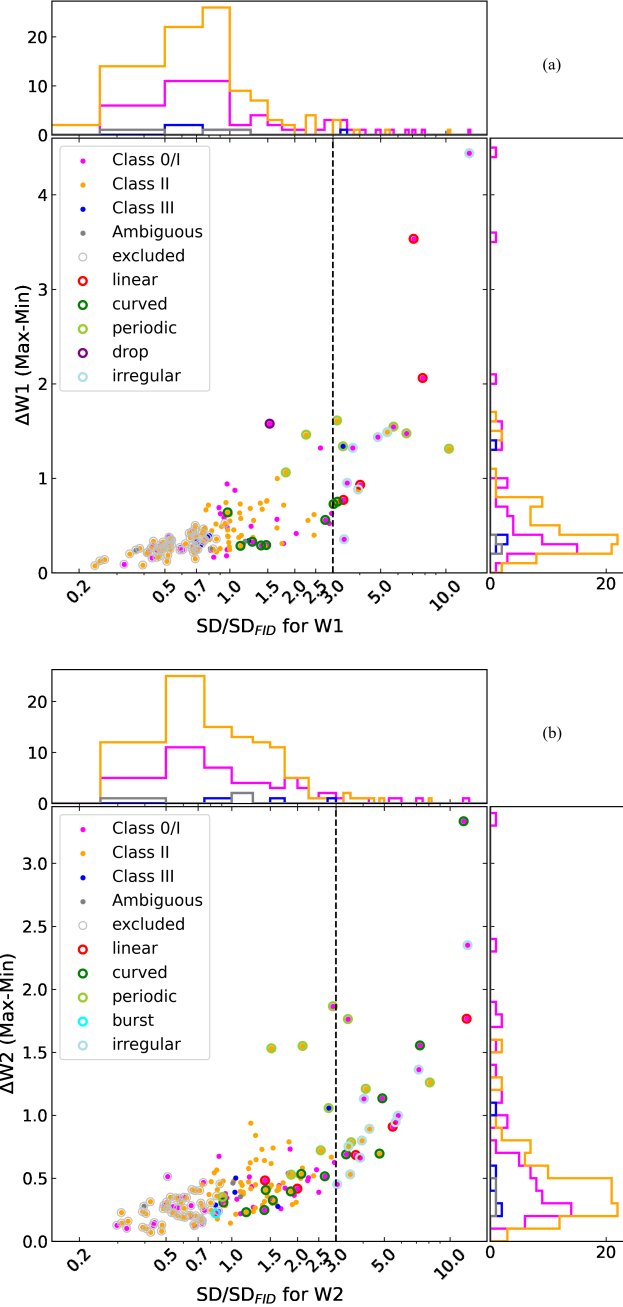


Figure 6. Comparison of SD/SD_{fid} and Δmag for all sources in the final samples of W_1 (a) and W_2 (b). The dashed vertical line indicates the commonly used threshold value of SD/SD_{fid} equal to 3 for identifying sources with brightness variability. The classification of YSOs is indicated by the filled circle colors, which are consistent with those used in Figure 5. Variable candidates among the YSOs are denoted by a bordered circle, with the color of the border circle indicating the type of variability, while sources that were excluded during the analysis because they have a $\Delta mag/\sigma(mag) < 3$ are marked with the gray bordered circle.

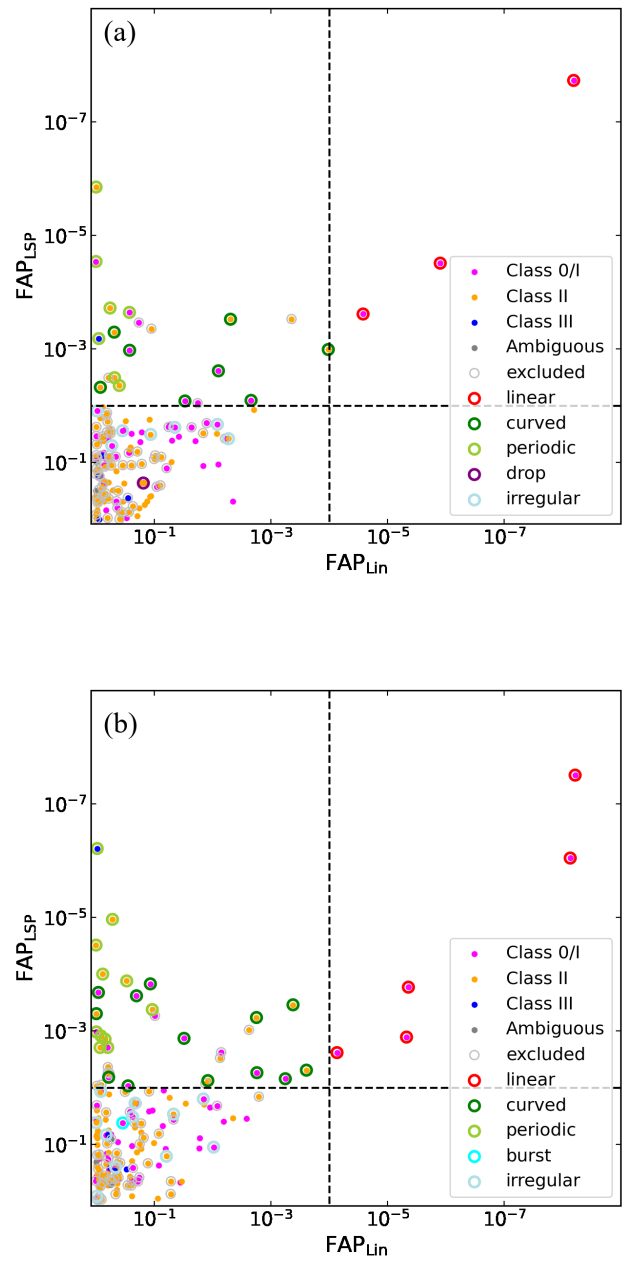


Figure 7. Comparison of the FAPs for linear and periodic fits for all sources in the final samples of W_1 (a) and W_2 (b). The dashed vertical line represents a FAP of 10^{-4} for the linear fit, while the dashed horizontal line represents a FAP of 10^{-2} for the periodic fit. Symbols and colors used in this figure are consistent with those presented in Figure 6, representing different evolutionary stages and the five types of mid-IR flux variability identified in our study.

irregular variables but no drop variable. Further discussion and analysis of these findings, supported by light curve data, is presented in Section 4.3.

Table 3 summarizes the statistical results from our independent variability investigations using WISE W1 and W2. We present the YSOs that are robust mid-IR variables across the six types, along with their corresponding evolutionary stages. Combined, 47 YSOs exhibit robust variability at either W1 or W2, including 21 YSOs that vary in both bands. Interestingly, while 14 display the same type of variability in both bands, 7 are classified into somewhat different variability types. Upon closer examination of the light curves for these seven cases, multiple phenomena appear to be at play. The remaining 26 YSOs are variable in just one of the two bands, with 7 variable in W1 and 20 in W2. This disparity in variability across the two bands will be examined in further detail, including an analysis of their light curves, in Section 4.3.1. For completeness, we present in Table B2 and B3, the variability measures derived from the NEOWISE light curves for both the final sample of variable candidates identified in this study (Table B2) and the remaining sources from the final sample that were not observed to vary (Table B3).

4. DISCUSSION

4.1. Spatial Coincidence of Sub-mm and Mid-IR Sources

This study focuses on the variability of sources at both sub-mm and mid-IR wavelengths within the same field of view centered on M17SWex. While the two wavelengths may respond to different time-dependent processes, the expectation is that for YSOs the long-term light curves are indicators of any underlying mass accretion variability onto the central source. Previously, such connections between mid-IR and sub-mm have been observed for nearby star-forming protostars by Contreras Peña et al. (2020); Lee et al. (2020); Yoon et al. (2022).

Figure 8 illustrates the spatial distribution of source peaks in our observed area at both sub-mm and mid-IR wavelengths. The co-added 850 μm map from 23 epochs in Figure 8a reveals the sub-mm peak locations and the three robust sub-mm variables. Similarly, Figures 8b–8c display the WISE W1 and W2 images from the first epoch (March 2014), showing the locations of all YSO candidates located within our JCMT surveyed area and highlighting the mid-IR variables. The sub-mm sources with a mean peak flux exceeding 100 mJy beam $^{-1}$ usually reside within sub-mm filamentary structures. Furthermore, numerous WISE-associated YSOs are situ-

ated along these same filaments, as expected for stars forming out of the prenatal molecular cloud material. Notably, our observation area also includes some isolated YSOs identified by Kuhn et al. (2021) that may not have a direct association with M17SWex.

While we identify variability independently for each wavelength, we specifically examine the spatial correlation of the sources without delving into their detailed properties. We chose a maximum separation of 3'' between the sub-mm peaks and the YSO candidates when matching. This value is based on the relative pointing accuracy of the JCMT, which is typically better than 2'' (Mairs et al. 2024), the localized nature of the mid-IR fluxes, and the desire for the peaks to remain within a typical core scale (5000 au) separation. Only seven YSOs from the Povich & Whitney (2010) and Kuhn et al. (2021) catalogs match the location of sub-mm peaks in the SCUBA-2 images. Among these seven matched YSOs, only three have corresponding WISE measurements. Finally, among the three matching YSOs, no source shows sub-mm flux variation, even though two of the sources, SPICY 79425 and 80368, show mid-IR flux variability in both WISE bands. This matching compares the observed sub-mm peaks with YSOs that also have NEOWISE measurements within a tight matching distance of \sim 5000 au. YSOs that reside within the sub-mm filaments may not live at the peaks, since this may be where new star formation is about to occur. Similarly, sub-mm peaks may be optically thick to mid-IR wavelengths and thus may hide the most recent star formation. Both of these situations are seen in nearby star-forming regions, where angular resolution allows for a clearer investigation of the connection between the sub-mm and mid-IR images.

Some additional difference between the sub-mm and mid-IR variability may be introduced by the distinct observation intervals and total monitoring periods. These two datasets only overlap during the last three years of the WISE observations. Furthermore, the cadence in the sub-mm is roughly monthly whereas in the mid-IR the epochs are only twice per year. Thus, the sub-mm has a much higher temporal resolution than the mid-IR, while the mid-IR has an extended observational baseline of about nine years, three times longer than the sub-mm observations considered here.

4.2. Individual Sub-mm Variables

In our study of the M17SWex region, three sources exhibiting sub-mm variability at 850 μm are identified (see Table 2). For simplicity, we here refer to these sources by just their right ascension, for example JCMTPP_J181812.2. To investigate the connection

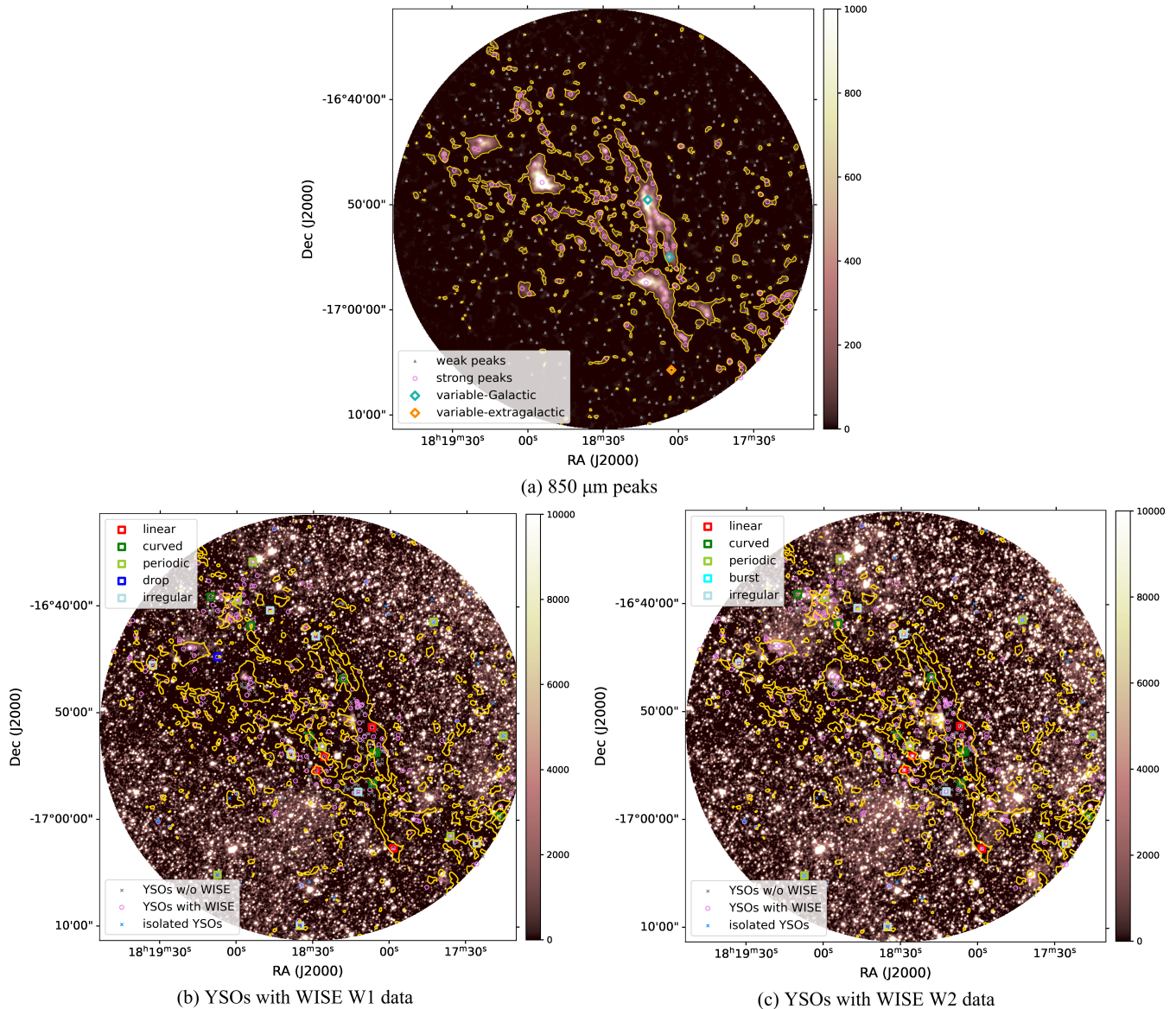


Figure 8. Positions of target source peaks within the M17 SWex observation area at sub-mm (a) and mid-IR (b–c). The 850 μm image in (a) is a co-added image from 23 epochs, with a 30 mJy beam⁻¹ contour overlaid. Target source peaks with a mean peak flux greater than 100 mJy beam⁻¹ are marked with pink circles, while those with a mean peak flux less than 100 mJy beam⁻¹ are shown with gray triangles. Three sub-mm robust variables are highlighted with teal and orange diamonds. The mid-IR images in (b–c) show WISE W1 and W2 data acquired during the first epoch used (March 2014), overlaid with the 850 μm contour shown from the (a) image. YSOs within our JCMT-observed area are marked: pink circles indicate those identified with WISE data, while gray crosses indicate those not identified. Additionally, royal-blue crosses mark YSOs cataloged by Kuhn et al. (2021) that were not included in any group in their study. Colored squares highlight mid-IR variables identified in this study. The color scales are displayed on the right side of each map, and the units are (a) mJy beam⁻¹ and (b,c) arbitrary counts.

Table 3. Variable Type by YSO Classification in WISE W1 and W2

Type	W1					W2				
	(Class 0/I, FS)	(Class II)	(Class III)	(ambiguous)	Total	(Class 0/I, FS)	(Class II)	(Class III)	(ambiguous)	Total
Count	53	95	5	3	156	62	109	5	3	179
Linear	4 (7.5)	0 (0)	0 (0)	0 (0)	4	5 (8.1)	0 (0)	0 (0)	0 (0)	5
Curved	4 (7.5)	4 (4.2)	0 (0)	0 (0)	8	8 (12.9)	5 (4.6)	0 (0)	0 (0)	13
Periodic	2 (3.8)	4 (4.2)	1 (20)	0 (0)	7	2 (3.2)	8 (7.3)	1 (20)	0 (0)	11
Burst	0 (0)	0 (0)	0 (0)	0 (0)	0	1 (1.6)	0 (0)	0 (0)	0 (0)	1
Drop	1 (1.9)	0 (0)	0 (0)	0 (0)	1	0 (0)	0 (0)	0 (0)	0 (0)	0
Irregular ^a	5 (9.4)	2 (2.1)	0 (0)	0 (0)	7	7 (11.3)	4 (3.7)	0 (0)	0 (0)	11
All Variables	16 (30.2)	10 (10.5)	1 (20)	0 (0)	27	23 (37.1)	17 (15.6)	1 (20)	0 (0)	41

NOTE—Numbers are the count of variables for each variable type, while numbers in parentheses are the fraction (%) of variable candidates relative to the numbers in the “Count” row, which denote the selected WISE samples in each evolutionary stage (see Section 3.3).

^aSources with $SD/SD_{fid} \geq 3$ but not classified as any previous specific type of variability.

between the observed sub-mm flux variability and previously identified star-forming activity, we searched for nearby YSOs within a radius of 6'' of the three sub-mm variable candidates.

The first source, JCMTPP_J181812.2, has a mean peak flux of ~ 5400 mJy beam $^{-1}$ with a linear decrease since 2021 (Figure 3). This bright sub-mm source is located near a YSO identified by Kuhn et al. (2021), at a separation of about 4''.9. The YSO is classified with a flat SED, placing it in a transitional phase between embedded (Class I) and optically visible (Class II)⁴. Unfortunately, this YSO is not detected in the WISE database, precluding the analysis of its mid-IR variability. The proximity of the YSO to our sub-mm source, despite the somewhat significant separation, raises the possibility of a physical association. Given the distance to M17 SWex it is likely that the sub-mm emission is tracing a larger concentration of dust and gas than a single protostellar core and therefore the peak dust emission may well be offset from any specific embedded protostar, responsible for localized heating. We thus consider JCMTPP_181812.2 a clump housing a candidate variable protostar.

The second sub-mm variable, JCMTPP_J181803.7, is comparatively weaker, with a mean peak flux of about 590 mJy beam $^{-1}$, and exhibits a linear increase in flux since 2020 (Figure 3). It is also undetected by WISE. Unlike the brighter source, this weaker sub-mm source does not have a confirmed nearby YSO in the Povich & Whitney (2010) or Kuhn et al. (2021) catalogues. The source peak is, however, within 2'' of the ATLASGAL clump AGAL014.131-00.522_S (Schuller et al. 2009; Contreras et al. 2013; Urquhart et al. 2014), catalogued as part of an unbiased survey of the Galaxy designed to identify high-mass clumps. The source has subsequently been classified as a protostellar clump, labelled AG0821, by Rathborne et al. (2016) based on association with either 4.5 μm emission or compact 24 μm emission. We therefore suggest that the sub-mm variability arises from an unseen protostellar source.

The third sub-mm variable, JCMTPP_J181802.8, has the faintest peak brightness, ~ 150 mJy beam $^{-1}$, among the three and lacks any known nearby YSO. Instead, it is coincident, separation of 4'', with a nearby compact radio source, NVSS J181802-170542 (also known as IVS B1815-171 and LQA 274-017_001), potentially of

extra-galactic origin. Long-timescale stochastic variability of this source is evident from the standard deviation analysis and a visual inspection of its light curve (see Figure 3), which shows fluctuations but no clear secular pattern. The brightness remains stable for the first seven epochs before experiencing a significant decrease from the 7th to the 11th epoch, corresponding to about 153 days. Subsequently, the flux experiences a gradual increase accompanied by fluctuations. The light curve again decreases during the final three epochs. While notably variable at 850 μm , this sub-mm source is too faint to be detected in our JCMT 450 μm observations and lacks a visible counterpart in the WISE source catalog. It is probable that this radio source is a quasar. Quasars are known to often show strong variability across a large range of wavelengths.

Intriguingly, the identification of JCMTPP_J181802.8, a potential extragalactic source showing significant sub-mm variability, echoes findings from a previous study within the JCMT Transient Survey which also uncovered an extragalactic variable source, most likely a blazar (Source 2864 in NGC 2023, Johnstone et al. 2022), showcasing the survey's unexpected capability to detect not only YSOs but also distant active galactic nuclei (AGNs). These findings underscore the importance of considering extragalactic contamination when interpreting variability in sub-mm observations of star-forming regions and highlights the survey's potential as a tool for identifying and studying blazars and other variable AGNs, perhaps in combination with interferometric monitoring as analysed by Bonato et al. (2018).

4.3. Mid-IR Variables

Using the classification of sources in M17 SWex by Povich & Whitney (2010); Kuhn et al. (2021) we find that the Class 0/I (protostars) evolutionary stage of YSOs are observed to be the most variable at mid-IR wavelengths. First, the fractional number of variable protostars is higher than for the Class II sources, as shown in Table 3. In the W1 band, approximately 30% of the protostars show variability, compared to about 11% of those at the Class II stages. Similarly, in the W2 band, around 37% of protostars are variable, while nearly 16% of Class II sources exhibit variability. Furthermore, the protostars also have the largest amplitude of variability (Figure 6).

As recognized by Park et al. (2021), many of the periodic variables might be contaminant AGB stars, especially for sources classified as Class II or Class III stage. Consideration of Table 3 reveals that accounting for this potential contamination only strengthens the argument that earlier evolutionary stages of star formation

⁴ Kuhn et al. (2021) uses the [4.5]-[8.0] colour of the source to determine a value of the spectral index, α , that yields a flat SED classification. However, using the MIPS 24 μm detection and equation 7 in Kuhn et al. (2021), we determine $\alpha=0.43$, consistent with a Class I YSO. The source is too faint for a clear detection with WISE.

are more likely to show mid-IR variability. Accurate determination of genuine PMS variability and potential AGB star contamination requires a multifaceted approach, such as searching for maser emission (Lee et al. 2021a) or utilizing a multi-wavelength approach (Groenewegen 2022).

4.3.1. Comparing Variability Across WISE Bands

Our analysis has identified 26 instances of variability that is robustly detected in only one of the WISE bands (W1 or W2), which are closely spaced in wavelength. Furthermore, of the 21 sources determined to robustly vary in both bands, 14 are assigned different variability types in the two bands when using the automated classification procedure. Together this raises intriguing questions about the underlying causes of these observed differences.

Figure 9 shows several representative light curves, including some that effectively illustrate this disparity in variability between bands. SPICY 80368 and 80463 exhibit nearly identical light curves with only subtle variations, and flux variability was confirmed in both W1 and W2 bands for these sources. SPICY 80128 and 81009 display flux variability in both bands, but a robust detection was only achieved for W2, where the measurement uncertainties were smaller. Similarly, weak but robust variability is observed only in W2 for SPICY 81226 and GLMA G014.2370–00.5063. Finally, an interesting source, SPICY 81451, shows widely divergent trends in the two WISE bands.

These examples provide a guide for us to understand differences in assessing variability in W1 and W2. Differences in variability classification across the two mid-IR wavelengths may be due to either sensitivity issues, for instance extinction making one band much fainter than the other, or physical processes in which the variations have wavelength dependence, including emission line contamination for W2 (Yoon et al. 2022). To investigate these possibilities, we employ the Spearman rank correlation test to assess the correlation between individual source light curves at W1 and W2. This non-parametric test was chosen due to its effectiveness in identifying monotonic relationships between two variables, making it suitable for analyzing light curve trends. Our study involves a Spearman correlation analysis using both the initial observational data and outcomes from simulated datasets.

Initially, we apply the Spearman correlation test to obtain correlation coefficients and corresponding p-values to assess the presence of and significance of correlations between the W1 and W2 light curves. Recognizing the potential influence of measurement uncertainties, we

then extend our analysis to simulated datasets to further assess the reliability of these correlations. To account for potential measurement uncertainties, we generate 100 simulated light curves for each source for both W1 and W2 bands. Each simulated light curve is created by adding normally distributed random noise to the corresponding data points from the original light curve. The standard deviation of this noise is set equal to the observational uncertainty associated with each original data point. This method, implemented using `np.random.normal`, is designed to account for the potential impact of measurement errors on the correlation analysis. The Spearman correlation test is reapplied to each of these 100 simulated datasets for every source. We then compare the mean values of the correlation coefficients and p-values obtained from the simulations with those from the original dataset. This comparison offers insights into the stability and reliability of our results under the influence of observational uncertainties.

By analyzing both the observed and simulated data, we determine the correlation between the WISE W1 and W2 band light curves. The results are listed in Table B2. For the 21 sources displaying robust measurable variations in both W1 and W2 bands, 19 had strong positive correlations and two had moderate-to-strong positive correlations. Thus, despite the fact that sometimes these sources were classified differently by band, the light curves appear to be predominantly responding in the same manner, reflecting the same underlying physical conditions.

The 26 sources that showed variability in only one band present a more varied distribution of Spearman correlation agreement. Ten sources were categorized as having a strong positive correlation, five as having a moderate-to-strong correlation, seven as having a weak-to-moderate correlation, and four as having no or very weak correlation. For the fifteen sources, 58%, exhibiting variability in only one WISE band (W1 or W2) and displaying a strong or moderate-to-strong positive correlation, it is expected that the same astrophysical phenomena are influencing both bands. The variation in the other band might be too subtle or weak for our detection methods to identify. This is also possible for the 7 sources, or 27%, showing variability in only one band and exhibiting a weak-to-moderate Spearman correlation, though additional caution should be exercised for this small subset. While the same physical phenomenon may affect both bands, the weak correlation could also indicate that the connection is not as direct or that other factors influence the observed variability. These cases might require more in-depth analysis or additional data to clarify the nature of the variability.

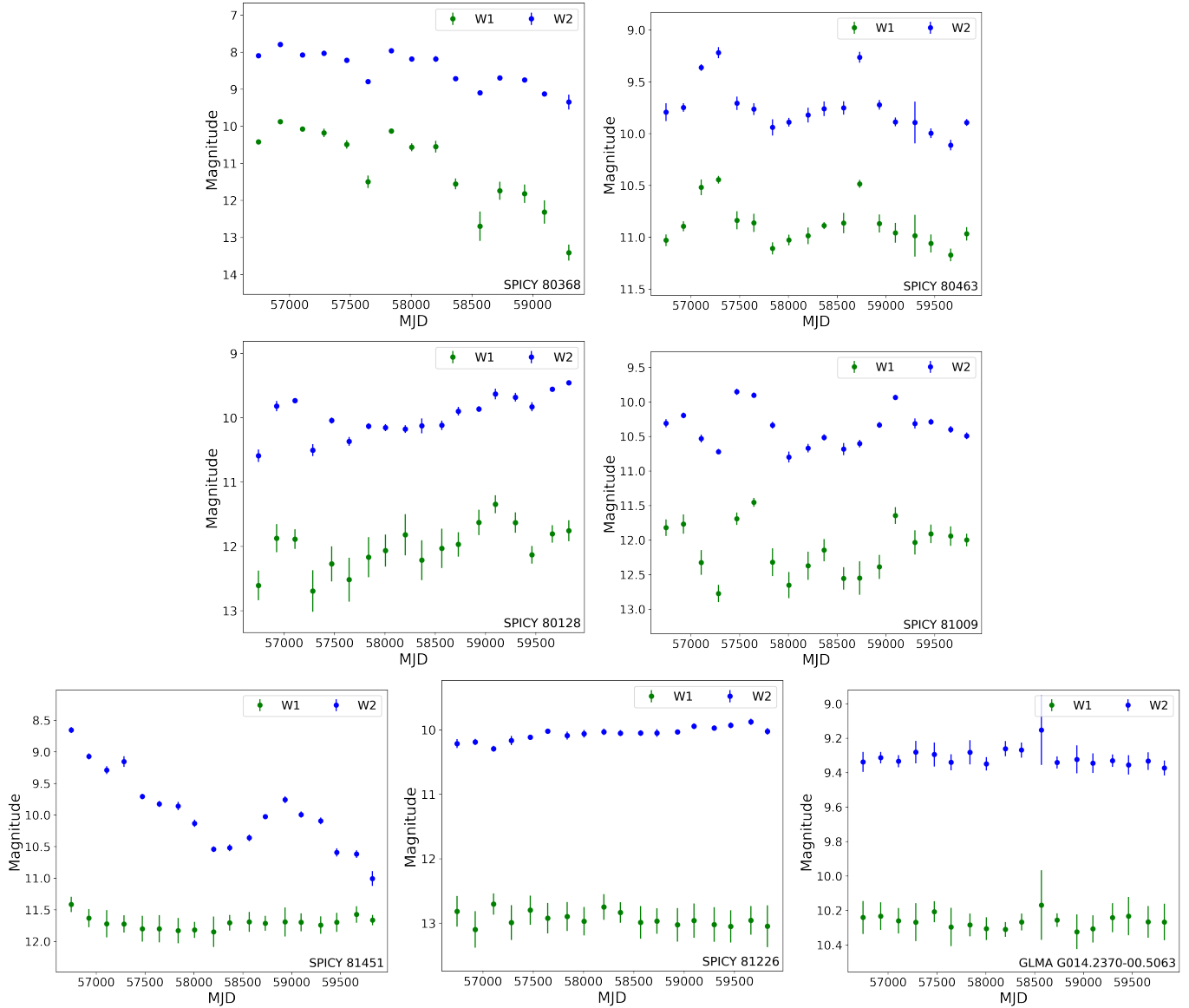


Figure 9. Representative light curves of several sources, observed in both the WISE W1 (green) and W2 (blue) bands. The source identifier is provided in the bottom right corner of each panel.

Four mid-IR variable sources, all determined variable only at W2, have no or very weak correlation according to the Spearman correlation test results, suggesting that the observed flux variation may be specific to only one of the WISE bands. It is important to note, however, that noise levels in the data play a role in confusing the variability at W1 and should be taken into account when interpreting these results. Thus, each of these four variables was considered carefully by eye. Among these four exceptional sources, only SPICY 81451 (Figure 9) reveals a clear difference in variability between the W1 and W2 bands. This finding warrants further investigation to understand the underlying mechanisms respon-

sible for this distinct behavior as discussed in further detail in Section 4.3.2.

4.3.2. The confused case of SPICY 81451 in the mid-IR

SPICY 81451 presents a complex and intriguing case. This source shows dramatic flux fluctuations in the WISE W2 band yet displays no discernible variation in the WISE W1 band (see Figure 9). A high angular resolution UKIDSS K image taken in 2012 (0.7"; Lucas et al. 2008) reveals that there are three sources in proximity to the location of the WISE detection. One of the three UKIDSS sources is classified as a galaxy (UGPS J181932.72-164510.2), a second source is considered stellar (UGPS J181933.04-164510.8), while the faintest source is considered a YSO (UGPS J181932.80-

164511.9). When examining the WISE peak positions, an offset of $2.7''$ is observed between the WISE W1 and W2. Furthermore, comparing against the positions of the UKIDSS sources reveals that the W1 and W2 WISE peaks coincide with a different UKIDSS source. Consequently, the W2 peak likely originates from the known YSO, while the W1 emission is likely associated with the nearby bright star. This suggests that the discrepancy in W1 and W2 flux variability is likely due to the emission in each WISE band being dominated by different sources. Notably, the YSO counterpart disappears in a more recent CFHT Ks image from 2020. This is consistent with the decline observed in WISE W2 and supports the suggestion that the two WISE bands are dominated by emission for a different source.

4.4. Comparison with Variables in Low-mass Star-forming Regions

Our survey of the M17SWex region, which is forming stars of intermediate mass at a distance of ~ 1.8 kpc, complements the Gould Belt investigations by Lee et al. (2021b) and Park et al. (2021), which focus on low-mass star-forming regions within 500 pc. Thus, a comparative analysis can offer valuable insights into the universality and diversity of star-forming processes.

In the sub-mm range, we identified only two robust sub-mm variable candidates out of 146 bright peaks (excluding the one robust variable extragalactic source). This corresponds to a lower detection rate compared to the 18 out of 83 protostars within the Gould Belt found by Lee et al. (2021b) over a similar timescale. It is possible that this difference might be attributable to environmental factors, including an inherent weaker (or rarer) variability for the YSOs in the more massive M17SWex. However, it is also worth recognizing the challenges of detecting sub-mm variability signatures at greater distances, where for a fixed JCMT beam the amount of envelope and nearby cloud contributing to the observed peak flux increases significantly and may therefore smother the localized variations. This latter possibility will be quantitatively explored in a companion JCMT Transient Survey paper by Wang et al. (in preparation).

Our mid-IR analysis of M17SWex used 9 years of WISE monitoring to assess variability, compared to the 6.5 years of mid-IR Gould Belt monitoring employed by Park et al. (2021), who focused exclusively on the W2 band. Considering only our W2 results for Class 0/I and Class II, we find consistency with Park et al. (2021) in the relative numbers of variables by evolutionary class and variability type, with a higher fraction of Class 0/I than Class II being variable and longer secular

timescales for the Class 0/I than Class II. However, the overall fraction of variability at both evolutionary stages is notably lower. This is primarily due to a dearth of irregular variability in M17SWex, which may be harder to discern for this sample since the typical mid-IR source is fainter than in the nearby Gould Belt. Setting aside the irregulars, the consistency in variability types between the Gould Belt and M17SWex suggests a potential universality in the underlying mechanisms driving YSOs variability.

Thus, we have somewhat conflicting variability results at sub-mm and mid-IR between M17SWex and the Gould Belt. However, accounting for expected complications monitoring at larger distances with fixed observing conditions, it is reasonable to assume that the underlying physical conditions responsible for stellar assembly remain similar across these star-forming environments. JCMT Transient Survey investigations of three additional massive star-forming regions will further probe this question.

5. SUMMARY

This study represents the first comprehensive attempt to characterize YSO variability in M17SWex, a region poised for the formation of intermediate-mass stars. Variability across many years, at both sub-mm and mid-IR wavelengths has been investigated.

The sub-mm variability analysis uses 3.5 years of monthly monitoring M17SWex with the JCMT and identifies two robust YSO secular variables and one extragalactic source. Compared against previous sub-mm variability analyses in nearby low-mass star-forming regions within the Gould Belt, we find an order of magnitude decrease in detectable variability within M17SWex. While this is possibly due to intrinsic differences in star formation activity with region complexity, it is most likely that observing inherent sub-mm variability is more difficult for sources at larger distances and in more complex environments.

The mid-IR variability analysis, using 9 years of bi-yearly WISE monitoring, reveals significant variability for 47 YSOs, with a notable fraction exhibiting variability in only one WISE band. The comparison of variability types and the correlation analysis between the W1 and W2 bands suggests that for most YSOs the two light curves are intrinsically similar, with the majority of the differences in variability categorization being due to either complexity in the light curves, beyond the simple models being used to fit, and noise. Only for one source, SPICY 81451, are the two mid-IR light curves distinctly different, a consequence of two bright sources

located within the WISE beam, with one source dominating at each wavelength.

When compared with results from low-mass star-forming regions, our mid-IR results for M17 SWEx suggest that some aspects of YSO variability are universal, including more variability at earlier stages and similar fractions of secular variability across regions. Potential regional differences are seen in the stochastic variability, with M17 SWEx having fewer of these sources. However, this is potentially due to the larger distance to the region and the more crowded environment.

Our study underscores the necessity of long-term, multi-wavelength monitoring campaigns across a variety of star formation environments to unravel the intricate processes governing the early evolution of YSOs.

This work was supported by the National Research Foundation of Korea through grants NRF-2020R1A6A3A01100208 & RS-2023-00242652 (G.P.). This work was partly supported by the Korea Astronomy and Space Science Institute grant funded by the Korea government(MSIT) (Project No. 2022-1-840-05). D.J. is supported by NRC Canada and by an NSERC Discovery Grant. J.-E. Lee is supported by the National Research Foundation of Korea (NRF) grant funded by the Korean government (MSIT) (grant number 2021R1A2C1011718). GJH is supported by the National Key R&D program of China 2022YFA1603102 and by general grant 12173003 from the National Natural Science Foundation of China.

Facilities: JCMT

Software: Astropy (Astropy Collaboration et al. 2013, 2018), TOPCAT (Taylor 2005)

APPENDIX

A. SUB-MM LIGHT CURVES OF VARIABLE CANDIDATES

For completeness, Table A1 presents the locations, peak brightnesses, and variability measures used in this paper for all the sources found by the Fellwalker algorithm.

Table A1. Statistics of All Submillimeter Sources

#	ID	f_m (mJy beam $^{-1}$)	SD (mJy beam $^{-1}$)	SD/SD _{fid}	$ S/\Delta S $
1	JCMTPP_J181854.2–164754	14336.49	216.05	1.00	2.31
2	JCMTPP_J181812.2–164933	5409.12	125.06	1.52	5.92
3	JCMTPP_J181812.9–165727	3181.91	49.62	1.00	1.19
4	JCMTPP_J181811.2–165236	1047.20	19.46	0.92	1.17
5	JCMTPP_J181918.7–164357	915.80	25.16	1.28	0.33
6	JCMTPP_J181748.6–170030	794.43	17.59	0.96	1.25
7	JCMTPP_J181829.2–164454	757.06	15.68	0.87	0.54
8	JCMTPP_J181856.9–164612	738.71	16.18	0.91	1.13
9	JCMTPP_J181808.1–165115	680.12	10.40	0.60	0.24
10	JCMTPP_J181805.1–165824	661.41	20.56	1.20	0.42
11	JCMTPP_J181812.9–164824	631.93	19.13	1.13	2.52
12	JCMTPP_J181839.0–165333	628.00	12.99	0.77	0.04
13	JCMTPP_J181811.4–165142	619.85	18.50	1.10	0.70
14	JCMTPP_J181809.3–165042	605.31	17.35	1.04	0.07
15	JCMTPP_J181805.7–165900	600.68	14.28	0.86	0.51
16	JCMTPP_J181803.7–165500	590.95	22.43	1.35	4.39
17	JCMTPP_J181758.8–170233	578.98	20.56	1.25	1.65
18	JCMTPP_J181757.6–170245	576.10	19.47	1.18	1.57
19	JCMTPP_J181806.8–165800	575.75	18.99	1.15	0.28
20	JCMTPP_J181804.7–165139	524.75	17.25	1.07	1.86
21	JCMTPP_J181933.1–164511	492.88	12.52	0.79	0.15
22	JCMTPP_J181804.1–165218	470.80	17.87	1.14	1.44
23	JCMTPP_J181901.9–164039	466.72	22.08	1.41	1.33
24	JCMTPP_J181831.0–165048	466.38	14.44	0.92	1.68
25	JCMTPP_J181805.1–165348	454.12	16.04	1.03	0.09
26	JCMTPP_J181903.2–163939	434.30	18.78	1.22	1.59

Table A1 *continued*

Table A1 (*continued*)

#	ID	f_m	SD	SD/SD _{fid}	$ S/\Delta S $
		(mJy beam $^{-1}$)	(mJy beam $^{-1}$)		
27	JCMTTP_J181801.8–165357	412.68	14.45	0.94	1.37
28	JCMTTP_J181804.5–165415	377.30	10.65	0.71	1.46
29	JCMTTP_J181814.3–165445	369.85	11.15	0.74	0.34
30	JCMTTP_J181818.7–164642	366.87	13.96	0.93	0.03
31	JCMTTP_J181716.6–165835	359.40	25.56	1.70	2.49
32	JCMTTP_J181921.2–164442	357.00	18.59	1.24	0.12
33	JCMTTP_J181919.5–164448	351.13	19.67	1.32	0.48
34	JCMTTP_J181826.9–165533	346.38	18.07	1.21	1.05
35	JCMTTP_J181814.9–165642	345.70	23.87	1.60	0.03
36	JCMTTP_J181932.9–164544	332.91	17.89	1.20	1.77
37	JCMTTP_J181846.3–165409	331.29	18.76	1.26	2.23
38	JCMTTP_J181825.4–165406	325.41	14.58	0.98	0.45
39	JCMTTP_J181832.5–164900	312.54	14.25	0.97	1.40
40	JCMTTP_J181808.7–165627	302.80	12.68	0.86	1.03
41	JCMTTP_J181824.8–165633	295.20	15.74	1.07	0.47
42	JCMTTP_J181812.9–165512	291.55	13.49	0.92	1.17
43	JCMTTP_J181722.0–165856	285.02	14.78	1.01	0.86
44	JCMTTP_J181715.5–165941	284.57	20.60	1.41	0.39
45	JCMTTP_J181819.3–165600	281.91	14.10	0.96	0.11
46	JCMTTP_J181754.2–165927	281.12	15.21	1.04	0.17
47	JCMTTP_J181837.1–164533	278.89	13.91	0.95	1.54
48	JCMTTP_J181717.2–170114	276.01	33.73	2.31	0.30
49	JCMTTP_J181820.6–170127	271.33	11.34	0.78	0.11
50	JCMTTP_J181914.3–164806	269.61	12.05	0.83	0.85
51	JCMTTP_J181829.4–165303	268.19	10.91	0.75	0.99
52	JCMTTP_J181831.0–165221	264.85	11.04	0.76	0.65
53	JCMTTP_J181720.8–170026	264.68	23.89	1.64	0.04
54	JCMTTP_J181822.3–164345	258.56	15.34	1.06	0.02
55	JCMTTP_J181723.7–165905	255.33	16.81	1.16	1.80
56	JCMTTP_J181842.9–163930	254.82	13.79	0.95	1.16
57	JCMTTP_J181804.7–165939	253.51	14.47	1.00	1.76
58	JCMTTP_J181820.0–164609	252.84	13.66	0.94	0.29
59	JCMTTP_J181735.2–170630	250.46	31.92	2.20	0.60
60	JCMTTP_J181726.6–170032	249.92	16.92	1.17	0.11
61	JCMTTP_J181728.3–170441	249.34	20.71	1.43	0.56
62	JCMTTP_J181851.3–163933	248.03	14.03	0.97	2.15
63	JCMTTP_J181821.4–165654	243.78	13.08	0.90	1.71
64	JCMTTP_J181759.1–164427	242.43	13.92	0.96	0.45
65	JCMTTP_J181817.9–165527	241.18	17.08	1.18	1.17
66	JCMTTP_J181904.2–164027	240.44	16.74	1.16	0.42
67	JCMTTP_J181850.9–165033	240.37	13.18	0.91	0.25
68	JCMTTP_J181913.0–163545	238.85	20.63	1.43	1.07
69	JCMTTP_J181848.8–165100	234.43	14.34	0.99	2.01
70	JCMTTP_J181829.0–165530	233.02	18.93	1.31	2.58
71	JCMTTP_J181727.0–170211	232.54	20.89	1.45	2.80
72	JCMTTP_J181725.6–170214	229.10	34.15	2.37	2.06
73	JCMTTP_J181809.5–165354	228.64	11.65	0.81	0.02
74	JCMTTP_J181859.3–165830	226.29	15.65	1.09	0.01
75	JCMTTP_J181825.8–164915	225.34	14.68	1.02	0.78
76	JCMTTP_J181834.0–165157	224.46	14.10	0.98	0.30
77	JCMTTP_J181820.4–165636	222.47	12.19	0.85	0.66
78	JCMTTP_J181718.5–165847	222.04	17.33	1.20	0.06

Table A1 *continued*

Table A1 (*continued*)

#	ID	f_m	SD	SD/SD _{fid}	$ S/\Delta S $
		(mJy beam $^{-1}$)	(mJy beam $^{-1}$)		
79	JCMTTP_J181735.0–170515	219.85	18.60	1.29	0.88
80	JCMTTP_J181810.2–164800	218.06	13.82	0.96	0.73
81	JCMTTP_J181816.2–164957	207.77	15.95	1.11	0.42
82	JCMTTP_J181801.4–165742	207.02	15.74	1.10	0.16
83	JCMTTP_J181727.5–165826	205.94	13.13	0.92	0.43
84	JCMTTP_J181816.4–164733	198.46	15.39	1.08	1.00
85	JCMTTP_J181739.6–170457	197.74	17.24	1.20	1.34
86	JCMTTP_J181822.9–165612	197.14	10.63	0.74	1.28
87	JCMTTP_J181859.9–164109	196.26	18.08	1.26	0.16
88	JCMTTP_J181817.5–164445	195.95	11.54	0.81	0.12
89	JCMTTP_J181815.4–165048	195.03	11.87	0.83	0.83
90	JCMTTP_J181810.6–165442	193.35	14.70	1.03	1.81
91	JCMTTP_J181757.2–170321	190.74	12.59	0.88	1.78
92	JCMTTP_J181832.7–164200	182.45	12.88	0.90	0.03
93	JCMTTP_J181731.2–170138	181.47	26.81	1.88	0.92
94	JCMTTP_J181901.5–163921	180.44	16.67	1.17	1.82
95	JCMTTP_J181828.7–164927	180.41	12.68	0.89	0.96
96	JCMTTP_J181854.0–165133	176.85	11.85	0.83	0.80
97	JCMTTP_J181811.4–165330	174.69	11.95	0.84	0.42
98	JCMTTP_J181811.4–164703	173.57	12.93	0.91	0.36
99	JCMTTP_J181727.3–164902	172.22	15.37	1.08	1.09
100	JCMTTP_J181830.6–164924	171.05	10.24	0.72	1.66
101	JCMTTP_J181902.2–165800	169.15	13.61	0.96	1.09
102	JCMTTP_J181828.3–164533	166.09	12.29	0.86	1.05
103	JCMTTP_J181929.1–164644	164.07	15.77	1.11	1.10
104	JCMTTP_J181759.7–165657	159.33	13.98	0.98	1.75
105	JCMTTP_J181741.1–165118	156.29	16.43	1.16	1.82
106	JCMTTP_J181807.9–164921	156.15	14.83	1.04	1.05
107	JCMTTP_J181832.5–164948	155.63	17.26	1.22	1.10
108	JCMTTP_J181802.8–170545	153.59	58.34	4.11	1.40
109	JCMTTP_J181906.8–164918	151.37	12.87	0.91	0.67
110	JCMTTP_J181812.0–164615	149.31	15.90	1.12	0.01
111	JCMTTP_J181820.6–164533	148.82	11.60	0.82	0.30
112	JCMTTP_J181842.1–165039	145.34	9.98	0.70	1.20
113	JCMTTP_J181820.4–163942	144.18	15.76	1.11	1.39
114	JCMTTP_J181834.8–165121	142.54	13.60	0.96	0.41
115	JCMTTP_J181718.9–165947	141.19	17.37	1.23	0.09
116	JCMTTP_J181828.3–164830	140.76	13.42	0.95	1.29
117	JCMTTP_J181911.8–164809	138.59	14.80	1.05	2.19
118	JCMTTP_J181725.0–164744	137.54	12.97	0.92	0.15
119	JCMTTP_J181852.1–164406	137.53	16.57	1.17	1.58
120	JCMTTP_J181903.8–164142	134.32	17.36	1.23	0.22
121	JCMTTP_J181852.8–164315	133.66	13.00	0.92	0.18
122	JCMTTP_J181919.1–165009	128.96	13.16	0.93	0.52
123	JCMTTP_J181820.4–164421	124.89	10.03	0.71	0.43
124	JCMTTP_J181820.4–164736	122.65	14.82	1.05	0.26
125	JCMTTP_J181824.1–165439	122.61	12.05	0.85	2.05
126	JCMTTP_J181839.2–165639	122.40	14.80	1.05	0.29
127	JCMTTP_J181907.0–164945	119.73	15.12	1.07	0.70
128	JCMTTP_J181737.5–165345	118.80	13.79	0.98	1.38
129	JCMTTP_J181818.9–164954	118.52	14.69	1.04	0.05
130	JCMTTP_J181847.6–165718	118.41	13.97	0.99	0.40

Table A1 *continued*

Table A1 (*continued*)

#	ID	f_m	SD	SD/SD _{fid}	$ S/\Delta S $
		(mJy beam $^{-1}$)	(mJy beam $^{-1}$)		
131	JCMTTP_J181825.6–165100	118.17	13.53	0.96	0.49
132	JCMTTP_J181800.9–165606	117.15	11.96	0.85	1.58
133	JCMTTP_J181724.6–164944	115.05	17.62	1.25	0.06
134	JCMTTP_J181850.9–163909	114.84	18.17	1.29	0.82
135	JCMTTP_J181758.0–165709	114.84	11.29	0.80	1.76
136	JCMTTP_J181857.2–165124	114.76	10.14	0.72	0.41
137	JCMTTP_J181738.1–170227	112.83	15.74	1.12	1.10
138	JCMTTP_J181744.3–164415	110.80	14.06	1.00	0.38
139	JCMTTP_J181907.4–163703	110.24	16.32	1.16	0.56
140	JCMTTP_J181850.7–164421	109.66	12.33	0.87	0.18
141	JCMTTP_J181718.5–170059	108.94	21.95	1.56	1.36
142	JCMTTP_J181854.6–164239	108.68	13.85	0.98	0.50
143	JCMTTP_J181735.0–170545	108.57	22.32	1.58	0.42
144	JCMTTP_J181743.8–170533	107.73	19.40	1.38	0.28
145	JCMTTP_J181801.6–170136	103.73	10.62	0.75	0.60
146	JCMTTP_J181904.9–164103	103.46	13.71	0.97	1.77
147	JCMTTP_J181827.5–164333	101.93	13.14	0.93	0.57
148	JCMTTP_J181908.4–164906	101.45	13.06	0.93	0.95
149	JCMTTP_J181818.1–165212	100.74	8.74	0.62	1.22
150	JCMTTP_J181828.5–170439	100.34	15.51	1.10	0.07
151	JCMTPP_J181912.4–163503	99.79	20.62	1.46	0.67
152	JCMTPP_J181748.0–164245	99.02	10.92	0.78	0.97
153	JCMTPP_J181737.3–165515	98.52	11.76	0.84	0.20
154	JCMTPP_J181914.7–164957	96.44	13.76	0.98	0.08
155	JCMTPP_J181915.7–163527	95.92	22.19	1.58	2.44
156	JCMTPP_J181733.3–170309	95.07	14.21	1.01	1.38
157	JCMTPP_J181758.4–165627	94.98	13.78	0.98	0.94
158	JCMTPP_J181713.4–164438	94.81	20.74	1.47	0.55
159	JCMTPP_J181746.9–165657	92.72	10.77	0.77	1.72
160	JCMTPP_J181732.7–165109	92.24	13.41	0.95	0.79
161	JCMTPP_J181834.0–165239	91.06	12.22	0.87	1.15
162	JCMTPP_J181919.9–165106	90.12	16.00	1.14	3.99
163	JCMTPP_J181817.7–170012	86.15	12.71	0.90	1.42
164	JCMTPP_J181904.4–163900	85.73	10.41	0.74	0.03
165	JCMTPP_J181717.0–165702	85.65	15.04	1.07	0.12
166	JCMTPP_J181907.2–164848	85.48	9.67	0.69	0.82
167	JCMTPP_J181844.0–164512	84.95	12.29	0.87	0.91
168	JCMTPP_J181915.5–164854	84.71	11.49	0.82	0.42
169	JCMTPP_J181821.6–164218	84.09	11.48	0.82	0.46
170	JCMTPP_J181909.4–163709	83.48	14.67	1.04	0.68
171	JCMTPP_J181856.1–164112	83.13	12.88	0.92	2.82
172	JCMTPP_J181905.1–163709	81.11	14.74	1.05	1.28
173	JCMTPP_J181719.3–165720	80.84	12.28	0.87	1.16
174	JCMTPP_J181914.2–163439	80.72	28.08	2.00	0.69
175	JCMTPP_J181814.6–164006	79.92	10.14	0.72	0.61
176	JCMTPP_J181758.4–170636	79.21	14.13	1.01	0.12
177	JCMTPP_J181854.3–170357	78.37	10.78	0.77	1.23
178	JCMTPP_J181938.1–164535	78.32	15.91	1.13	1.57
179	JCMTPP_J181723.5–170256	77.59	24.08	1.71	2.23
180	JCMTPP_J181854.8–164036	77.56	14.63	1.04	0.79
181	JCMTPP_J181916.0–165115	77.42	11.67	0.83	0.02
182	JCMTPP_J181752.8–165754	77.37	13.20	0.94	1.09

Table A1 *continued*

Table A1 (*continued*)

#	ID	f_m	SD	SD/SD _{fid}	$ S/\Delta S $
		(mJy beam $^{-1}$)	(mJy beam $^{-1}$)		
183	JCMTTP_J181733.4–164639	77.26	13.12	0.93	0.01
184	JCMTTP_J181858.8–164154	77.07	9.41	0.67	1.28
185	JCMTTP_J181916.0–164830	77.06	13.71	0.98	0.21
186	JCMTTP_J181757.4–165927	75.69	10.51	0.75	1.11
187	JCMTTP_J181715.4–164702	75.51	20.22	1.44	1.79
188	JCMTTP_J181901.6–164933	75.35	14.03	1.00	0.11
189	JCMTTP_J181910.1–165036	74.77	12.70	0.90	1.43
190	JCMTTP_J181716.4–165520	74.60	13.94	0.99	0.57
191	JCMTTP_J181821.8–170448	74.25	13.59	0.97	0.04
192	JCMTTP_J181901.1–164715	73.32	11.83	0.84	0.20
193	JCMTTP_J181825.2–164830	73.09	10.48	0.75	0.65
194	JCMTTP_J181840.7–164736	73.00	15.40	1.10	0.41
195	JCMTTP_J181850.3–165954	72.75	13.86	0.99	0.37
196	JCMTTP_J181818.5–165145	72.65	12.88	0.92	1.09
197	JCMTTP_J181837.9–163636	72.61	15.03	1.07	0.06
198	JCMTTP_J181841.7–164245	72.61	11.45	0.82	0.84
199	JCMTTP_J181844.4–163727	72.46	9.99	0.71	0.93
200	JCMTTP_J181811.4–171051	71.85	25.11	1.79	0.35
201	JCMTTP_J181745.0–165909	71.72	13.66	0.97	0.31
202	JCMTTP_J181859.0–163857	71.60	9.74	0.69	0.24
203	JCMTTP_J181944.2–164917	71.54	12.90	0.92	0.61
204	JCMTTP_J181807.0–165400	71.31	14.41	1.03	0.01
205	JCMTTP_J181929.5–164753	70.54	10.93	0.78	0.50
206	JCMTTP_J181733.1–170006	70.32	16.49	1.17	0.33
207	JCMTTP_J181725.8–170320	69.98	22.36	1.59	0.69
208	JCMTTP_J181839.4–164842	69.74	11.67	0.83	1.35
209	JCMTTP_J181722.7–164950	69.20	15.71	1.12	0.33
210	JCMTTP_J181919.9–164745	68.89	9.66	0.69	2.63
211	JCMTTP_J181819.1–165448	68.75	14.52	1.03	1.48
212	JCMTTP_J181925.5–164321	68.72	15.13	1.08	0.55
213	JCMTTP_J181844.7–171021	68.28	19.25	1.37	0.07
214	JCMTTP_J181726.7–164729	67.43	14.79	1.05	1.44
215	JCMTTP_J181751.9–170133	67.37	9.26	0.66	0.55
216	JCMTTP_J181925.6–165157	66.10	11.31	0.81	2.85
217	JCMTTP_J181736.3–165212	64.49	14.45	1.03	1.28
218	JCMTTP_J181758.2–165606	64.10	12.73	0.91	1.72
219	JCMTTP_J181818.3–165833	63.23	9.54	0.68	0.63
220	JCMTTP_J181823.7–165245	62.95	10.90	0.78	2.43
221	JCMTTP_J181844.4–164724	62.64	10.03	0.71	0.56
222	JCMTTP_J181758.5–163321	62.12	22.91	1.63	1.34
223	JCMTTP_J181928.7–164429	62.08	13.65	0.97	0.68
224	JCMTTP_J181735.7–165251	61.57	11.55	0.82	1.88
225	JCMTTP_J181733.8–165533	60.75	12.62	0.90	1.28
226	JCMTTP_J181924.5–164648	60.63	9.32	0.66	0.83
227	JCMTTP_J181901.1–165003	60.56	9.87	0.70	1.26
228	JCMTTP_J181838.2–165148	60.44	12.04	0.86	1.28
229	JCMTTP_J181821.4–165051	59.46	10.67	0.76	1.03
230	JCMTTP_J181814.5–164548	59.23	11.82	0.84	0.22
231	JCMTTP_J181718.5–170144	58.51	22.64	1.61	0.31
232	JCMTTP_J181902.2–165045	58.42	13.62	0.97	0.38
233	JCMTTP_J181827.7–165112	58.12	14.56	1.04	0.89
234	JCMTTP_J181846.9–165448	58.10	13.21	0.94	0.23

Table A1 *continued*

Table A1 (*continued*)

#	ID	f_m	SD	SD/SD _{fid}	$ S/\Delta S $
		(mJy beam $^{-1}$)	(mJy beam $^{-1}$)		
235	JCMTTP_J181826.2–164545	57.94	13.18	0.94	2.52
236	JCMTTP_J181832.9–164312	57.54	14.53	1.04	0.01
237	JCMTTP_J181924.5–164533	57.47	12.54	0.89	1.05
238	JCMTTP_J181854.3–165621	57.16	6.82	0.49	1.26
239	JCMTTP_J181737.9–165657	57.08	11.87	0.85	1.26
240	JCMTTP_J181902.2–165421	56.82	11.64	0.83	1.49
241	JCMTTP_J181732.7–170338	56.42	16.85	1.20	0.36
242	JCMTTP_J181929.5–164359	56.34	15.13	1.08	0.36
243	JCMTTP_J181731.7–165917	56.22	11.54	0.82	0.56
244	JCMTTP_J181721.1–164917	55.52	13.22	0.94	1.07
245	JCMTTP_J181921.4–165718	54.97	10.50	0.75	0.24
246	JCMTTP_J181824.1–165848	54.89	12.79	0.91	0.56
247	JCMTTP_J181853.6–165712	54.30	14.34	1.02	0.53
248	JCMTTP_J181850.5–164500	53.97	11.94	0.85	0.79
249	JCMTTP_J181844.0–165306	53.86	12.24	0.87	0.30
250	JCMTTP_J181736.3–165751	53.40	14.22	1.01	1.41
251	JCMTTP_J181920.8–164821	53.25	13.00	0.93	0.39
252	JCMTTP_J181923.7–164924	53.25	13.59	0.97	1.12
253	JCMTTP_J181922.7–165057	53.17	14.04	1.00	0.57
254	JCMTTP_J181832.9–171012	52.31	20.16	1.44	0.81
255	JCMTTP_J181739.7–164506	52.19	9.86	0.70	1.05
256	JCMTTP_J181804.7–165609	52.17	9.34	0.67	0.57
257	JCMTTP_J181938.7–164332	52.08	19.31	1.38	0.09
258	JCMTTP_J181755.5–164454	51.90	8.60	0.61	1.17
259	JCMTTP_J181717.0–165402	51.54	14.29	1.02	0.39
260	JCMTTP_J181825.4–170430	51.42	12.25	0.87	1.02
261	JCMTTP_J181826.9–164633	51.40	11.65	0.83	0.60
262	JCMTTP_J181734.6–165842	51.30	16.16	1.15	0.27
263	JCMTTP_J181757.2–165109	51.21	14.14	1.01	1.34
264	JCMTTP_J181828.7–165018	51.06	16.61	1.18	0.16
265	JCMTTP_J181911.8–165006	50.68	10.46	0.75	0.98
266	JCMTTP_J181831.9–170503	50.41	7.86	0.56	0.62
267	JCMTTP_J181834.8–170933	50.03	16.82	1.20	0.13
268	JCMTTP_J181822.3–165006	49.99	12.36	0.88	0.22
269	JCMTTP_J181822.1–164039	49.40	12.03	0.86	0.93
270	JCMTTP_J181710.8–164626	49.28	20.41	1.46	0.52
271	JCMTTP_J181819.8–165927	48.87	11.74	0.84	1.38
272	JCMTTP_J181744.4–170100	48.30	9.15	0.65	2.11
273	JCMTTP_J181907.1–163612	48.30	16.76	1.20	0.37
274	JCMTTP_J181908.5–165318	48.27	12.70	0.91	2.16
275	JCMTTP_J181806.2–170312	48.19	12.84	0.92	1.05
276	JCMTTP_J181826.7–165200	47.99	10.61	0.76	1.41
277	JCMTTP_J181819.1–170230	47.95	11.95	0.85	1.08
278	JCMTTP_J181840.6–163827	47.67	12.83	0.92	1.93
279	JCMTTP_J181849.0–165836	47.29	9.08	0.65	0.88
280	JCMTTP_J181836.5–164921	47.14	9.19	0.66	0.05
281	JCMTTP_J181818.9–170409	47.04	14.07	1.00	0.37
282	JCMTTP_J181832.7–170100	46.77	11.62	0.83	0.35
283	JCMTTP_J181847.5–164457	46.54	9.81	0.70	1.28
284	JCMTTP_J181844.4–165818	46.22	7.13	0.51	0.52
285	JCMTTP_J181947.7–164423	46.02	27.54	1.96	1.35
286	JCMTTP_J181928.8–165753	45.99	16.11	1.15	1.78

Table A1 *continued*

Table A1 (*continued*)

#	ID	f_m	SD	SD/SD _{fid}	$ S/\Delta S $
		(mJy beam $^{-1}$)	(mJy beam $^{-1}$)		
287	JCMTTP_J181728.4–164820	45.64	10.93	0.78	0.51
288	JCMTTP_J181855.7–165003	45.49	12.78	0.91	0.96
289	JCMTTP_J181921.6–163836	45.44	17.74	1.27	0.49
290	JCMTTP_J181932.9–165853	45.41	19.49	1.39	0.28
291	JCMTTP_J181803.2–170821	45.20	13.96	1.00	1.00
292	JCMTTP_J181803.0–165618	45.17	13.60	0.97	1.79
293	JCMTTP_J181727.6–164435	45.07	13.11	0.94	1.83
294	JCMTTP_J181750.6–163406	44.78	22.69	1.62	0.15
295	JCMTTP_J181823.9–164154	44.68	14.56	1.04	0.12
296	JCMTTP_J181838.8–164815	44.03	13.16	0.94	1.67
297	JCMTTP_J181913.8–163721	43.90	9.36	0.67	2.11
298	JCMTTP_J181817.4–170836	43.78	15.47	1.10	0.84
299	JCMTTP_J181854.2–164151	43.75	11.66	0.83	1.57
300	JCMTTP_J181726.6–165859	43.63	16.58	1.18	1.29
301	JCMTTP_J181940.8–164841	43.33	20.16	1.44	0.23
302	JCMTTP_J181739.6–165903	42.88	17.30	1.23	0.37
303	JCMTTP_J181744.4–165415	42.85	13.16	0.94	0.89
304	JCMTTP_J181743.8–165612	41.93	12.28	0.88	0.68
305	JCMTTP_J181837.9–165527	41.56	7.09	0.51	0.84
306	JCMTTP_J181906.1–164327	41.54	13.07	0.93	0.29
307	JCMTTP_J181906.8–165242	41.32	12.72	0.91	3.16
308	JCMTTP_J181800.1–164721	41.21	15.88	1.13	0.78
309	JCMTTP_J181737.2–164206	41.14	12.82	0.92	0.34
310	JCMTTP_J181846.3–164121	40.88	9.11	0.65	1.87
311	JCMTTP_J181831.7–163233	40.75	16.45	1.17	0.86
312	JCMTTP_J181825.4–165027	40.43	9.16	0.65	0.55
313	JCMTTP_J181719.2–164535	40.31	19.88	1.42	0.78
314	JCMTTP_J181728.6–165138	40.30	10.84	0.77	0.17
315	JCMTTP_J181808.7–163921	40.05	10.50	0.75	1.51
316	JCMTTP_J181756.1–165757	39.92	16.93	1.21	1.79
317	JCMTTP_J181755.1–165251	39.92	11.40	0.81	1.88
318	JCMTTP_J181757.1–170939	39.91	21.95	1.57	0.11
319	JCMTTP_J181830.4–164745	39.84	13.72	0.98	1.20
320	JCMTTP_J181813.7–165921	39.67	12.26	0.87	0.56
321	JCMTTP_J181929.3–165108	39.34	10.08	0.72	1.13
322	JCMTTP_J181822.7–165936	39.01	10.65	0.76	1.26
323	JCMTTP_J181742.4–164227	38.94	18.39	1.31	0.57
324	JCMTTP_J181830.6–165827	38.91	15.64	1.12	0.01
325	JCMTTP_J181732.1–165653	38.90	11.90	0.85	0.90
326	JCMTTP_J181827.3–164145	38.67	13.43	0.96	0.37
327	JCMTTP_J181901.7–164327	38.23	11.09	0.79	0.97
328	JCMTTP_J181855.3–165224	38.12	10.37	0.74	1.61
329	JCMTTP_J181832.9–170742	38.10	12.25	0.87	2.17
330	JCMTTP_J181723.3–165753	37.98	12.82	0.92	0.56
331	JCMTTP_J181919.3–165754	37.88	9.96	0.71	1.20
332	JCMTTP_J181737.9–170148	37.87	12.51	0.89	2.27
333	JCMTTP_J181803.7–164533	37.47	12.03	0.86	0.72
334	JCMTTP_J181846.5–164030	37.42	12.29	0.88	0.28
335	JCMTTP_J181842.7–164318	37.15	14.00	1.00	0.45
336	JCMTTP_J181752.6–165627	37.03	9.93	0.71	0.77
337	JCMTTP_J181723.8–164417	37.02	12.57	0.90	0.98
338	JCMTTP_J181829.2–164239	36.97	13.30	0.95	1.30

Table A1 *continued*

Table A1 (*continued*)

#	ID	f_m	SD	SD/SD _{fid}	$ S/\Delta S $
		(mJy beam $^{-1}$)	(mJy beam $^{-1}$)		
339	JCMTTP_J181938.9–164241	36.81	19.95	1.42	1.01
340	JCMTTP_J181852.6–165224	36.66	13.27	0.95	0.52
341	JCMTTP_J181827.7–170157	36.55	12.63	0.90	0.61
342	JCMTTP_J181906.8–164445	36.52	11.46	0.82	0.03
343	JCMTTP_J181858.0–163824	36.22	12.30	0.88	2.04
344	JCMTTP_J181918.3–165239	36.22	12.96	0.92	0.61
345	JCMTTP_J181925.8–170054	36.15	16.10	1.15	1.49
346	JCMTTP_J181847.4–170012	36.00	12.00	0.86	1.78
347	JCMTTP_J181836.5–164803	35.88	10.05	0.72	0.76
348	JCMTTP_J181908.5–165154	35.60	8.75	0.62	0.30
349	JCMTTP_J181807.2–170230	35.47	9.69	0.69	1.82
350	JCMTTP_J181718.4–164338	34.44	20.28	1.45	0.35
351	JCMTTP_J181722.1–165520	34.16	15.08	1.08	1.68
352	JCMTTP_J181754.2–170824	33.93	18.54	1.32	0.84
353	JCMTTP_J181853.4–170518	33.73	14.08	1.01	0.97
354	JCMTTP_J181908.5–165645	33.69	12.39	0.88	0.82
355	JCMTTP_J181755.6–164057	33.68	13.00	0.93	0.90
356	JCMTTP_J181804.9–171003	33.68	18.34	1.31	2.11
357	JCMTTP_J181926.2–165124	33.67	10.70	0.76	2.33
358	JCMTTP_J181808.9–163351	33.48	21.35	1.52	0.05
359	JCMTTP_J181757.0–165354	33.30	11.89	0.85	1.78
360	JCMTTP_J181855.1–165445	33.18	13.37	0.95	0.79
361	JCMTTP_J181824.3–170730	33.03	16.50	1.18	0.16
362	JCMTTP_J181912.4–165700	33.03	10.57	0.75	1.04
363	JCMTTP_J181924.9–164136	33.01	17.04	1.22	0.03
364	JCMTTP_J181830.4–164121	32.95	9.15	0.65	1.84
365	JCMTTP_J181923.1–170142	32.82	12.43	0.89	0.38
366	JCMTTP_J181926.5–165918	32.70	16.38	1.17	2.03
367	JCMTTP_J181918.3–165442	32.66	15.03	1.07	0.67
368	JCMTTP_J181944.1–164408	32.62	26.12	1.86	0.31
369	JCMTTP_J181752.3–170430	32.43	12.85	0.92	1.01
370	JCMTTP_J181933.5–164214	32.23	18.20	1.30	0.57
371	JCMTTP_J181717.9–165302	32.02	16.59	1.18	0.47
372	JCMTTP_J181856.3–163657	32.01	14.67	1.05	1.07
373	JCMTTP_J181848.2–163545	31.92	14.03	1.00	0.48
374	JCMTTP_J181923.5–165545	31.44	14.82	1.06	0.54
375	JCMTTP_J181814.1–164312	31.35	10.57	0.75	1.14
376	JCMTTP_J181734.5–163912	31.32	16.57	1.18	0.42
377	JCMTTP_J181709.7–165302	31.32	24.22	1.73	0.70
378	JCMTTP_J181721.9–164135	31.29	20.72	1.48	0.59
379	JCMTTP_J181836.9–163200	31.28	19.43	1.39	0.08
380	JCMTTP_J181737.9–170012	31.22	11.47	0.82	0.93
381	JCMTTP_J181755.1–164733	31.20	12.83	0.92	0.37
382	JCMTTP_J181842.5–165406	31.08	11.04	0.79	0.24
383	JCMTTP_J181922.8–164054	30.96	19.94	1.42	0.93
384	JCMTTP_J181920.0–170712	30.93	30.41	2.17	2.23
385	JCMTTP_J181746.9–170339	30.91	14.96	1.07	1.15
386	JCMTTP_J181817.9–165357	30.86	13.23	0.94	1.30
387	JCMTTP_J181909.2–163903	30.65	11.96	0.85	0.56
388	JCMTTP_J181836.7–170309	30.61	11.06	0.79	1.30
389	JCMTTP_J181834.4–165721	30.58	9.20	0.66	0.61
390	JCMTTP_J181820.8–170730	30.48	12.60	0.90	0.62

Table A1 *continued*

Table A1 (*continued*)

#	ID	f_m	SD	SD/SD _{fid}	$ S/\Delta S $
		(mJy beam $^{-1}$)	(mJy beam $^{-1}$)		
391	JCMTPP_J181832.5–165554	30.04	8.40	0.60	2.32
392	JCMTPP_J181838.4–164145	30.02	14.43	1.03	2.15
393	JCMTPP_J181817.7–164057	29.88	10.23	0.73	1.42
394	JCMTPP_J181801.8–164645	29.71	8.44	0.60	0.76
395	JCMTPP_J181725.4–165147	29.58	10.83	0.77	0.36
396	JCMTPP_J181746.9–165524	29.37	13.91	0.99	0.75
397	JCMTPP_J181901.3–163351	29.36	18.82	1.34	2.23
398	JCMTPP_J181937.2–164247	29.32	24.66	1.76	0.21
399	JCMTPP_J181857.1–163239	29.32	21.85	1.56	2.06
400	JCMTPP_J181948.3–164532	29.32	28.33	2.02	0.23
401	JCMTPP_J181830.2–165603	29.19	12.60	0.90	0.93
402	JCMTPP_J181838.8–170000	29.07	13.29	0.95	0.09
403	JCMTPP_J181802.0–170500	28.84	12.02	0.86	0.51
404	JCMTPP_J181913.7–170042	28.78	12.49	0.89	0.35
405	JCMTPP_J181849.0–165230	28.61	13.32	0.95	3.44
406	JCMTPP_J181830.0–165912	28.55	10.71	0.76	0.99
407	JCMTPP_J181808.7–164254	28.22	10.02	0.72	1.44
408	JCMTPP_J181747.1–170733	28.21	18.20	1.30	0.20
409	JCMTPP_J181711.0–165526	28.13	20.23	1.44	0.61
410	JCMTPP_J181753.6–170721	28.08	19.03	1.36	1.16
411	JCMTPP_J181735.3–164412	28.01	16.26	1.16	1.54
412	JCMTPP_J181812.6–170445	28.00	8.21	0.59	0.04
413	JCMTPP_J181737.8–164533	27.98	10.38	0.74	1.05
414	JCMTPP_J181813.1–164212	27.98	12.23	0.87	0.20
415	JCMTPP_J181819.7–170642	27.91	10.66	0.76	0.75
416	JCMTPP_J181907.2–163803	27.89	14.72	1.05	1.32
417	JCMTPP_J181907.1–163454	27.89	21.70	1.55	1.05
418	JCMTPP_J181754.5–164339	27.87	10.99	0.78	0.27
419	JCMTPP_J181803.5–163730	27.87	10.75	0.77	1.06
420	JCMTPP_J181736.8–163648	27.83	21.52	1.54	0.27
421	JCMTPP_J181902.6–164515	27.81	14.27	1.02	0.29
422	JCMTPP_J181745.7–164039	27.66	13.55	0.97	1.46
423	JCMTPP_J181817.5–163445	27.62	14.05	1.00	1.96
424	JCMTPP_J181925.8–165306	27.62	13.97	1.00	1.17
425	JCMTPP_J181750.9–164603	27.47	9.80	0.70	2.04
426	JCMTPP_J181852.0–165836	27.33	16.43	1.17	2.16
427	JCMTPP_J181838.3–163339	27.29	27.07	1.93	0.69
428	JCMTPP_J181948.1–164744	27.23	21.28	1.52	0.59
429	JCMTPP_J181744.4–165206	27.14	11.21	0.80	0.70
430	JCMTPP_J181831.3–165351	27.11	10.99	0.78	1.07
431	JCMTPP_J181822.1–165754	27.03	13.98	1.00	0.51
432	JCMTPP_J181810.2–163245	26.99	23.84	1.70	1.53
433	JCMTPP_J181829.4–164000	26.80	11.75	0.84	2.23
434	JCMTPP_J181815.6–163236	26.67	23.18	1.66	3.07
435	JCMTPP_J181825.6–165954	26.65	16.48	1.18	0.50
436	JCMTPP_J181759.7–170818	26.52	19.03	1.36	0.76
437	JCMTPP_J181813.1–163848	26.46	11.61	0.83	2.52
438	JCMTPP_J181850.5–163703	26.36	16.31	1.16	1.68
439	JCMTPP_J181812.6–170118	26.21	10.45	0.75	1.18
440	JCMTPP_J181802.6–170348	26.06	13.09	0.93	0.18
441	JCMTPP_J181917.2–164006	25.99	12.93	0.92	1.50
442	JCMTPP_J181901.8–165557	25.89	10.99	0.78	0.12

Table A1 *continued*

Table A1 (*continued*)

#	ID	f_m	SD	SD/SD _{fid}	$ S/\Delta S $
		(mJy beam $^{-1}$)	(mJy beam $^{-1}$)		
443	JCMTTP_J181801.6–164348	25.85	13.44	0.96	0.11
444	JCMTTP_J181834.6–164703	25.78	12.46	0.89	0.45
445	JCMTTP_J181730.4–165520	25.72	12.87	0.92	1.44
446	JCMTTP_J181914.5–165445	25.58	16.53	1.18	3.10
447	JCMTTP_J181845.9–170306	25.42	9.07	0.65	1.48
448	JCMTTP_J181859.8–163551	25.18	17.46	1.25	1.46
449	JCMTTP_J181909.1–165536	25.06	8.73	0.62	1.23
450	JCMTTP_J181743.8–164748	25.00	12.35	0.88	0.12
451	JCMTTP_J181743.2–165257	24.98	10.41	0.74	2.49
452	JCMTTP_J181727.6–164023	24.94	17.40	1.24	1.53
453	JCMTTP_J181842.5–170021	24.82	12.21	0.87	2.08
454	JCMTTP_J181908.2–163733	24.71	14.39	1.03	1.54
455	JCMTTP_J181820.6–170606	24.64	14.90	1.06	0.28
456	JCMTTP_J181814.7–171015	24.41	19.43	1.39	0.06
457	JCMTTP_J181747.4–165006	24.39	12.45	0.89	1.29
458	JCMTTP_J181835.6–163924	24.32	10.40	0.74	0.91
459	JCMTTP_J181752.8–163915	24.31	14.83	1.06	0.99
460	JCMTTP_J181802.2–163427	24.24	29.07	2.08	1.11
461	JCMTTP_J181831.0–163824	24.22	13.86	0.99	0.29
462	JCMTTP_J181854.5–165806	24.20	14.49	1.03	0.47
463	JCMTTP_J181732.8–163951	23.98	12.43	0.89	1.54
464	JCMTTP_J181900.1–163654	23.91	17.57	1.25	0.31
465	JCMTTP_J181823.7–170039	23.90	8.81	0.63	0.97
466	JCMTTP_J181747.1–165809	23.87	13.99	1.00	0.92
467	JCMTTP_J181816.0–170618	23.78	15.06	1.08	0.08
468	JCMTTP_J181828.7–171118	23.78	30.26	2.16	1.42
469	JCMTTP_J181811.8–164403	23.71	12.04	0.86	0.17
470	JCMTTP_J181935.8–164138	23.66	19.69	1.41	1.96
471	JCMTTP_J181844.0–163339	23.65	24.58	1.76	1.39
472	JCMTTP_J181817.1–163218	23.62	29.02	2.07	2.69
473	JCMTTP_J181755.8–163924	23.36	13.34	0.95	0.84
474	JCMTTP_J181811.6–170848	23.35	13.77	0.98	0.74
475	JCMTTP_J181806.8–170609	23.26	12.61	0.90	1.13
476	JCMTTP_J181929.6–165011	23.25	16.24	1.16	0.32
477	JCMTTP_J181728.0–164211	23.18	13.96	1.00	1.73
478	JCMTTP_J181711.4–165802	22.97	20.06	1.43	2.05
479	JCMTTP_J181843.6–163603	22.96	13.14	0.94	0.98
480	JCMTTP_J181751.5–170527	22.88	17.01	1.21	0.18
481	JCMTTP_J181725.2–164641	22.86	11.56	0.83	0.39
482	JCMTTP_J181911.6–165824	22.86	12.69	0.91	2.59
483	JCMTTP_J181909.3–164557	22.79	8.82	0.63	0.85
484	JCMTTP_J181934.4–164850	22.79	14.50	1.04	1.05
485	JCMTTP_J181808.7–170854	22.71	12.87	0.92	2.13
486	JCMTTP_J181940.4–164702	22.50	18.83	1.34	0.37
487	JCMTTP_J181828.3–170724	22.48	11.47	0.82	0.45
488	JCMTTP_J181736.8–163712	22.48	16.54	1.18	2.21
489	JCMTTP_J181743.6–170357	22.44	15.01	1.07	1.20
490	JCMTTP_J181837.3–164339	22.40	6.64	0.47	0.24
491	JCMTTP_J181909.0–164136	22.35	15.13	1.08	1.05
492	JCMTTP_J181909.7–164230	22.35	11.56	0.83	0.35
493	JCMTTP_J181812.0–170654	22.34	13.13	0.94	0.77
494	JCMTTP_J181740.7–165254	22.21	11.88	0.85	0.15

Table A1 *continued*

Table A1 (*continued*)

#	ID	f_m	SD	SD/SD _{fid}	$ S/\Delta S $
		(mJy beam $^{-1}$)	(mJy beam $^{-1}$)		
495	JCMTTP_J181859.3–170130	22.20	7.94	0.57	0.50
496	JCMTTP_J181839.2–163524	22.19	16.92	1.21	1.41
497	JCMTTP_J181943.6–165059	22.16	16.48	1.18	0.16
498	JCMTTP_J181847.2–170509	22.10	14.68	1.05	2.53
499	JCMTTP_J181749.5–163527	22.07	23.54	1.68	1.82
500	JCMTTP_J181930.2–165938	22.04	13.31	0.95	0.04
501	JCMTTP_J181859.5–165309	22.01	11.59	0.83	0.21
502	JCMTTP_J181903.5–170745	21.93	20.14	1.44	1.74
503	JCMTTP_J181839.0–164421	21.93	12.45	0.89	1.82
504	JCMTTP_J181758.9–163403	21.91	16.23	1.16	3.06
505	JCMTTP_J181907.5–170506	21.76	12.41	0.89	2.00
506	JCMTTP_J181849.4–165539	21.74	8.33	0.59	2.03
507	JCMTTP_J181755.8–164242	21.71	13.42	0.96	0.33
508	JCMTTP_J181745.6–170812	21.68	18.85	1.35	2.90
509	JCMTTP_J181833.1–163642	21.66	16.64	1.19	0.96
510	JCMTTP_J181933.3–164744	21.63	15.95	1.14	1.52
511	JCMTTP_J181913.3–165251	21.62	9.34	0.67	0.28
512	JCMTTP_J181842.3–164354	21.59	14.12	1.01	0.31
513	JCMTTP_J181853.0–170212	21.58	12.81	0.91	0.44
514	JCMTTP_J181750.4–163509	21.48	25.61	1.83	3.16
515	JCMTTP_J181729.9–163932	21.36	25.32	1.81	2.65
516	JCMTTP_J181935.6–164414	21.32	18.49	1.32	0.50
517	JCMTTP_J181808.1–163454	21.27	20.62	1.47	0.65
518	JCMTTP_J181758.6–170718	21.20	13.02	0.93	1.85
519	JCMTTP_J181936.5–165935	21.16	22.45	1.60	0.41
520	JCMTTP_J181905.3–170024	21.14	11.92	0.85	2.19
521	JCMTTP_J181730.6–165832	21.08	18.32	1.31	0.75
522	JCMTTP_J181800.5–164815	21.07	9.15	0.65	1.00
523	JCMTTP_J181743.8–170700	21.04	15.88	1.13	0.32
524	JCMTTP_J181902.6–165206	21.04	10.95	0.78	0.02
525	JCMTTP_J181853.2–170109	20.94	10.82	0.77	0.11
526	JCMTTP_J181914.5–164924	20.94	9.08	0.65	1.00
527	JCMTTP_J181928.2–163959	20.82	20.48	1.46	0.63
528	JCMTTP_J181931.4–165238	20.81	12.42	0.89	3.50
529	JCMTTP_J181845.0–164945	20.73	6.62	0.47	0.25
530	JCMTTP_J181939.2–165250	20.70	15.90	1.14	0.41
531	JCMTTP_J181915.2–170248	20.66	13.52	0.97	2.02
532	JCMTTP_J181748.3–163836	20.62	14.97	1.07	0.65
533	JCMTTP_J181752.0–165206	20.42	11.55	0.83	0.91
534	JCMTTP_J181911.3–164157	20.42	12.61	0.90	0.14
535	JCMTTP_J181828.1–163503	20.41	14.87	1.06	0.22
536	JCMTTP_J181822.7–163321	20.41	19.29	1.38	0.79
537	JCMTTP_J181937.3–165608	20.40	13.22	0.94	0.12
538	JCMTTP_J181815.6–165257	20.34	17.18	1.23	1.78
539	JCMTTP_J181831.7–170827	20.25	15.81	1.13	0.94
540	JCMTTP_J181807.0–164209	20.24	12.28	0.88	0.10
541	JCMTTP_J181914.5–163912	20.17	12.38	0.88	1.63
542	JCMTTP_J181853.0–163512	20.15	21.13	1.51	0.15
543	JCMTTP_J181900.7–165512	20.12	12.12	0.87	0.85
544	JCMTTP_J181834.2–165654	19.90	10.45	0.75	2.51
545	JCMTTP_J181758.2–170521	19.78	12.39	0.88	1.35
546	JCMTTP_J181727.9–165423	19.76	13.37	0.95	2.18

Table A1 *continued*

Table A1 (*continued*)

#	ID	f _m (mJy beam ⁻¹)	SD (mJy beam ⁻¹)	SD/SD _{fid}	S/ΔS
547	JCMTPP_J181926.9–165709	19.74	13.70	0.98	0.89
548	JCMTPP_J181740.9–164548	19.70	12.10	0.86	2.67
549	JCMTPP_J181735.5–165018	19.61	11.09	0.79	1.11
550	JCMTPP_J181711.4–165138	19.60	21.47	1.53	1.77
551	JCMTPP_J181758.2–164930	19.59	13.04	0.93	3.23
552	JCMTPP_J181820.2–164839	19.58	8.58	0.61	1.68
553	JCMTPP_J181942.9–165226	19.50	16.58	1.18	1.71
554	JCMTPP_J181932.3–165611	19.48	19.09	1.36	0.12
555	JCMTPP_J181855.0–163754	19.45	11.69	0.83	0.04
556	JCMTPP_J181917.4–164154	19.44	15.44	1.10	0.24
557	JCMTPP_J181729.6–164614	19.42	16.27	1.16	0.82
558	JCMTPP_J181810.6–163630	19.28	15.72	1.12	1.16
559	JCMTPP_J181858.4–163521	19.27	15.92	1.14	1.79
560	JCMTPP_J181750.4–170645	19.17	16.62	1.19	0.34
561	JCMTPP_J181853.2–163709	19.11	11.45	0.82	1.95
562	JCMTPP_J181913.5–165909	19.08	11.39	0.81	0.51
563	JCMTPP_J181739.1–163806	19.07	24.00	1.71	0.21
564	JCMTPP_J181740.3–164657	19.07	11.78	0.84	0.61
565	JCMTPP_J181849.0–170142	19.05	10.04	0.72	1.32
566	JCMTPP_J181806.4–163748	19.04	16.90	1.21	0.68
567	JCMTPP_J181835.2–170845	19.04	16.76	1.20	2.13
568	JCMTPP_J181905.5–165145	18.91	10.74	0.77	0.56
569	JCMTPP_J181922.0–165227	18.78	13.40	0.96	1.26
570	JCMTPP_J181916.6–164709	18.73	9.68	0.69	1.43
571	JCMTPP_J181811.4–170403	18.71	13.05	0.93	0.14
572	JCMTPP_J181756.2–164603	18.66	12.95	0.92	1.29
573	JCMTPP_J181748.7–163733	18.66	18.37	1.31	0.20
574	JCMTPP_J181721.2–165359	18.63	12.00	0.86	1.41
575	JCMTPP_J181851.3–164124	18.61	14.79	1.06	1.74
576	JCMTPP_J181743.8–170424	18.57	15.53	1.11	0.06
577	JCMTPP_J181906.6–165824	18.56	10.41	0.74	1.98
578	JCMTPP_J181923.7–165957	18.47	15.69	1.12	0.49
579	JCMTPP_J181915.1–164648	18.42	14.51	1.04	1.70
580	JCMTPP_J181748.4–170451	18.40	8.73	0.62	1.30
581	JCMTPP_J181845.3–170630	18.28	15.77	1.13	2.03
582	JCMTPP_J181857.0–165327	18.22	10.65	0.76	2.32
583	JCMTPP_J181739.0–165939	18.22	13.86	0.99	0.85
584	JCMTPP_J181755.5–165603	18.14	11.38	0.81	0.69
585	JCMTPP_J181916.5–163645	18.12	19.53	1.39	1.48
586	JCMTPP_J181720.3–164217	18.02	21.86	1.56	2.06
587	JCMTPP_J181732.8–164554	17.97	11.97	0.85	0.33
588	JCMTPP_J181757.6–170554	17.94	15.13	1.08	1.18
589	JCMTPP_J181735.3–164054	17.92	15.73	1.12	1.30
590	JCMTPP_J181708.9–164735	17.90	25.62	1.83	1.55
591	JCMTPP_J181819.1–164257	17.81	9.59	0.69	0.45
592	JCMTPP_J181827.3–163854	17.77	12.76	0.91	2.16
593	JCMTPP_J181716.5–164829	17.68	18.07	1.29	0.41
594	JCMTPP_J181728.8–164550	17.52	11.44	0.82	2.20
595	JCMTPP_J181729.5–170347	17.45	14.57	1.04	2.50
596	JCMTPP_J181858.7–170251	17.44	10.77	0.77	2.02
597	JCMTPP_J181917.0–165645	17.38	12.57	0.90	1.53
598	JCMTPP_J181835.4–170115	17.37	10.38	0.74	0.42

Table A1 *continued*

Table A1 (*continued*)

#	ID	f_m	SD	SD/SD _{fid}	$ S/\Delta S $
		(mJy beam $^{-1}$)	(mJy beam $^{-1}$)		
599	JCMTTP_J181936.2–165026	17.28	18.41	1.31	2.14
600	JCMTTP_J181744.4–165757	17.19	10.93	0.78	0.30
601	JCMTTP_J181748.2–164524	17.05	9.51	0.68	0.46
602	JCMTTP_J181809.3–170733	16.96	10.54	0.75	1.01
603	JCMTTP_J181927.7–170229	16.92	23.51	1.68	1.85
604	JCMTTP_J181831.9–164242	16.85	10.15	0.73	2.97
605	JCMTTP_J181744.2–165118	16.85	13.74	0.98	0.81
606	JCMTTP_J181915.6–165609	16.81	12.64	0.90	0.13
607	JCMTTP_J181918.2–164124	16.81	13.51	0.96	1.63
608	JCMTTP_J181736.9–164800	16.76	12.90	0.92	0.16
609	JCMTTP_J181749.7–165309	16.74	11.65	0.83	0.48
610	JCMTTP_J181826.4–170803	16.70	13.95	1.00	0.19
611	JCMTTP_J181807.9–163736	16.61	12.72	0.91	1.39
612	JCMTTP_J181831.3–163754	16.47	10.90	0.78	1.01
613	JCMTTP_J181939.0–165414	16.45	13.42	0.96	1.55
614	JCMTTP_J181906.8–164621	16.40	13.85	0.99	1.61
615	JCMTTP_J181751.5–165103	16.35	10.51	0.75	0.39
616	JCMTTP_J181802.2–164157	16.17	13.92	0.99	0.70
617	JCMTTP_J181928.5–165502	16.08	14.64	1.05	2.35
618	JCMTTP_J181917.4–165136	15.94	11.77	0.84	0.80
619	JCMTPP_J181816.6–165333	15.92	11.56	0.83	0.66
620	JCMTPP_J181747.8–164021	15.89	15.18	1.08	1.10
621	JCMTPP_J181741.1–170200	15.81	13.85	0.99	0.17
622	JCMTPP_J181747.0–163909	15.75	17.00	1.21	2.07
623	JCMTPP_J181920.0–165527	15.69	13.38	0.96	1.65
624	JCMTPP_J181911.8–164639	15.61	8.57	0.61	1.84
625	JCMTPP_J181843.0–170151	15.57	13.45	0.96	0.13
626	JCMTPP_J181801.6–163933	15.51	17.67	1.26	1.36
627	JCMTPP_J181920.3–164130	15.50	13.99	1.00	0.87
628	JCMTPP_J181752.6–164757	15.50	10.66	0.76	0.58
629	JCMTPP_J181751.1–164703	15.48	11.89	0.85	0.54
630	JCMTPP_J181805.2–163951	15.42	12.19	0.87	0.34
631	JCMTPP_J181859.9–170433	15.41	15.89	1.14	2.06
632	JCMTPP_J181741.7–164951	15.25	14.13	1.01	1.36
633	JCMTPP_J181728.1–165332	15.19	14.47	1.03	1.71
634	JCMTPP_J181730.5–164847	15.18	14.41	1.03	0.96
635	JCMTPP_J181819.1–163536	15.13	16.77	1.20	1.83
636	JCMTPP_J181813.0–170818	15.11	16.37	1.17	2.27
637	JCMTPP_J181818.5–165315	15.06	13.94	1.00	0.01
638	JCMTPP_J181808.0–170548	14.91	19.71	1.41	0.83
639	JCMTPP_J181929.7–164238	14.73	17.18	1.23	0.85
640	JCMTPP_J181858.8–164500	14.70	10.95	0.78	0.89
641	JCMTPP_J181914.5–164003	14.61	11.57	0.83	0.70
642	JCMTPP_J181745.9–164206	14.60	16.88	1.21	1.62
643	JCMTPP_J181903.3–170133	14.60	11.15	0.80	1.44
644	JCMTPP_J181843.6–163621	14.49	13.46	0.96	1.01
645	JCMTPP_J181730.5–164250	14.43	19.54	1.40	0.10
646	JCMTPP_J181752.4–164712	14.26	8.47	0.61	0.46
647	JCMTPP_J181834.4–165518	14.25	11.27	0.80	0.39
648	JCMTPP_J181902.4–170300	14.24	10.15	0.73	0.12
649	JCMTPP_J181832.1–170403	14.15	13.29	0.95	3.65
650	JCMTPP_J181738.2–164251	14.08	7.49	0.53	1.73

Table A1 *continued*

Table A1 (*continued*)

#	ID	f_m	SD	SD/SD _{fid}	$ S/\Delta S $
		(mJy beam $^{-1}$)	(mJy beam $^{-1}$)		
651	JCMTPP_J181743.2–164912	14.07	12.11	0.86	1.66
652	JCMTPP_J181817.9–170457	13.85	17.30	1.24	0.34
653	JCMTPP_J181750.5–164912	13.70	13.58	0.97	1.63
654	JCMTPP_J181929.8–165411	13.63	17.01	1.21	1.30
655	JCMTPP_J181917.0–164557	13.61	13.55	0.97	1.57
656	JCMTPP_J181734.5–164306	13.59	11.58	0.83	2.34
657	JCMTPP_J181745.5–164003	13.45	18.39	1.31	1.28
658	JCMTPP_J181848.0–170112	13.43	13.97	1.00	0.73
659	JCMTPP_J181922.5–165403	13.42	15.85	1.13	1.14
660	JCMTPP_J181805.7–170900	13.36	17.40	1.24	1.85
661	JCMTPP_J181811.6–170957	13.17	20.52	1.47	2.70
662	JCMTPP_J181840.9–164409	13.16	12.17	0.87	0.70
663	JCMTPP_J181744.6–165500	13.01	11.39	0.81	2.21

B. VARIABILITY MEASUREMENTS FROM NEOWISE LIGHT CURVES FOR FINAL SAMPLE YSOS

We present the variability measures derived from NEOWISE light curves from the final sample of YSOs analyzed in our study, covering both the W1 and W2 bands. Table B2 lists these measures from the 47 YSOs identified as exhibiting robust mid-IR variability across the six investigated types. Table B3 provides details for the remaining 132 YSOs in the final sample that did not exhibit detectable mid-IR variability. For completeness, Figure B1 shows mid-IR light curves for the 40 YSOs identified as exhibiting robust mid-IR variability, but not included in Figure 9.

REFERENCES

- Astropy Collaboration, Robitaille, T. P., Tollerud, E. J., et al. 2013, A&A, 558, A33, doi: [10.1051/0004-6361/201322068](https://doi.org/10.1051/0004-6361/201322068)
- Astropy Collaboration, Price-Whelan, A. M., Sipőcz, B. M., et al. 2018, AJ, 156, 123, doi: [10.3847/1538-3881/aabc4f](https://doi.org/10.3847/1538-3881/aabc4f)
- Baek, G., MacFarlane, B. A., Lee, J.-E., et al. 2020, ApJ, 895, 27, doi: [10.3847/1538-4357/ab8ad4](https://doi.org/10.3847/1538-4357/ab8ad4)
- Baraffe, I., & Chabrier, G. 2010, A&A, 521, A44, doi: [10.1051/0004-6361/201014979](https://doi.org/10.1051/0004-6361/201014979)
- Berry, D. S. 2015, Astronomy and Computing, 10, 22, doi: [10.1016/j.ascom.2014.11.004](https://doi.org/10.1016/j.ascom.2014.11.004)
- Billot, N., Morales-Calderón, M., Stauffer, J. R., Megeath, S. T., & Whitney, B. 2012, ApJL, 753, L35, doi: [10.1088/2041-8205/753/2/L35](https://doi.org/10.1088/2041-8205/753/2/L35)
- Bonato, M., Liuzzo, E., Giannetti, A., et al. 2018, MNRAS, 478, 1512, doi: [10.1093/mnras/sty1173](https://doi.org/10.1093/mnras/sty1173)
- Bouvier, J., Grankin, K., Ellerbroek, L. E., Bouy, H., & Barrado, D. 2013, A&A, 557, A77, doi: [10.1051/0004-6361/201321389](https://doi.org/10.1051/0004-6361/201321389)
- Caramazza, M., Flaccomio, E., Micela, G., et al. 2007, A&A, 471, 645, doi: [10.1051/0004-6361:20077195](https://doi.org/10.1051/0004-6361:20077195)
- Carpenter, J. M., Hillenbrand, L. A., & Skrutskie, M. F. 2001, AJ, 121, 3160, doi: [10.1086/321086](https://doi.org/10.1086/321086)
- Cody, A. M., Stauffer, J., Baglin, A., et al. 2014, AJ, 147, 82, doi: [10.1088/0004-6256/147/4/82](https://doi.org/10.1088/0004-6256/147/4/82)
- Condon, J. J., Cotton, W. D., Greisen, E. W., et al. 1998, AJ, 115, 1693, doi: [10.1086/300337](https://doi.org/10.1086/300337)
- Contreras, Y., Schuller, F., Urquhart, J. S., et al. 2013, A&A, 549, A45, doi: [10.1051/0004-6361/201220155](https://doi.org/10.1051/0004-6361/201220155)
- Contreras Peña, C., Johnstone, D., Baek, G., et al. 2020, MNRAS, 495, 3614, doi: [10.1093/mnras/staa1254](https://doi.org/10.1093/mnras/staa1254)
- Dempsey, J. T., Friberg, P., Jenness, T., et al. 2013, MNRAS, 430, 2534, doi: [10.1093/mnras/stt090](https://doi.org/10.1093/mnras/stt090)

Table B2. Properties of NEOWISE Light Curves for Potential Variable Mid-Infrared Sources

#	ID ^a	R.A.	Dec.	N	$\Delta(W)$	SD	σ	S^b	Period ^c			Class ^e	Outside ^f	Corr. ^g	
		(deg)	(deg)	(mag)	(mag)	(mag)	(%/yr)	(yr)	FAP _{Lin}	FAP _{LSP}	Type ^d				
1	SPICY 79195	274.3010	-16.9586	18	0.310	0.084	0.049	7.4e-01	6.7e-02	...	0/I	...	C
				18	0.452	0.106	0.035	6.7e-01	6.8e-02	irregular			
2	SPICY 79250	274.3144	-16.8679	18	1.338	0.438	0.109	...	1.496	9.0e-01	6.5e-04	periodic	III	Y	A
				18	1.057	0.370	0.125	...	1.496	9.5e-01	6.1e-07	periodic			
3	SPICY 79296	274.3211	-16.9943	18	0.288	0.079	0.055	-2.798	10.021	8.0e-03	2.4e-03	curved	0/I	...	C
				18	0.266	0.071	0.122	2.6e-01	2.7e-02	...			
4	SPICY 79425	274.3571	-17.0367	18	4.440	1.183	0.195	5.4e-01	5.0e-02	irregular	0/I	...	A
				18	3.334	0.921	0.084	+10.315	6.795	1.2e-01	1.5e-04	curved			
5	SPICY 79472	274.3713	-17.0259	18	0.322	0.087	0.088	8.6e-03	3.1e-02	...	II	...	A
				18	0.406	0.099	0.070	-2.617	13.142	1.2e-02	7.5e-03	curved			
6	SPICY 79570	274.3998	-17.0254	18	1.546	0.567	0.075	...	1.900	1.0e+00	2.9e-05	periodic	0/I	...	A
				18	1.865	0.673	0.171	...	1.990	9.9e-01	1.0e-03	periodic			
7	SPICY 79654	274.4286	-16.6908	18	1.611	0.480	0.123	...	0.701	4.8e-01	3.2e-03	periodic	II	Y	A
				18	1.550	0.540	0.206	...	0.701	8.2e-01	1.2e-03	periodic			
8	SPICY 79718	274.4512	-17.0021	18	1.432	0.402	0.278	5.0e-01	7.2e-02	...	0/I	...	A
				18	1.131	0.272	0.069	2.4e-01	3.2e-02	irregular			
9	SPICY 79863	274.4892	-16.9892	18	0.617	0.157	0.063	1.0e+00	1.4e-01	...	II	...	A
				18	0.530	0.152	0.042	1.0e+00	4.1e-02	irregular			
10	SPICY 79885	274.4933	-17.0445	18	0.770	0.231	0.067	+8.660	...	1.3e-06	3.1e-05	linear	0/I	...	A
				18	0.684	0.197	0.051	+9.627	...	4.4e-06	1.7e-04	linear			
11	SPICY 80019	274.5253	-16.8960	18	0.284	0.092	0.082	-0.488	5.139	8.4e-01	4.7e-03	curved	II	...	B ^h
				18	0.419	0.117	0.099	1.0e+00	7.1e-02	...			
12	SPICY 80029	274.5272	-16.9432	17	0.638	0.166	0.161	+2.579	13.142	1.0e-04	1.0e-03	curved	II	...	C ^h
				17	0.544	0.140	0.168	5.5e-02	1.5e-02	...			
13	SPICY 80035	274.5285	-16.8555	18	2.061	0.675	0.108	+15.749	...	6.5e-09	1.8e-08	linear	0/I	...	A
				18	1.766	0.600	0.051	+25.185	...	7.4e-09	8.9e-07	linear			
14	SPICY 80128	274.5481	-16.8603	18	1.347	0.345	0.231	8.2e-03	4.1e-02	...	0/I	...	A
				18	1.134	0.310	0.065	+10.372	13.142	1.7e-03	5.4e-03	curved			
15	SPICY 80156	274.5508	-16.9565	18	0.354	0.101	0.030	8.3e-03	2.1e-02	irregular	0/I	...	A
				18	0.258	0.078	0.046	3.6e-02	4.7e-01	...			
16	SPICY 80256	274.5755	-16.7800	18	0.327	0.090	0.070	-1.360	8.100	2.6e-01	1.1e-03	curved	0/I	...	A
				18	0.325	0.091	0.059	-1.855	8.100	2.0e-01	2.4e-04	curved			
17	SPICY 80368	274.6062	-16.9019	15	3.534	1.045	0.164	-20.394	...	2.6e-05	2.4e-04	linear	0/I	...	A
				15	1.554	0.471	0.064	-17.271	13.142	5.7e-04	6.9e-03	curved			
18	SPICY 80417	274.6194	-16.9235	18	0.930	0.343	0.084	+12.335	...	2.2e-10	3.0e-09	linear	0/I	...	A
				18	0.909	0.308	0.052	+18.046	...	6.1e-09	3.1e-08	linear			
19	SPICY 80429	274.6207	-16.7136	18	1.488	0.427	0.079	1.2e-01	3.2e-02	irregular	II	...	A
				18	1.260	0.379	0.045	...	0.875	5.2e-01	1.1e-05	periodic			
20	SPICY 80463	274.6312	-16.8701	18	0.726	0.201	0.075	-2.256	4.133	4.9e-01	5.0e-04	curved	II	...	A
				18	0.892	0.234	0.063	6.2e-02	1.6e-01	irregular			
21	SPICY 80519	274.6432	-17.1025	18	0.672	0.217	0.157	7.6e-01	1.0e-02	...	II	Y	A
				18	0.528	0.159	0.085	...	0.857	1.0e+00	3.1e-05	periodic			
22	SPICY 80528	274.6456	-17.1659	18	1.435	0.401	0.076	3.5e-01	2.8e-02	irregular	0/I	Y	A
				18	1.362	0.352	0.043	4.6e-01	2.5e-01	irregular			
23	SPICY 80529	274.6471	-17.1579	18	0.348	0.088	0.163	2.3e-02	2.4e-02	...	0/I	Y	D
				18	0.247	0.071	0.049	+0.457	5.852	9.1e-01	2.1e-04	curved			
24	SPICY 80587	274.6583	-16.8401	18	0.665	0.137	0.173	1.1e-01	3.9e-01	...	II	...	B ^h
				18	0.534	0.152	0.072	+5.212	13.142	4.2e-04	3.4e-04	curved			
25	SPICY 80736	274.6866	-16.9915	18	0.306	0.080	0.108	1.8e-01	3.4e-04	...	0/I	...	C ^h
				18	0.307	0.079	0.090	+1.633	6.794	3.1e-02	1.3e-03	curved			
26	SPICY 80781	274.6954	-16.6735	18	1.321	0.358	0.106	9.6e-01	1.2e-02	irregular	0/I	...	A
				18	0.997	0.265	0.053	8.3e-01	1.2e-02	irregular			
27	SPICY 80831	274.7091	-16.8556	18	0.555	0.135	0.059	2.7e-01	5.9e-02	...	II	...	A
				18	0.753	0.168	0.051	2.1e-01	1.9e-02	irregular			
28	SPICY 80884	274.7238	-16.5977	18	1.475	0.504	0.068	...	0.668	2.7e-01	2.3e-04	periodic	0/I	...	A
				18	1.763	0.627	0.134	...	1.989	6.3e-01	1.9e-03	periodic			
29	SPICY 80886	274.7245	-16.6353	18	0.244	0.060	0.063	2.0e-03	1.3e-02	...	II	...	B ^h
				18	0.395	0.105	0.059	-4.129	13.142	2.5e-04	4.9e-03	curved			
30	SPICY 80890	274.7266	-16.6967	18	0.558	0.149	0.053	-4.801	4.581	3.0e-02	8.2e-03	curved	0/I	...	A
				18	0.661	0.188	0.048	1.4e-02	1.6e-02	irregular			
31	SPICY 80975	274.7503	-16.6571	18	0.252	0.071	0.086	4.4e-04	3.0e-04	...	II	...	C ^h
				18	0.351	0.095	0.101	...	1.076	1.1e-01	4.2e-04	periodic			
32	SPICY 81009	274.7601	-16.9048	18	1.320	0.370	0.151	6.9e-01	8.4e-02	...	0/I	...	A
				18	0.945	0.272	0.053	9.8e-01	8.2e-01	irregular			
33	SPICY 81013	274.7613	-16.6910	18	0.716	0.185	0.107	6.7e-01	3.2e-02	...	II	...	B ^h
				18	0.721	0.198	0.077	...	1.674	8.5e-01	2.0e-03	periodic			
34	SPICY 81														

Table B2. Continued from previous page

#	ID ^a	R.A. (deg)	Dec. (deg)	N	$\Delta(W)$ (mag)	SD (mag)	σ (mag)	S^b	Period ^c (yr)	FAP _{Lin}	FAP _{LSP}	Type ^d	Class ^e	Outside ^f	Corr. ^g
36	SPICY 81140	274.7921	-16.6523	18	0.751	0.251	0.077	+6.771	10.021	4.9e-03	3.0e-04	curved	II	...	A
				18	0.695	0.242	0.051	+10.444	10.021	1.8e-03	5.8e-04	curved			
37	SPICY 81164	274.7980	-16.8000	18	0.246	0.072	0.102	1.1e-01	4.4e-04	...	II	...	C ^h
				18	0.230	0.069	0.059	-0.138	8.099	9.9e-01	4.9e-04	curved			
38	SPICY 81226	274.8124	-16.8308	18	0.395	0.108	0.237	1.6e-01	5.5e-01	...	0/I	...	D
				18	0.417	0.102	0.050	+5.404	...	4.7e-06	1.3e-03	linear			
39	SPICY 81374	274.8585	-17.0125	18	0.566	0.151	0.092	6.7e-01	3.9e-02	...	0/I	Y	A
				18	0.515	0.126	0.047	-1.994	6.794	6.1e-01	6.5e-03	curved			
40	SPICY 81450	274.8866	-16.7596	18	0.880	0.246	0.058	5.3e-03	3.8e-02	irregular	II	...	A
				18	0.799	0.220	0.049	4.7e-02	2.9e-02	irregular			
41	SPICY 81451	274.8867	-16.7533	18	0.433	0.099	0.160	1.0e+00	3.4e-02	...	0/I	...	D
				18	2.350	0.601	0.058	9.6e-03	1.1e-01	irregular			
42	GLMA G014.1520-00.5173	274.5214	-16.8952	18	0.292	0.084	0.058	-2.897	13.142	2.2e-03	8.0e-03	curved	0/I	...	B
				18	0.482	0.148	0.105	-3.083	...	7.4e-05	2.4e-03	linear			
43	GLMA G014.1999-00.5875	274.6098	-16.8862	16	1.461	0.330	0.140	...	1.445	4.0e-01	4.4e-03	periodic	II	...	B
				16	1.531	0.376	0.242	...	1.444	7.7e-01	9.9e-05	periodic			
44	GLMA G014.2057-00.5937	274.6183	-16.8841	17	0.998	0.281	0.195	1.2e-01	1.7e-02	...	II	...	B
				17	0.785	0.245	0.082	...	1.000	3.0e-01	1.3e-04	periodic			
45	GLMA G014.2125-00.6368	274.6614	-16.8986	18	0.950	0.290	0.088	4.5e-02	2.4e-02	irregular	0/I	...	A
				18	0.689	0.190	0.054	-3.823	5.851	2.8e-01	9.2e-03	curved			
46	GLMA G014.2370-00.5063	274.5534	-16.8151	18	0.155	0.038	0.087	7.2e-01	1.1e-01	...	0/I	...	D
				18	0.220	0.049	0.059	3.5e-01	4.2e-02	burst			
47	GLMA G014.4640-00.5961	274.7482	-16.6577	18	1.061	0.357	0.192	...	0.913	1.0e+00	1.4e-06	periodic	II	...	A
				18	1.092	0.378	0.202	9.4e-01	9.6e-07	...			

NOTE—In the table, where two values are stacked vertically, the top value corresponds to W1 while the bottom value denotes W2.

^a All source identifiers (IDs) are based on designations from two key references: Kuhn et al. (2021) and Povich & Whitney (2010). Kuhn et al. (2021) utilizes the SPICY (Spitzer/IRAC Candidate YSO) numbering system, while Povich & Whitney (2010) refer to sources by their GLIMPSE Archive (GLMA) coordinates. SPICY IDs are numerical, whereas GLMA IDs are presented in a Galactic coordinate format.

^b Best-fit linear slope.

^c LSP period for periodic or curved sources.

^d Variable type.

^e YSO classification.

^f All sources are presumed to be associated with M17 SWEx, unless marked as ‘outside’ (Y) in accordance with the determinations by Kuhn et al. (2021).

^g The Spearman correlation between WISE W1 and W2 light curves. categories are as follows: A = strong positive correlation, B = moderate-to-strong positive correlation, C = weak-to-moderate positive correlation, D = No or very weak correlation.

^h Those who show notable differences between the original and simulated data.

Table B3. Statistics of NEOWISE Light Curves for Non-Variable Mid-Infrared Sources

#	ID ^a	R.A. (deg)	Dec. (deg)	N	$\Delta(W)$ (mag)	SD (mag)	σ (mag)	FAP _{Lin}	FAP _{LSP}	Class ^b	Outside ^c
1	SPICY 79255	274.3150	-16.9375	17	0.905	0.216	0.205	7.5e-01	5.2e-01	II	...
				17	0.313	0.083	0.196	2.5e-01	5.3e-01		
2	SPICY 79278	274.3184	-16.9781	18	0.282	0.066	0.045	9.6e-01	5.1e-01	II	...
				18	0.317	0.067	0.047	7.4e-01	3.7e-01		
3	SPICY 79352	274.3393	-16.8787	18	0.283	0.071	0.105	4.6e-01	7.9e-02	0/I	...
				18	0.443	0.107	0.064	7.1e-02	4.7e-02		
4	SPICY 79376	274.3441	-16.9843	18	0.368	0.106	0.203	5.4e-01	3.2e-01	0/I	...
				18	0.126	0.030	0.100	8.7e-01	8.4e-01		
5	SPICY 79423	274.3565	-17.0686	16	0.743	0.176	0.195	9.5e-01	5.0e-01	II	...
				16	0.286	0.076	0.148	9.1e-01	2.7e-01		
6	SPICY 79441	274.3617	-17.0703	18	0.282	0.071	0.158	9.5e-01	8.2e-02	0/I	...
				18	0.127	0.032	0.073	4.8e-01	4.0e-01		
7	SPICY 79452	274.3648	-17.0273	18	0.594	0.147	0.236	6.1e-02	4.5e-01	0/I	...
				18	0.378	0.103	0.107	4.2e-01	4.1e-01		
8	SPICY 79525	274.3898	-16.8455	18	0.475	0.113	0.073	1.2e-01	3.9e-01	II	Y
				18	0.412	0.086	0.056	1.0e-01	9.3e-02		
9	SPICY 79533	274.3923	-17.0346	18	0.548	0.164	0.164	2.0e-01	8.8e-01	II	...
				18	0.581	0.168	0.079	2.4e-01	8.1e-01		
10	SPICY 79620	274.4155	-17.0934	18	0.555	0.161	0.125	1.5e-01	5.6e-01	II	...
				18	0.577	0.143	0.124	8.7e-01	6.0e-01		
11	SPICY 79731	274.4543	-16.9910	18	0.333	0.097	0.130	6.7e-01	1.5e-02	II	...
				18	0.464	0.133	0.083	6.2e-01	1.4e-01		
12	SPICY 79778	274.4668	-16.9226	18	0.139	0.033	0.126	6.3e-01	9.5e-01	II	...
				18	0.159	0.038	0.116	1.6e-03	1.4e-02		
13	SPICY 79831	274.4785	-16.9234	18	0.311	0.085	0.049	1.0e+00	3.8e-01	II	...
				18	0.293	0.086	0.046	7.8e-01	3.8e-01		
14	SPICY 79839	274.4799	-16.9747	18	0.181	0.054	0.055	1.7e-01	4.4e-02	0/I	...
				18	0.229	0.057	0.065	1.1e-01	2.5e-02		
15	SPICY 79859	274.4865	-16.8730	18	0.239	0.065	0.111	1.3e-02	2.0e-02	0/I	...
				18	0.144	0.043	0.058	4.7e-02	3.6e-02		
16	SPICY 79882	274.4931	-17.1085	17	1.654	0.384	0.382	7.3e-01	3.9e-02	II	...
				17	0.741	0.197	0.137	9.5e-01	7.7e-02		
17	SPICY 79886	274.4939	-17.0483	15	0.266	0.078	0.156	9.9e-01	8.3e-01	II	...
				15	0.344	0.080	0.144	6.7e-01	2.7e-02		
18	SPICY 79887	274.4940	-17.1091	15	1.854	0.430	0.365	5.2e-01	2.8e-01	II	Y
				15	0.730	0.177	0.147	9.9e-01	2.3e-01		
19	SPICY 79925	274.5046	-16.9515	15	0.463	0.125	0.166	9.8e-01	7.4e-02	II	...
				15	0.841	0.245	0.194	2.4e-01	1.9e-01		
20	SPICY 79928	274.5049	-16.8936	18	0.545	0.126	0.216	9.7e-01	3.3e-02	II	...
				18	0.481	0.115	0.115	8.0e-01	3.7e-01		
21	SPICY 79954	274.5117	-16.8889	15	2.740	0.671	0.396	9.1e-01	2.6e-02	II	...
				15	0.258	0.069	0.146	4.6e-01	7.5e-01		
22	SPICY 80024	274.5264	-16.8705	18	0.691	0.187	0.194	6.7e-01	6.9e-01	0/I	...
				18	0.674	0.168	0.175	6.6e-01	1.4e-01		
23	SPICY 80028	274.5271	-16.9136	18	0.372	0.090	0.130	6.5e-01	1.3e-02	II	...
				18	0.467	0.130	0.124	2.0e-01	1.4e-01		
24	SPICY 80044	274.5319	-16.9533	18	0.628	0.179	0.295	5.8e-02	2.4e-02	0/I	...
				18	0.505	0.136	0.065	1.1e-02	2.2e-02		
25	SPICY 80071	274.5378	-16.9773	18	0.397	1.091	0.037	6.1e-01	2.2e-01	II	...
				18	0.429	0.097	0.067	6.3e-01	5.2e-01		
26	SPICY 80074	275.5382	-16.6283	17	0.429	0.096	0.115	5.1e-02	9.8e-02	II	Y
				17	0.193	0.051	0.085	6.3e-01	4.3e-03		
27	SPICY 80081	274.5398	-16.8360	18	0.350	0.096	0.125	6.1e-03	3.8e-02	0/I	...
				18	0.219	0.059	0.054	2.6e-03	3.5e-02		
28	SPICY 80087	274.5409	-16.8699	18	0.324	0.095	0.193	1.5e-02	3.0e-02	II	...
				18	0.214	0.056	0.053	4.4e-01	6.3e-01		
29	SPICY 80111	274.5449	-16.8203	18	0.294	0.082	0.170	1.8e-02	9.0e-03	0/I	...
				18	0.282	0.071	0.107	9.7e-02	5.4e-04		
30	SPICY 80115	274.5454	-16.8214	16	0.585	0.165	0.177	8.2e-01	1.7e-01	0/I	...
				16	0.285	0.074	0.152	1.9e-01	4.5e-01		
31	SPICY 80132	274.5483	-16.9914	18	0.074	0.023	0.098	7.8e-01	3.7e-01	II	...
				18	0.099	0.030	0.073	4.6e-01	2.8e-01		
32	SPICY 80137	274.5489	-16.8487	17	1.725	0.387	0.210	9.6e-02	4.9e-01	0/I	...
				17	0.342	0.079	0.129	9.2e-01	9.4e-01		
33	SPICY 80142	274.5493	-16.7684	18	0.420	0.131	0.176	5.5e-01	1.1e-01	II	...
				18	0.143	0.042	0.042	2.9e-02	1.9e-02		
34	SPICY 80148	274.5496	-16.9072	18	0.242	0.061	0.100	9.7e-01	4.3e-01	0/I	...
				18	0.122	0.034	0.051	6.2e-01	1.8e-01		
35	SPICY 80161	274.5515	-16.8237	18	0.872	0.189	0.188	2.5e-01	3.1e-02	0/I	...
				18	0.510	0.129	0.102	8.4e-02	2.3e-01		

NOTE—Continued on next page

Table B3. Continued from previous page

#	ID ^a	R.A. (deg)	Dec. (deg)	N	$\Delta(W)$ (mag)	SD (mag)	σ (mag)	FAP _{Lin}	FAP _{LSP}	Class ^b	Outside ^c
36	SPICY 80170	274.5523	-16.8179	18	0.374	0.079	0.060	8.5e-01	1.7e-02	II	...
				18	0.395	0.082	0.072	8.4e-01	1.2e-02		
37	SPICY 80173	274.5530	-16.8240	17	0.619	0.167	0.171	3.1e-01	1.9e-02	II	...
				17	0.445	0.114	0.099	4.0e-01	3.2e-01		
38	SPICY 80175	274.5531	-16.8173	18	0.333	0.077	0.065	1.0e+00	3.1e-01	uncertain	...
				18	0.353	0.078	0.069	1.0e+00	2.0e-01		
39	SPICY 80203	274.5607	-16.7960	18	0.306	0.078	0.128	2.7e-01	7.5e-01	II	...
				18	0.207	0.048	0.074	4.1e-01	3.8e-01		
40	SPICY 80214	274.5635	-16.8258	18	0.218	0.055	0.131	5.7e-02	2.4e-02	0/I	...
				18	0.239	0.074	0.085	9.7e-01	2.0e-02		
41	SPICY 80255	274.5753	-16.7754	18	0.233	0.054	0.113	7.6e-01	3.4e-02	II	...
				18	0.080	0.026	0.054	1.3e-02	8.3e-03		
42	SPICY 80277	274.5795	-16.9806	18	0.576	0.155	0.148	1.3e-01	4.9e-01	II	...
				18	0.667	0.172	0.065	4.5e-03	3.4e-02		
43	SPICY 80295	274.5854	-16.9480	18	0.484	0.113	0.114	5.0e-02	4.1e-02	0/I	...
				18	0.389	0.112	0.046	1.7e-02	7.7e-02		
44	SPICY 80316	274.5893	-16.9811	18	0.265	0.072	0.154	4.2e-01	3.1e-01	II	...
				18	0.129	0.036	0.075	1.7e-01	4.2e-02		
45	SPICY 80342	274.5973	-16.8191	18	0.727	0.159	0.133	8.2e-01	4.6e-01	II	...
				18	0.519	0.130	0.060	5.2e-01	4.9e-01		
46	SPICY 80345	274.5985	-16.9398	17	0.490	0.109	0.120	3.7e-01	9.7e-01	II	...
				17	0.410	0.102	0.124	8.7e-01	1.6e-01		
47	SPICY 80357	274.6030	-16.9244	18	0.221	0.054	0.061	3.4e-01	4.8e-01	II	...
				18	0.237	0.056	0.044	6.1e-01	5.6e-02		
48	SPICY 80364	274.6047	-16.8233	18	0.454	0.087	0.084	8.5e-01	4.2e-02	II	...
				18	0.500	0.103	0.052	9.7e-01	2.5e-02		
49	SPICY 80370	274.6067	-16.8181	18	0.629	0.173	0.058	1.5e-02	1.1e-01	0/I	...
				18	0.625	0.162	0.056	6.4e-02	1.2e-01		
50	SPICY 80375	274.6082	-16.8423	18	0.120	0.035	0.068	7.1e-01	1.2e-01	II	...
				18	0.164	0.046	0.062	9.5e-01	1.5e-01		
51	SPICY 80380	274.6099	-16.7665	13	0.757	0.220	0.152	2.6e-01	5.4e-02	II	...
				13	0.473	0.124	0.153	2.1e-01	4.9e-02		
52	SPICY 80410	274.6182	-16.7735	14	1.281	0.355	0.391	5.8e-01	4.7e-01	II	...
				14	0.433	0.144	0.091	9.7e-01	7.3e-02		
53	SPICY 80415	274.6193	-16.9451	18	0.186	0.044	0.086	6.1e-01	4.3e-01	II	...
				18	0.177	0.044	0.051	1.7e-01	6.1e-02		
54	SPICY 80470	274.6319	-16.6346	12	0.257	0.070	0.184	9.6e-01	4.8e-02	II	...
				12	0.227	0.062	0.194	6.8e-01	2.2e-01		
55	SPICY 80484	274.6350	-16.9239	18	0.438	0.093	0.132	3.3e-01	2.3e-01	II	...
				18	0.223	0.060	0.110	5.9e-01	5.6e-03		
56	SPICY 80488	274.6355	-16.9016	18	0.397	0.093	0.135	2.0e-01	6.4e-02	II	...
				18	0.371	0.086	0.114	1.4e-02	2.0e-02		
57	SPICY 80492	274.6359	-16.8190	12	0.927	0.279	0.463	9.9e-01	1.6e-01	0/I	...
				12	0.732	0.199	0.118	5.6e-01	6.6e-02		
58	SPICY 80498	274.6369	-16.6970	18	0.357	0.100	0.119	9.0e-01	3.0e-01	II	...
				18	0.402	0.104	0.065	8.8e-01	5.3e-01		
59	SPICY 80500	274.6382	-16.7009	18	0.516	0.131	0.145	9.6e-01	6.9e-01	II	...
				18	0.520	0.130	0.052	9.5e-01	3.3e-01		
60	SPICY 80527	274.6453	-16.9038	18	0.626	0.153	0.174	2.0e-02	4.2e-02	0/I	...
				18	0.569	0.159	0.069	1.7e-02	1.2e-01		
61	SPICY 80551	274.6514	-16.8983	12	0.682	0.186	0.158	9.9e-01	7.9e-01	II	...
				12	0.649	0.175	0.150	6.4e-01	3.2e-01		
62	SPICY 80562	274.6536	-16.8271	18	0.802	0.197	0.318	9.1e-01	2.7e-01	II	...
				18	0.111	0.032	0.082	5.9e-01	4.1e-01		
63	SPICY 80569	274.6545	-16.8054	18	0.472	0.110	0.205	5.6e-01	8.2e-01	II	...
				18	0.261	0.084	0.141	9.3e-01	9.2e-01		
64	SPICY 80573	274.6556	-16.8325	18	0.246	0.058	0.112	7.6e-02	7.9e-02	II	...
				18	0.223	0.061	0.074	9.0e-01	3.6e-01		
65	SPICY 80582	274.6571	-16.8043	18	0.334	0.081	0.183	5.6e-01	3.1e-02	II	...
				18	0.256	0.076	0.153	4.4e-01	1.4e-01		
66	SPICY 80597	274.6610	-16.8007	14	0.682	0.202	0.255	8.3e-01	7.2e-01	II	...
				14	0.623	0.182	0.149	4.8e-01	3.7e-01		
67	SPICY 80632	274.6660	-16.6754	15	0.463	0.114	0.160	6.8e-01	3.5e-01	II	...
				15	0.274	0.076	0.105	6.2e-01	5.4e-03		
68	SPICY 80639	274.6671	-16.7987	13	0.388	0.135	0.210	9.8e-01	4.0e-02	II	...
				13	0.350	0.098	0.194	7.5e-03	3.0e-03		
69	SPICY 80685	274.6749	-16.8768	17	0.453	0.117	0.120	7.5e-01	2.0e-01	II	...
				17	0.359	0.124	0.141	2.9e-01	5.2e-01		
70	SPICY 80692	274.6760	-16.8982	15	0.593	0.150	0.207	5.8e-01	9.0e-01	II	...
				15	0.455	0.149	0.173	1.3e-01	2.1e-01		

NOTE—Continued on next page

Table B3. Continued from previous page

#	R.A. ID ^a	Dec. (deg)	N	$\Delta(W)$ (mag)	SD (mag)	σ (mag)	FAP _{Lin}	FAP _{LSP}	Class ^b	Outside ^c
71	SPICY 80749	274.6888	-16.5462	18 0.308	0.079	0.069	6.2e-01	3.8e-02	0/I	Y
				18 0.422	0.108	0.059	1.0e+00	3.8e-02		
72	SPICY 80814	274.7041	-16.8393	14 0.765	0.258	0.168	5.9e-01	2.5e-02	II	...
				14 0.937	0.226	0.174	6.8e-01	3.7e-02		
73	SPICY 80835	274.7117	-16.8712	16 0.717	0.146	0.166	4.1e-01	7.6e-01	II	...
				16 0.305	0.090	0.111	5.3e-01	4.5e-01		
74	SPICY 80873	274.7209	-16.6357	18 0.260	0.063	0.143	6.3e-01	1.9e-02	II	...
				18 0.303	0.085	0.119	3.2e-01	1.2e-02		
75	SPICY 80883	274.7232	-16.6883	18 0.286	0.071	0.138	9.2e-01	1.4e-01	II	...
				18 0.189	0.047	0.076	4.4e-01	2.0e-01		
76	SPICY 80894	274.7273	-16.7800	18 0.274	0.059	0.058	9.2e-01	4.1e-01	II	...
				18 0.133	0.033	0.048	8.0e-01	9.3e-01		
77	SPICY 80919	274.7329	-16.8060	13 0.690	0.196	0.246	5.9e-01	1.2e-01	II	...
				13 0.478	0.128	0.148	5.4e-01	4.8e-01		
78	SPICY 80923	274.7337	-16.6610	15 0.240	0.068	0.185	8.7e-01	1.7e-01	uncertain	...
				15 0.278	0.067	0.171	5.4e-01	8.1e-02		
79	SPICY 80927	274.7355	-16.7790	18 0.089	0.025	0.075	6.2e-02	1.3e-01	0/I	...
				18 0.102	0.026	0.080	2.4e-01	4.3e-01		
80	SPICY 80931	274.7377	-16.6334	18 0.227	0.062	0.134	7.4e-01	2.3e-01	0/I	...
				18 0.148	0.033	0.074	9.5e-01	9.4e-01		
81	SPICY 80934	274.7384	-16.6495	18 0.374	0.088	0.080	9.2e-01	3.6e-01	II	...
				18 0.309	0.075	0.038	8.4e-01	3.0e-01		
82	SPICY 80935	274.7392	-16.6255	18 0.338	0.087	0.073	9.3e-01	1.7e-01	III	...
				18 0.276	0.091	0.056	3.0e-01	2.7e-01		
83	SPICY 80961	274.7474	-16.6839	18 0.492	0.120	0.101	9.5e-01	1.3e-01	0/I	...
				18 0.540	0.129	0.075	9.9e-01	3.7e-01		
84	SPICY 80968	274.7493	-16.9031	18 0.246	0.065	0.068	1.6e-01	2.9e-02	0/I	...
				18 0.518	0.121	0.060	1.2e-01	2.6e-02		
85	SPICY 80969	274.7494	-16.6347	18 0.235	0.058	0.070	5.4e-02	2.1e-02	0/I	...
				18 0.266	0.067	0.052	6.9e-02	1.1e-02		
86	SPICY 80971	274.7495	-16.9592	17 0.382	0.098	0.101	5.1e-01	3.1e-01	II	Y
				17 0.301	0.081	0.053	4.3e-01	4.8e-01		
87	SPICY 80973	274.7499	-16.6802	18 0.474	0.119	0.152	1.5e-01	2.3e-01	II	...
				18 0.446	0.114	0.074	3.4e-02	4.4e-01		
88	SPICY 80976	274.7507	-16.8742	15 0.391	0.108	0.137	2.8e-01	4.2e-01	III	...
				15 0.502	0.124	0.123	4.8e-01	2.9e-01		
89	SPICY 80982	274.7528	-16.6857	15 0.294	0.082	0.159	9.1e-02	2.7e-01	0/I	...
				15 0.346	0.097	0.103	8.9e-01	1.8e-01		
90	SPICY 81006	274.7597	-16.6794	18 0.125	0.033	0.135	3.5e-01	1.1e-01	II	...
				18 0.144	0.039	0.124	8.4e-01	5.5e-01		
91	SPICY 81011	274.7612	-16.6829	18 0.390	0.114	0.120	1.0e+00	4.4e-01	II	...
				18 0.450	0.122	0.098	7.5e-01	4.6e-01		
92	SPICY 81025	274.7636	-16.6492	14 0.664	0.191	0.367	2.0e-02	1.5e-01	0/I	...
				14 0.349	0.104	0.167	7.1e-03	2.4e-03		
93	SPICY 81028	274.7655	-16.6879	15 0.254	0.070	0.106	5.8e-01	8.3e-02	II	...
				15 0.202	0.069	0.102	7.8e-01	4.7e-01		
94	SPICY 81061	274.7751	-16.6448	18 0.246	0.067	0.097	2.7e-01	6.7e-02	0/I	...
				18 0.246	0.061	0.083	1.0e+00	4.4e-01		
95	SPICY 81095	274.7811	-16.6741	18 0.350	0.087	0.109	1.8e-01	6.4e-01	II	...
				18 0.285	0.086	0.062	1.7e-01	1.2e-01		
96	SPICY 81130	274.7886	-16.6654	16 0.903	0.239	0.280	1.6e-01	2.4e-01	II	...
				16 0.567	0.143	0.168	9.4e-01	5.8e-02		
97	SPICY 81147	274.7946	-16.8397	18 0.329	0.097	0.138	5.7e-01	2.8e-02	II	...
				18 0.326	0.086	0.056	6.0e-01	1.3e-02		
98	SPICY 81151	274.7953	-16.6277	17 0.372	0.089	0.141	1.0e+00	9.7e-01	II	...
				17 0.220	0.061	0.151	8.8e-01	1.5e-01		
99	SPICY 81186	274.8040	-16.6750	16 0.199	0.056	0.165	6.5e-01	2.9e-02	II	...
				16 0.311	0.088	0.176	3.8e-01	2.1e-01		
100	SPICY 81191	274.8046	-16.8102	18 0.283	0.064	0.089	8.8e-01	1.0e+00	III	...
				18 0.287	0.080	0.095	6.3e-01	6.7e-02		
101	SPICY 81204	274.8077	-16.8198	18 0.295	0.080	0.150	9.3e-01	5.1e-01	II	...
				18 0.246	0.074	0.093	8.1e-01	8.8e-03		
102	SPICY 81224	274.8120	-16.5990	18 0.173	0.047	0.100	1.0e-01	8.7e-02	II	...
				18 0.201	0.057	0.102	1.5e-01	7.6e-02		
103	SPICY 81232	274.8131	-16.6000	13 0.363	0.106	0.148	1.0e+00	1.6e-01	II	...
				13 0.402	0.108	0.147	1.8e-01	9.8e-02		
104	SPICY 81242	274.8157	-16.8383	14 0.323	0.085	0.169	4.5e-01	4.8e-01	0/I	...
				14 0.333	0.106	0.099	6.0e-01	2.8e-01		
105	SPICY 81251	274.8184	-16.7325	18 0.257	0.065	0.079	9.9e-01	1.0e-01	uncertain	...
				18 0.462	0.118	0.116	5.6e-01	5.1e-01		

NOTE—Continued on next page

Table B3. Continued from previous page

#	ID ^a	R.A. (deg)	Dec. (deg)	N	$\Delta(W)$ (mag)	SD (mag)	σ (mag)	FAP _{Lin}	FAP _{LSP}	Class ^b	Outside ^c
106	SPICY 81254	274.8186	−16.7659	18	0.325	0.090	0.129	7.9e−01	7.5e−02	III	...
				18	0.389	0.091	0.086	5.8e−01	2.6e−01		
107	SPICY 81255	274.8191	−16.7443	18	0.257	0.065	0.070	7.5e−01	4.2e−02	II	...
				18	0.301	0.074	0.045	8.7e−01	1.6e−01		
108	SPICY 81261	274.8227	−16.6042	18	0.250	0.061	0.131	3.6e−01	7.5e−01	II	...
				18	0.226	0.059	0.112	6.4e−01	9.5e−02		
109	SPICY 81298	274.8349	−16.8103	18	0.371	0.111	0.148	7.9e−02	2.5e−01	II	...
				18	0.181	0.051	0.070	5.2e−02	7.4e−01		
110	SPICY 81306	274.8366	−16.7339	18	0.523	0.170	0.181	9.8e−01	2.4e−02	II	...
				18	0.641	0.191	0.135	9.1e−01	4.1e−01		
111	SPICY 81331	274.8429	−16.7194	16	0.418	0.116	0.177	6.1e−01	3.2e−03	II	...
				16	0.401	0.109	0.157	1.2e−01	1.2e−02		
112	SPICY 81332	274.8433	−16.7227	18	0.267	0.080	0.134	9.7e−01	8.4e−02	0/I	...
				18	0.202	0.068	0.106	2.0e−01	1.9e−02		
113	SPICY 81391	274.8644	−16.7846	18	0.214	0.060	0.091	9.8e−01	1.3e−01	II	...
				18	0.282	0.073	0.080	9.5e−01	2.5e−01		
114	SPICY 81412	274.8727	−16.7324	18	0.377	0.091	0.167	4.3e−01	6.2e−01	0/I	...
				18	0.434	0.097	0.079	8.5e−01	9.0e−01		
115	SPICY 81415	274.8736	−16.7331	18	0.370	0.090	0.166	4.0e−01	9.9e−01	II	...
				18	0.389	0.090	0.080	8.6e−01	8.8e−01		
116	SPICY 81477	274.8986	−16.7624	15	0.735	0.189	0.259	1.4e−01	4.8e−01	II	...
				15	0.346	0.090	0.148	8.3e−02	6.4e−02		
117	SPICY 81502	274.9056	−16.8041	18	0.395	0.097	0.089	6.1e−01	2.8e−02	II	...
				18	0.470	0.114	0.102	9.8e−01	6.7e−02		
118	SPICY 81516	274.9129	−16.7174	18	0.416	0.098	0.050	3.0e−01	9.5e−01	0/I	...
				18	0.482	0.114	0.055	4.3e−01	8.9e−02		
119	SPICY 81531	274.9197	−16.6897	14	0.865	0.225	0.402	4.4e−01	1.6e−01	II	...
				14	0.449	0.111	0.148	9.3e−01	5.8e−02		
120	SPICY 81537	274.9232	−16.7504	18	0.210	0.049	0.120	2.5e−01	1.1e−01	II	...
				18	0.170	0.044	0.062	5.2e−02	4.4e−01		
121	SPICY 81539	274.9238	−16.7473	14	0.633	0.155	0.145	1.7e−01	2.3e−01	II	...
				14	0.790	0.191	0.124	2.6e−01	3.6e−01		
122	SPICY 81542	274.9252	−16.6950	18	0.737	0.173	0.118	7.3e−01	4.8e−01	II	...
				18	0.617	0.146	0.089	9.1e−01	3.4e−02		
123	SPICY 81600	274.9501	−16.7376	18	0.521	0.134	0.043	8.0e−03	1.1e−01	0/I	...
				18	0.364	0.097	0.050	2.4e−01	1.0e−01		
124	GLMA G014.0330-00.5157	274.4610	−16.9993	18	0.164	0.044	0.052	3.1e−01	2.6e−02	0/I	...
				18	0.274	0.074	0.140	2.3e−01	2.6e−01		
125	GLMA G014.1667-00.4990	274.5119	−16.8736	18	0.147	0.042	0.061	7.9e−01	2.7e−01	II	...
				18	0.265	0.072	0.057	8.4e−01	3.0e−01		
126	GLMA G014.2167-00.6341	274.6610	−16.8936	18	0.162	0.042	0.092	6.0e−01	7.5e−02	II	...
				18	0.234	0.068	0.176	2.2e−01	4.0e−02		
127	GLMA G014.2459-00.5815	274.6270	−16.8429	15	0.500	0.123	0.171	8.7e−01	4.7e−01	II	...
				15	0.410	0.109	0.165	7.3e−01	3.5e−01		
128	GLMA G014.3109-00.5928	274.6695	−16.7910	18	0.258	0.064	0.065	4.5e−03	4.8e−01	0/I	...
				18	0.269	0.077	0.061	6.5e−03	3.9e−02		
129	GLMA G014.3411-00.6392	274.7271	−16.7863	18	0.445	0.101	0.128	4.5e−01	1.4e−01	II	...
				18	0.311	0.084	0.143	9.6e−01	9.2e−03		
130	GLMA G014.4335-00.6970	274.8259	−16.7323	16	0.941	0.292	0.299	3.8e−02	3.5e−02	0/I	...
				16	0.512	0.154	0.298	8.4e−03	2.1e−02		
131	GLMA G014.4810-00.6167	274.7755	−16.6525	18	0.274	0.070	0.105	2.3e−01	5.9e−01	II	...
				18	0.374	0.108	0.096	9.6e−01	1.0e−01		
132	GLMA G014.4911-00.7629	274.9150	−16.7126	18	0.345	0.086	0.163	1.6e−01	1.1e−01	II	...
				18	0.358	0.091	0.062	8.7e−02	9.0e−01		

NOTE—In the table, where two values are stacked vertically, the top value corresponds to W1 while the bottom value denotes W2.

^aAll source identifiers (IDs) are based on designations from two key references: Kuhn et al. (2021) and Povich & Whitney (2010). Kuhn et al. (2021) utilizes the SPICY (Spitzer/IRAC Candidate YSO) numbering system, while Povich & Whitney (2010) refer to sources by their GLIMPSE Archive (GLMA) coordinates. SPICY IDs are numerical, whereas GLMA IDs are presented in a Galactic coordinate format.

^b YSO classification.

^cAll sources are presumed to be associated with M17 SWEx, unless marked as 'outside' (Y) in accordance with the determinations by Kuhn et al. (2021).

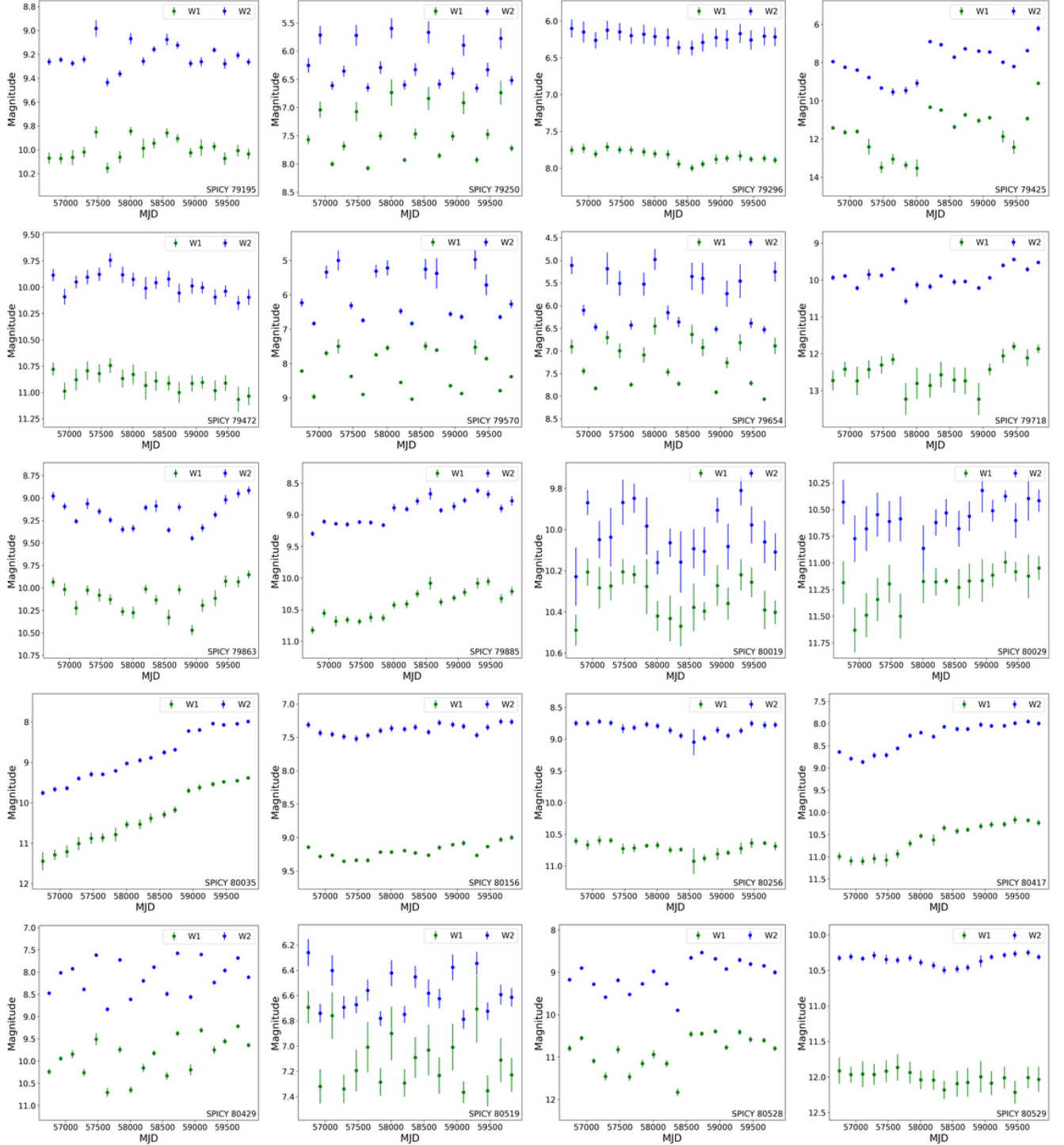


Figure B1. Mid-IR light curves for sources in the final WISE sample, included in either the W1 or W2 analysis, are presented. The total number of sources is 179. Sources shown in Figure 9 are not included here. The first 40 sources exhibit flux variability in either the W1 or W2 band. The subsequent panels display sources that were not observed to vary in this study. The source identifier is provided in the bottom right corner of each panel.

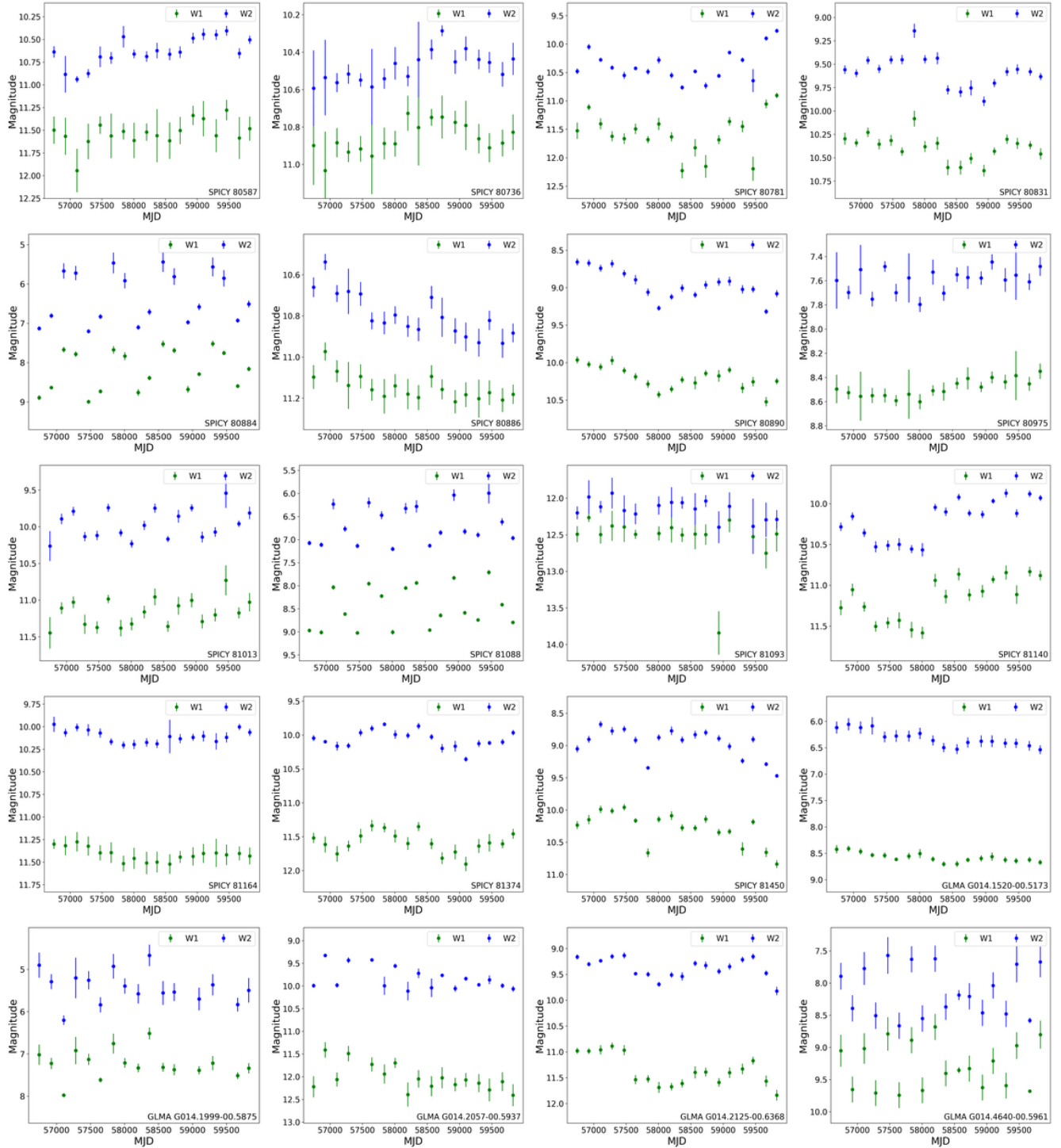


Figure B1. Continued from the previous page.

- Fischer, W. J., Hillenbrand, L. A., Herczeg, G. J., et al. 2023, in Astronomical Society of the Pacific Conference Series, Vol. 534, Protostars and Planets VII, ed. S. Inutsuka, Y. Aikawa, T. Muto, K. Tomida, & M. Tamura, 355, doi: [10.48550/arXiv.2203.11257](https://doi.org/10.48550/arXiv.2203.11257)
- Fischer, W. J., Safron, E., & Megeath, S. T. 2019, ApJ, 872, 183, doi: [10.3847/1538-4357/ab01dc](https://doi.org/10.3847/1538-4357/ab01dc)
- Fischer, W. J., Battersby, C., Johnstone, D., et al. 2024, AJ, 167, 82, doi: [10.3847/1538-3881/ad188b](https://doi.org/10.3847/1538-3881/ad188b)
- Francis, L., Johnstone, D., Lee, J.-E., et al. 2022, ApJ, 937, 29, doi: [10.3847/1538-4357/ac8a9e](https://doi.org/10.3847/1538-4357/ac8a9e)
- Grankin, K. N., Bouvier, J., Herbst, W., & Melnikov, S. Y. 2008, A&A, 479, 827, doi: [10.1051/0004-6361:20078476](https://doi.org/10.1051/0004-6361:20078476)
- Groenewegen, M. A. T. 2022, A&A, 659, A145, doi: [10.1051/0004-6361/202142648](https://doi.org/10.1051/0004-6361/202142648)
- Guarcello, M. G., Flaccomio, E., Micela, G., et al. 2017, A&A, 602, A10, doi: [10.1051/0004-6361/201629983](https://doi.org/10.1051/0004-6361/201629983)
- Herbst, W., LeDuc, K., Hamilton, C. M., et al. 2010, AJ, 140, 2025, doi: [10.1088/0004-6256/140/6/2025](https://doi.org/10.1088/0004-6256/140/6/2025)
- Herczeg, G. J., Johnstone, D., Mairs, S., et al. 2017, ApJ, 849, 43, doi: [10.3847/1538-4357/aa8b62](https://doi.org/10.3847/1538-4357/aa8b62)
- Hodapp, K. W., Chini, R., Watermann, R., & Lemke, R. 2012, ApJ, 744, 56, doi: [10.1088/0004-637X/744/1/56](https://doi.org/10.1088/0004-637X/744/1/56)
- Holland, W. S., Bintley, D., Chapin, E. L., et al. 2013, MNRAS, 430, 2513, doi: [10.1093/mnras/sts612](https://doi.org/10.1093/mnras/sts612)
- Hosokawa, T., Offner, S. S. R., & Krumholz, M. R. 2011, ApJ, 738, 140, doi: [10.1088/0004-637X/738/2/140](https://doi.org/10.1088/0004-637X/738/2/140)
- Hsieh, T.-H., Murillo, N. M., Belloche, A., et al. 2019, ApJ, 884, 149, doi: [10.3847/1538-4357/ab425a](https://doi.org/10.3847/1538-4357/ab425a)
- Johnstone, D., Hendricks, B., Herczeg, G. J., & Bruderer, S. 2013, ApJ, 765, 133, doi: [10.1088/0004-637X/765/2/133](https://doi.org/10.1088/0004-637X/765/2/133)
- Johnstone, D., Herczeg, G. J., Mairs, S., et al. 2018, ApJ, 854, 31, doi: [10.3847/1538-4357/aaa764](https://doi.org/10.3847/1538-4357/aaa764)
- Johnstone, D., Lalchand, B., Mairs, S., et al. 2022, ApJ, 937, 6, doi: [10.3847/1538-4357/ac8a48](https://doi.org/10.3847/1538-4357/ac8a48)
- Jørgensen, J. K., Visser, R., Williams, J. P., & Bergin, E. A. 2015, A&A, 579, A23, doi: [10.1051/0004-6361/201425317](https://doi.org/10.1051/0004-6361/201425317)
- Kackley, R., Scott, D., Chapin, E., & Friberg, P. 2010, in Society of Photo-Optical Instrumentation Engineers (SPIE) Conference Series, Vol. 7740, Software and Cyberinfrastructure for Astronomy, ed. N. M. Radziwill & A. Bridger, 77401Z, doi: [10.1117/12.857397](https://doi.org/10.1117/12.857397)
- Kuhn, M. A., de Souza, R. S., Krone-Martins, A., et al. 2021, ApJS, 254, 33, doi: [10.3847/1538-4365/abe465](https://doi.org/10.3847/1538-4365/abe465)
- Kunitomo, M., Guillot, T., Takeuchi, T., & Ida, S. 2017, A&A, 599, A49, doi: [10.1051/0004-6361/201628260](https://doi.org/10.1051/0004-6361/201628260)
- Lee, J.-E. 2007, Journal of Korean Astronomical Society, 40, 83, doi: [10.5303/JKAS.2007.40.4.083](https://doi.org/10.5303/JKAS.2007.40.4.083)
- Lee, J.-E., Lee, S., Lee, S., et al. 2021a, ApJL, 916, L20, doi: [10.3847/2041-8213/ac0d59](https://doi.org/10.3847/2041-8213/ac0d59)
- Lee, J.-E., Baek, G., Lee, S., et al. 2023, ApJ, 956, 43, doi: [10.3847/1538-4357/ace34b](https://doi.org/10.3847/1538-4357/ace34b)
- Lee, S., Lee, J.-E., Johnstone, D., Herczeg, G. J., & Aikawa, Y. 2024, ApJ, 964, 34, doi: [10.3847/1538-4357/ad21e3](https://doi.org/10.3847/1538-4357/ad21e3)
- Lee, Y.-H., Johnstone, D., Lee, J.-E., et al. 2020, ApJ, 903, 5, doi: [10.3847/1538-4357/abb6fe](https://doi.org/10.3847/1538-4357/abb6fe)
- . 2021b, ApJ, 920, 119, doi: [10.3847/1538-4357/ac1679](https://doi.org/10.3847/1538-4357/ac1679)
- Lomb, N. R. 1976, Ap&SS, 39, 447, doi: [10.1007/BF00648343](https://doi.org/10.1007/BF00648343)
- Lucas, P. W., Hoare, M. G., Longmore, A., et al. 2008, MNRAS, 391, 136, doi: [10.1111/j.1365-2966.2008.13924.x](https://doi.org/10.1111/j.1365-2966.2008.13924.x)
- MacFarlane, B., Stamatellos, D., Johnstone, D., et al. 2019a, MNRAS, 487, 5106, doi: [10.1093/mnras/stz1512](https://doi.org/10.1093/mnras/stz1512)
- . 2019b, MNRAS, 487, 4465, doi: [10.1093/mnras/stz1570](https://doi.org/10.1093/mnras/stz1570)
- Mainzer, A., Bauer, J., Grav, T., et al. 2011, ApJ, 731, 53, doi: [10.1088/0004-637X/731/1/53](https://doi.org/10.1088/0004-637X/731/1/53)
- Mainzer, A., Bauer, J., Cutri, R. M., et al. 2014, ApJ, 792, 30, doi: [10.1088/0004-637X/792/1/30](https://doi.org/10.1088/0004-637X/792/1/30)
- Mairs, S., Lane, J., Johnstone, D., et al. 2017, ApJ, 843, 55, doi: [10.3847/1538-4357/aa7844](https://doi.org/10.3847/1538-4357/aa7844)
- Mairs, S., Lee, S., Johnstone, D., et al. 2024, arXiv e-prints, arXiv:2401.03549, doi: [10.48550/arXiv.2401.03549](https://doi.org/10.48550/arXiv.2401.03549)
- Molyarova, T., Akimkin, V., Semenov, D., et al. 2018, ApJ, 866, 46, doi: [10.3847/1538-4357/aadfd9](https://doi.org/10.3847/1538-4357/aadfd9)
- Nguyen-Luong, Q., Nakamura, F., Sugitani, K., et al. 2020, ApJ, 891, 66, doi: [10.3847/1538-4357/ab700a](https://doi.org/10.3847/1538-4357/ab700a)
- Park, W., Lee, J.-E., Contreras Peña, C., et al. 2021, ApJ, 920, 132, doi: [10.3847/1538-4357/ac1745](https://doi.org/10.3847/1538-4357/ac1745)
- Petrov, L., Kovalev, Y. Y., Fomalont, E. B., & Gordon, D. 2011, AJ, 142, 35, doi: [10.1088/0004-6256/142/2/35](https://doi.org/10.1088/0004-6256/142/2/35)
- Povich, M. S., Townsley, L. K., Robitaille, T. P., et al. 2016, ApJ, 825, 125, doi: [10.3847/0004-637X/825/2/125](https://doi.org/10.3847/0004-637X/825/2/125)
- Povich, M. S., & Whitney, B. A. 2010, ApJL, 714, L285, doi: [10.1088/2041-8205/714/2/L285](https://doi.org/10.1088/2041-8205/714/2/L285)
- Rathborne, J. M., Whitaker, J. S., Jackson, J. M., et al. 2016, PASA, 33, e030, doi: [10.1017/pasa.2016.23](https://doi.org/10.1017/pasa.2016.23)
- Scargle, J. D. 1989, ApJ, 343, 874, doi: [10.1086/167757](https://doi.org/10.1086/167757)
- Scholz, A., Froebrich, D., & Wood, K. 2013, MNRAS, 430, 2910, doi: [10.1093/mnras/stt091](https://doi.org/10.1093/mnras/stt091)
- Schuller, F., Menten, K. M., Contreras, Y., et al. 2009, A&A, 504, 415, doi: [10.1051/0004-6361/200811568](https://doi.org/10.1051/0004-6361/200811568)
- Shimoikura, T., Dobashi, K., Hirose, A., et al. 2019, PASJ, 71, S6, doi: [10.1093/pasj/psz061](https://doi.org/10.1093/pasj/psz061)
- Sugitani, K., Nakamura, F., Shimoikura, T., et al. 2019, PASJ, 71, S7, doi: [10.1093/pasj/psz072](https://doi.org/10.1093/pasj/psz072)
- Taylor, M. B. 2005, in Astronomical Society of the Pacific Conference Series, Vol. 347, Astronomical Data Analysis Software and Systems XIV, ed. P. Shopbell, M. Britton, & R. Ebert, 29

- Urquhart, J. S., Moore, T. J. T., Csengeri, T., et al. 2014, MNRAS, 443, 1555, doi: [10.1093/mnras/stu1207](https://doi.org/10.1093/mnras/stu1207)
- Whitney, B. A., Wood, K., Bjorkman, J. E., & Cohen, M. 2003, ApJ, 598, 1079, doi: [10.1086/379068](https://doi.org/10.1086/379068)
- Wright, E. L., Eisenhardt, P. R. M., Mainzer, A. K., et al. 2010, AJ, 140, 1868, doi: [10.1088/0004-6256/140/6/1868](https://doi.org/10.1088/0004-6256/140/6/1868)
- Wu, Y. W., Sato, M., Reid, M. J., et al. 2014, A&A, 566, A17, doi: [10.1051/0004-6361/201322765](https://doi.org/10.1051/0004-6361/201322765)
- Yoo, H., Lee, J.-E., Mairs, S., et al. 2017, ApJ, 849, 69, doi: [10.3847/1538-4357/aa8c0a](https://doi.org/10.3847/1538-4357/aa8c0a)
- Yoon, S.-Y., Herczeg, G. J., Lee, J.-E., et al. 2022, ApJ, 929, 60, doi: [10.3847/1538-4357/ac5632](https://doi.org/10.3847/1538-4357/ac5632)
- Zakri, W., Megeath, S. T., Fischer, W. J., et al. 2022, ApJL, 924, L23, doi: [10.3847/2041-8213/ac46ae](https://doi.org/10.3847/2041-8213/ac46ae)